DOCTOR OF PHILOSOPHY

Conical Diffraction Photonics

Grant, Stephen D.

Award date:
2016

Conical Diffraction Photonics

Mr Stephen D. Grant, BSc (Hons)

Supervisor: Prof. Amin Abdolvand

A thesis submitted to the School of Science and Engineering, University of Dundee for the degree of Doctor of Philosophy (PhD)

April 2016

Table of Contents

List of Figures

List of Tables

List of Acronyms

APL – Azimuthally Polarised Light

CD – Conical Diffraction

CPL – Circularly Polarised Light

CR – Conical Refraction

KGW – Potassium Gadolinium Tungstate ($KGd(WO_4)_2$)

KTP – Potassium Titanyl Phospahate ($KTiOPO_4$)

LCPL – Left Circularly Polarised Light

LPL – Linearly Polarised Light

RCPL – Right Circularly Polarised Light

RPL – Radially Polarised Light

SH – Second Harmonic

SHG – Second Harmonic Generation

UPL – Unpolarised Light

Declaration

I, the undersigned, declare that I am the author of this thesis; that all references cited have been consulted by me; that the work of which the thesis is a record has been done by myself, and it has not been previously accepted for a higher degree.

Stephen Grant

Certification

I, Professor A. Abdolvand of the School of Science and Engineering, hereby certify that Stephen Grant has spent the required number of terms at research under my supervision and that he has fulfilled the conditions of the Ordinance of the University of Dundee so that he is qualified to submit the following thesis for the degree of Doctor of Philosophy.

Amin Abdolvand

List of Publications

1. Stephen D. Grant, Amin Abdolvand: *Left- and right-circularly polarized light in cascade conical diffraction*. **Optics Letters** 12/2012; 37(24):5226-8. DOI:10.1364/OL.37.005226
2. Stephen D. Grant, Svetlana A. Zolotovskaya, Todor K. Kalkandjiev, W. Allan Gillespie, Amin Abdolvand: *On the frequency-doubled conically-refracted Gaussian beam*. **Optics Express** 09/2014; 22(18-18):21347-21353. DOI:10.1364/OE.22.021347
3. Stephen D. Grant, Svetlana A. Zolotovskaya, W. Allan Gillespie, Todor K Kalkandjiev, Amin Abdolvand: *Azimuthally and radially polarized light in conical diffraction*. **Optics Letters** 04/2014; 39(7):1988-91. DOI:10.1364/OL.39.001988
4. Stephen D. Grant, Amin Abdolvand: *Evolution of conically diffracted Gaussian beams in free space*. **Optics Express** 02/2014; 22(4):3880-6. DOI:10.1364/OE.22.003880
5. Stephen D. Grant, Steve Reynolds, Amin Abdolvand: *Optical sensing of chirality using conical diffraction phenomenon.* **Journal of Optics.** 01/2016; 18(2):025609. DOI:10.1088/2040-8978/18/2/025609

Publication not related to this work:

S. Anand, J. Nylk, S. L. Neale, C. Dodds, S. D. Grant, M. H. Ismail, J. Reboud, J. M. Cooper, D. McGloin: *Aerosol droplet optical trap loading using surface acoustic wave nebulization*. **Optics Express** 12/2013; 21(25):30148-55. DOI:10.1364/OE.21.030148

Acknowledgements

I would like to thank my supervisors Professor Amin Abdolvand and Dr. Steve Reynolds for the opportunity, guidance, advice and support throughout these last three years, and the Engineering and Physical Sciences Research Council (EPSRC) for funding this work.

I would also like to thank all the members of the MAPS research group for assistance, collaboration, and many fruitful conversations, in particular Dr. Svetlana Zolotovskaya, Dr Andrew Hourd, Lauren Fleming, and Mateusz Tyrk.

Finally I'd like to thank my friends and all of my family for their continued support.

Abstract

Recent interest in conical diffraction (CD) has led to a large increase in experimental and theoretical investigations over the last two decades, a marked change from the previous 160 quiet years in the field. Once dismissed as an optical curiosity, the phenomenon has emerged as a fascinating area with potential for a large number of practical applications many of which have been realised while others are still being discovered.

In this thesis a number of aspects of the theory as recently described are experimentally investigated with a view to strengthening the current theoretical understanding of the phenomenon.

Developing from single crystal CD (the simplest case), through cascade CD, non-linear CD, and with a particular emphasis on the polarisation effects of the phenomenon, a number of areas are investigated.

Single crystal CD with circularly (CPL), linearly (LPL), azimuthally and radially polarised light (APL and RPL) is examined. The effect of LPL in removing a section of the ring orthogonally polarised to the incident beam is shown, along with the first investigation into the effects of RPL and APL polarisation effects in CD. The effect of the incident beam spot size on the pattern developed is also investigated and shown to conform to the theory. All findings show good agreement with the current theory.

Cascade CD with various numbers of crystals and incident beam polarisations is investigated. Included in these experiments are a variable two crystal cascade and

the first demonstration of the different patterns produced for a three crystal cascade when left and right circularly polarised light (LCPL and RCPL, respectively) are used, as recently predicted. As with the single crystal case, results are in agreement with theory. In both the single and cascade cases a cross section of the beam is captured to demonstrated the free space evolution of a CD beam.

Simultaneous second harmonic generation (SHG) and CD from a single crystal is described in an update of Bloembergen et al.'s pioneering 1970's investigations with added emphasis on polarisation. SHG in non-phase matched conditions, as well as the influence of incident polarisation on the pattern and type of SHG, are observed.

And finally a sensor based on CD demonstrating a simple, practical application of the phenomenon is outlined and a prototype device made and trialled. Using the effect of LPL described earlier to determine the polarisation angle of an incident beam, the device's use as a polarimeter is also tested to determine the specific rotation introduced by optically active liquids with the initial prototype showing results comparable to current methods.

This work contains 7 chapters. The first is an introduction to the history of the phenomenon along with a thesis statement. Chapter 2 deals with single crystal CD, chapter 3 contains the expansion from single to cascade CD. The complexities introduced by various types of polarisation are described in chapter 4 for both single and cascade setups. Chapter 5 deals with SHG using a CD crystal and chapter 6 outlines the design and operation of the novel sensor based on the phenomenon. The final chapter is a summary of the work and outlook on the future of the field.

1 Introduction

Conical diffraction (CD) was first predicted in 1832 by William Rowan Hamilton and observed shortly thereafter by Humphrey Lloyd. The results of both of these events were published in 1837 and have slowly over the past 180 years led to the emergence of a fascinating and rapidly developing new area of research and development. Renewed interest in the last two decades has led to a rapid increase in the theoretical and experimental understanding of the phenomenon and a search for new and innovative applications for its unique properties.

This chapter contains an overview of the topic from its inception up to the time this work was undertaken, 2012-2015. Placing each major milestone in a historical context, the foundation on which the current field is established is revealed and this work is given a modest place in a larger, richer tapestry.

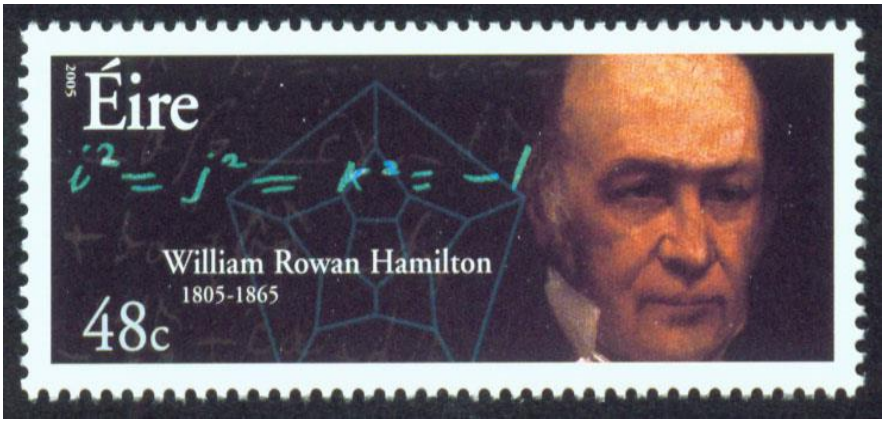

Figure 1.1 Irish stamp commemorating the bicentenary of Hamilton's birth in 2005 – a year designated the Year of Hamilton in the state.

1.1 Historical Background

1.1.1 William Rowan Hamilton

William Rowan Hamilton was born at the stroke of midnight on the 3rd/4th of August 1805 [1]. A linguistic and mathematical prodigy, Hamilton was fluent in many languages as a child and developed an interest in mathematics by early adolescence. Sparked by his discovery of an error in Laplace's *Mécanique céleste* before his 18th birthday, the Royal Astronomer of Ireland, John Brinkley, declared of him

> *'This young man, I do not say will be, but is, the first mathematician of his age.'* [1]

Hamilton entered Trinity College at the University of Dublin shortly thereafter and while still an undergraduate presented the memoir *Theory of Systems of Rays* [2] to the Royal Irish Academy. This memoir contained the introduction of a unified approach for optics, dynamics and mechanics.

In Hamilton's first supplement to the theory [3] he describes what he calls the Characteristic function, '*variation of the action, or the time, expended by light of any one colour, in going from one variable point to another.'*
The equation that accompanies this statement is the Equation of the Characteristic Function and, to Hamilton, this described 'the whole of mathematical optics'.

The *Equation of the Characteristic Function* is given by equation (1.1):

$$\delta V = \left(\delta \int v\, ds = \right) \frac{\delta v}{\delta \alpha} \delta x - \frac{\delta v'}{\delta \alpha'} \delta x' + \frac{\delta v}{\delta \beta} \delta y - \frac{\delta v'}{\delta \beta'} \delta y' + \frac{\delta v}{\delta \gamma} \delta z - \frac{\delta v'}{\delta \gamma'} \delta z' \qquad (1.1)$$

where x, y, and z are coordinates; α, β, and γ are cosines of direction of the ray ds, and v is the refractive index of the medium. Hamilton demonstrates how this equation can be reduced, by deduction of all other parameters, to depend on only V as an unknown and thus be solved offering a single method for any proposed problems in mathematical optics. Over the course of the supplement various circumstances are examined and the methods of using the characteristic function to investigate them are laid out.

The application of this function to various fields produced most interesting results, of particular importance here is the third supplement to the memoir, published in 1832 [4], wherein Hamilton's function was applied to optics and Hamilton's prediction of CD was set out.

It is when attention turns to Fresnel's wave (contained in numbers 28 & 29 of the supplement for the curious reader) that Hamilton begins to describe a general reformulation of reflection and refraction that leads to some 'remarkable theoretical conclusions.'

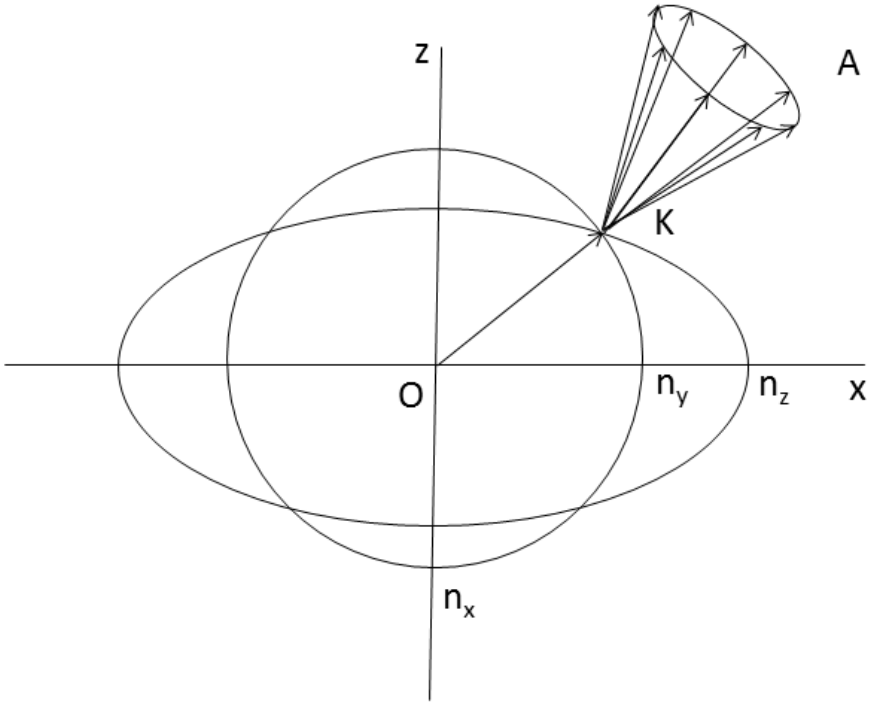

*Figure 1.2 Two dimension (xz plane) wave surface diagram showing the optic axis (line OA) passing through the wave surface intersection at K. The cone of rays between points K and A shows the surface created by the rotation of **S**.*

When considering the shape of the wave front Hamilton notes that the wave has a conoidal cusp and that no single tangent plane exists, instead a tangent cone touches the conoidal cusp. Four such conoidal cusps exist with two pairs each defining an optic axis as shown in figure 1.2. It also becomes apparent that the plane in contact with the end of an optic axis is a circle and that four such circles exist.

As the intersections take the form of a double cone (diabolo) they have come to be known as diabolical points.

Outlining a form of the laws of reflection and refraction in keeping with the characteristic function, Hamilton shows that the tangent plane to a reflecting

surface will determine the number of rays involved to satisfy the connection between the initial and final parameters. In a biaxial crystal it is seen that, generally, for every two incident rays a single refracted ray will be found and for every two refracted rays one incident ray exists. It is the exceptions to this general case that proved most interesting in Hamilton's work.

As no single tangent plane exists at a conoidal cusp there is no longer a pair of refracted rays for a single incident or vice versa, instead the so-called "cusp ray" has an infinite number of possible corresponding rays giving rise not to normal refraction, but a refracted cone of light. As described by Hamilton:

> '*this one internal cusp-ray must correspond to an external cone of rays, according to a new theoretical law of light which may be called External Conical Refraction.'* [4]

He also outlines the reciprocal relationship of 'internal conical refraction (CR)', wherein one external ray corresponds to an internal cone of rays.

It is from this prediction, based on the work of Fresnel and Hamilton's own insight and mathematical prowess, that Humphrey Lloyd, at Hamilton's request, carried out the first experiments in CD in 1833.

1.1.2 Reverend Humphrey Lloyd

Reverend Humphrey Lloyd (1800 - 1881) was a Fellow of Trinity College and Professor of Natural and Experimental Philosophy in the University of Dublin. He began studying at Trinity in 1815 at just 15 years old and quickly established himself as one of the leading experimentalists working there, becoming a junior fellow in

1824 and eventually becoming President of both the British Association and the Royal Irish Academy [5].

As noted in his 1833 paper, *On the Phænomena presented by Light in its Passage along the Axes of Bi-axal Crystals* [6], Lloyd was asked by Hamilton to carry out the experiments as Hamilton himself was *'naturally anxious',* due to the stakes of the results. The prediction could have potentially led to a sea-change in the contemporary understanding of light:

> '*If confirmed by experiment, they would furnish a new and almost convincing proof of the truth of that theory; and if disproved, on the other hand, it is evident that the theory must be abandoned or modified.'* [6]

Lloyd's experiment involved the use of an aragonite crystal, cut with its end faces perpendicular to the optic axis. A lens was used to focus the light from a lamp a *'considerable distance away'*, and the effect observed by looking through the crystal at the lamp. Having realised that light traveling from other directions would affect the results, a thin metal plate with an aperture on it was employed to ensure only light travelling along the optic axis would be seen. The phenomena then observed *'was in the highest degree curious.'*

> *'There appeared a luminous circle with a small dark space round the center and in this dark space (which was also nearly circular) were two bright points divided by a narrow and well defined dark line.'* [6]

Having observed the striking phenomenon, Lloyd began noting the features of it, in particular the unusual polarisation properties. He noted as the incident beam of light was polarised a small section of the ring disappeared and a half rotation of the plane of polarisation led to a full rotation of the missing section of the ring, a feature predicted by Hamilton previously.

In an additional short paper in 1833, *Further Experiments on the Phænomena presented by Light in its Passage along the Axes of Biaxal Crystals* [7], Lloyd presents further experiments which have better agreement with the theory.

This experimental confirmation of Hamilton's predictions marked a quiet revelation at the time. It was a rare, perhaps unheard of, example of a phenomenon predicted purely from mathematics, an application of phase space and dynamics with observable, real world effects and was a significant boon to the theory of light as a transverse wave.

Despite the challenging nature of the experiments at the time, what had been observed to this point was still the simplest case of CR and was lacking the fine detail of the internal structure of the ring. These details would emerge over the next 100 years due to the work of many scientists, most notably in the work of Poggendorff and Raman.

1.1.3 J.C. Poggendorff & C.V. Raman

Johann Christian Poggendorff was a German physicist known for his contributions to electricity and magnetism, as well as the optical illusion which bears his name. In terms of CD he is known for his 1839 [8] paper, wherein he describes the internal structure of the ring, namely that the ring consists of a:

'bright ring that encompasses a coal black sliver.'

It wasn't until the early 1900s when Voigt [9], explained the origin of the dark area bisecting the bright ring, he noted that the initial prediction was based on a perfectly collimated, infinitely narrow beam.

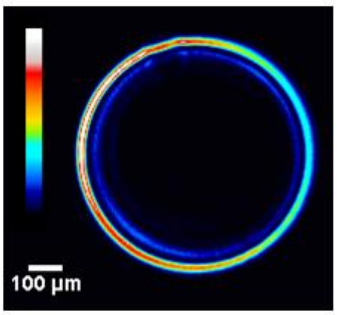

Figure 1.3 Typical CD ring pattern illustrating the pair of bright rings separated by a dark ring..

Obviously this is not the case in reality and so rays from the area around the diabolical point also influence the pattern. The intensity of the light is proportional to the radius of the rings which make up the so called wave cone. At the diabolical point this disappears giving zero intensity along the cylinder causing the dark area between the two bright rings.

Further observation on the evolution of a CD beam beyond the crystal was made by Raman, Rajagopalan and Nedungadi [10].

Chandrasekhara Venkata Raman was an Indian physicist known for his work in light scattering leading to a number of eponymous effects and methods including Raman Scattering, the Raman Effect and Raman spectroscopy.

In relation to CD, Raman noted that the ring turns into a bright central spot as the distance from the crystal face increases. As this effect is related to the circle of contact in external CD, the two effects, internal and external, cannot be treated as completely distinct.

1.1.4 Nicolaas Bloembergen

Nicolaas Bloembergen is a Dutch American physicist. He is known for his work in laser spectroscopy for which he, along with Arthur Schawlow and Kai Siegbahn, was awarded the Nobel Prize in physics [11]. In the 1970's he carried out a number of investigations into second harmonic generation (SHG) in CD with H. Shih [12] and A.J. Schell [13-14]. This work extended CD into the nonlinear regime and outlined a scheme for characterising the observed effects on the produced patterns in the case of nonlinear CD. This work will be examined in more detail in a later chapter.

This was a notable expansion of the field in a new direction and marked the first version of a full wave theory for the phenomenon. However this treatment was in some ways limited and a further, more complete, expansion of the theory was carried out by Belsky and Khapalyuk. [15]

1.1.5 Belsky & Khapalyuk

A.M. Belsky and A.P. Khapalyuk gave, in 1978 [15], a definitive formulation of the theory governing CD by including the previously omitted paraxial nature of the phenomenon. This moved from a geometrical optics based theory to a wave based one which was required to describe a number of aspects of the theory such as Poggendorff's dark ring and the Raman bright spot. This shift to a wave based understanding has led to the phenomenon being referred to increasingly as *conical*

diffraction (as it is in this work) as opposed to *conical refraction* to reflect the necessity of using the wave theory of light to obtain a more thorough understanding of the field.

1.1.6 Modern Day – Michael Berry

Renewed interest in the field in the past two decades has led to a surge in publications relating to both theoretical aspects of CD and increasingly, experimental observations and applications. Chief among these is the work of Michael Berry at Bristol University whose reformulation of the Belsky-Khapulyuk theory [16], by analytically solving the Belsky-Khapulyuk integrals has taken over as the defacto standard theory for the phenomenon.

The increase in interest has led to a better theoretical understanding in recent years with the aforementioned recapitulation of the theory as well as expanding the theory to include cascade CD [17], dichroism [18], optical activity [19] and nonlinearity [20]. The nature of the beam in free space has also been investigated [21], [22] and resulted in the current description of a '*bottle-beam*' due to the beam consisting of two intersecting oppositely propagating cones.

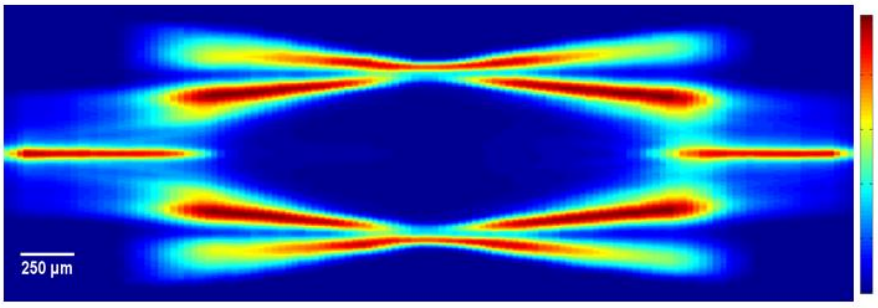

Figure 1.4 Cross section of the evolution of a CD beam in free space showing the 'bottle-beam' structure.

As well as these theoretical advances, the practical space has also expanded to include more practical experimental methodology and numerous applications have been found. Some examples include Bessel beam formation [23], free space multiplexing [24], which has applications in communications, optical trapping [25] [26], and lasers based on CD [27]–[29].

It is in this environment of advancement that this work was undertaken with a view to experimentally examine some of the fundamental properties of the phenomenon. It is hoped that by adding to the practical usage and understanding of the phenomenon, that doorways to applications of CD will be found.

1.2 Thesis Statement

The work contained in this thesis concerns investigations relating to various aspects of the predictions made in the aforementioned theoretical works, and investigating possible applications of CD.

Starting with the most fundamental work, chapter 2 will look into the basic evolution of a CD beam in free space, various parameters and the dependence of the CD beam on the crystals used to produce it. The experimental work is based on the theory as laid out by Berry in [30], and this work has been published in [31].

Chapter 3 expands this to look into the same parameters and evolution of a beam diffracted not by one but a cascade of CD crystals. This includes the effects of the orientations of the crystals in the cascade. This work is also contained in [31]

Chapter 4 investigates the effects of polarisation on the produced beams for both single crystal and cascade configurations. Polarisation is one of the most interesting

aspects of a CD beam. Here we investigate unpolarised (UPL); linearly polarised (LPL) [31], circularly-polarised (CPL) [32], radially- and azimuthally-polarised beams (RPL and APL respectively) [33], and the effects of each type on the pattern so produced in the ring plane and, in the case of LCPL and RCPL, away from the ring plane.

Moving into the nonlinear realm, chapter 5 involves using a potassium titanyl phosphate (KTP) crystal to produce nonlinear effects in the generation of a simultaneous CD and frequency-doubled beam adhering to the experimental work of Schell and Bloembergen in the 1970s. This work is from [34]

Chapter 6 regards the design and production of a polarisation sensor using a simple Logitech webcam, taking advantage of the polarisation properties of CD to determine the polarisation angle of an incident Gaussian beam [35].

Finally Chapter 7 is used to summarize the preceding work, report briefly on the advances made in the field to the current time and provide an outlook to possible future work.

2 Single Crystal Conical Diffraction

Initial experiments were limited to the case of single crystal conical diffraction (CD) not dissimilar to the experiments carried out by Humphrey Lloyd 180 years ago [6-7]. This was both to investigate some of the predicted, but not yet experimentally verified aspects of CD, and also to become familiar with the practical use of CD crystals and the nuances involved in viewing the phenomenon before moving onto more complex experiments. Four main parameters pertaining to the evolution and shape of a CD beam are investigated along with obtaining a cross section of the beam in free space and assessing the impact of incident beam size on the produced ring pattern.

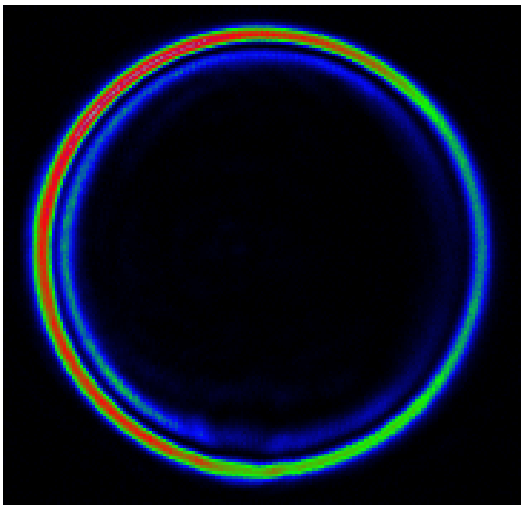

Figure 2.1 Typical CD ring pattern

2.1 Introduction

The goals for this chapter were to (1) investigate a number of parameters as derived from the work of Michael Berry in [30], and (2) to investigate the dependence of the pattern in the ring plane on the ratio of ring radius to incident beam radius, the so called *beam strength,* ρ_0, as predicted by Belsky and Stepanov in [36].

A brief overview of the theoretical understanding of CD as it stands today, based on the work of Michael Berry, and building upon the work of not only Belsky and Khapalyuk, but all of the aforementioned scientists back through 180 years to William Hamilton himself, is contained in appendix 1. Only a physical description of the phenomenon and the aspects of the theory relevant to this work are included in this chapter.

When light is incident in an arbitrary direction on a dielectric material, the incident energy causes the molecules in the material to vibrate producing dielectric, or secondary, radiation. As both the incident and secondary waves propagate through the material they interfere with each other. The resultant wave has a group velocity different than that of the incident wave and thus appears to have changed velocity, emerging from the material later (in most cases) than would be the case if the light had propagated through the same volume of air. This is the origin of the refractive index of the material, the ratio of the speed of light in the material to the speed of light in a vacuum.

The angle of incidence of the light, coupled with this effective change in speed, leads to light bending when passing from one medium to another. This is refraction,

and can be readily observed in many day to day situations; a pencil appearing to bend in water is one of the most recognisable examples.

Refractive effects depend on the type of material through which the light is moving. For example, in an isotropic material, such as glass, the microscopic structure is uniform in all directions and light will pass through it in the same manner regardless of how it is incident on the material producing the familiar 'bent' rays of light.

For anisotropic materials (those whose microscopic structure varies depending on direction), however, light will travel along distinct paths depending on its polarisations properties, producing double refraction, whereby a single incident beam produces two emerging beams having passed through the medium. This effect is known as birefringence and the different directions in the medium have a different refractive index associated with them. Many naturally occurring crystals are birefringent and produce this effect.

Depending on the lattice structure in these crystals, they will have two (uniaxial) or three (biaxial) directions which have different refractive indices. In both of these types of crystals there is a special direction along which double refraction will not occur as the refractive index does not vary for different polarisations. This is the optic axis. Uniaxial crystals have a single optic axis, while biaxial crystals have two optic axes.

Passage of light along these axes produces a single refracted ray. One incident, one emergent. However, when light falls exactly along the optic axis, just as Hamilton predicted, it will emerge as a CD beam. The single emergent beam will have a

unique and unusual shape. This is due to the shape of the wave surface along the optic axis.

The wave surface is a surface traced out by the end points of all possible propagation directions within the crystal, with lengths corresponding to phase velocities. The surface consists of two shells, one an ellipse, the other a sphere, with four intersection points between them. The surface is shown in figure 2.2 for each two dimensional plane xy, xz and yz. The intersection points are all in the xz plane. (figure 2.2 (b)).

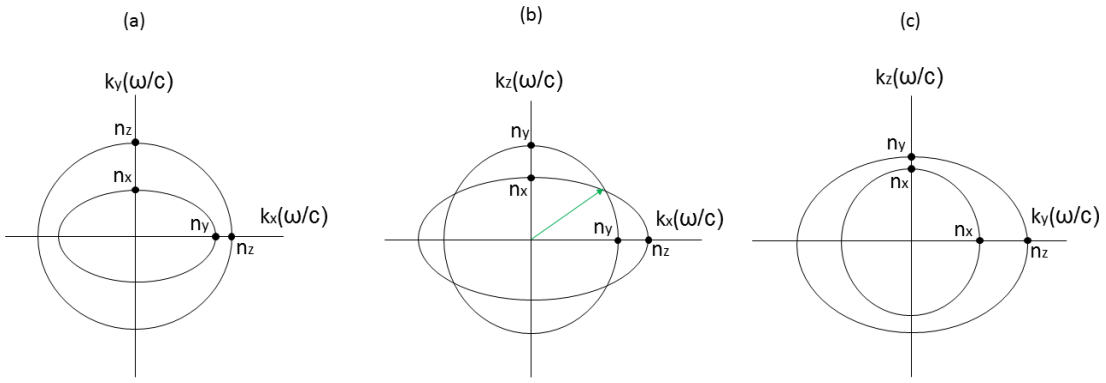

Figure 2.2 Wave surface diagrams for biaxial crystal in the (a) xy, (b) xz, and (c) zy planes. The xz plane is where the intersections between the wave surfaces, which give rise to CD, are located. The green arrow on (b) denotes the optic axis direction.

The optic axis is defined by the green line in fig. 2.2 (b), with another existing symmetrically about the z axis. They pass through the intersection points between the wave normal surfaces. These points of intersection have the shape of a double cone in three dimensions. It is due to this shape that CD occurs.

The index ellipsoid is a construction which defines the allowed directions of the displacement vector, **D**, of a wave propagating in direction, **k**. An ellipse drawn through the ellipsoid perpendicular to the direction s, will define the allowed **D**

directions by its semi axes. As shown in figure 2.3, if this direction **s** lies along the optic axis, the ellipse has eccentricity 0, i.e. it is a circle, and therefore does not have defined semi axes. Thus all directions about the circle are allowed directions for the displacement vector.

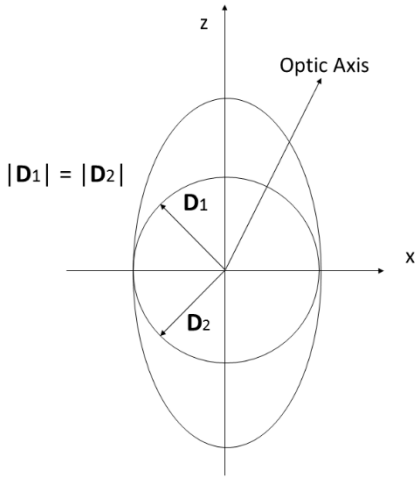

Figure 2.3 Index ellipsoid for a biaxial crystal. When light travels along the optic axis, the ellipse seegment through the ellipsoid is circular, meaning that there is no defined semi axes. This means that any direction of the displacement vector is allowed.

As light passes through the double cone, with wave vector direction **k** and, perpendicular to **k**, displacement vector **D**, the electric field vector **E** can be canted at an angle to **D** in the same plane as **D** and **k**. As noted in accordance with the index ellipsoid, **D** can lie in any direction, and thus **E** can also lie in any direction. The Poynting vector, **S**, which determines the direction of rays and transmission of energy lies perpendicular to **E**. This means that, as **D** rotates through all its allowed directions, **E** and **S** will also rotate and being canted at an angle, both trace out a cone, with energy lying on the cone traced out by the Poynting vector, **S**. This is illustrated in figure 2.4.

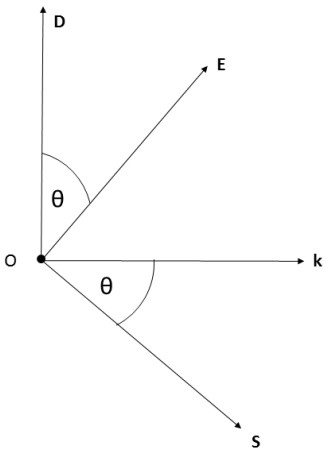

*Figure 2.4 Orientations of vectors in a biaxial crystal as light propagates in direction **k**. The electric field, **E**, and poynting vectors, **S**, are canted at an angle θ compared to the displacement field, **D**, and wave vector, **k**,*

From conics, and as outlined in Born and Wolf's Principles of Optics [37], the propagation of the beam, giving rise to the conical shape, can be described as follows.

As shown in figure 2.5 (adapted from figure 14.11 in [37]), **k** is the direction of the incident beam, **E** is the electric field vector, **S** is the Poynting vector, and O is the origin. α and β are the planes which lie perpendicular to **k** and along **E** respectively, with E', k', and S' being the points where **E**, **k**, and **S** cross the α plane. Firstly, using similar triangles E'k'O and Ok'S', the relationship between the lengths of lines E'k' and k'S' can be shown to be:

$$\mathrm{E'k'.k'S'} = \mathrm{Ok'^2} = \text{constant}$$

Meaning that as the propagation distance, Ok', increases, so too does the length of the line k'S'.

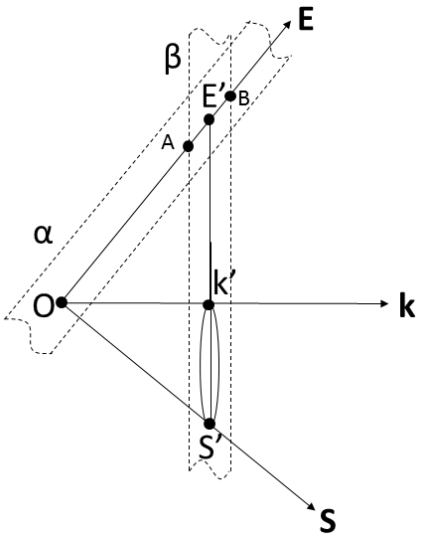

Figure 2.5 Geometrical representation of the propagation of the cone of light as the propagation distance increases. The center of inversion at k', and similar triangles E'k'O and Ok'S', give rise to an inverse curve at locus S'. This curve has the form of a circle which touches both k' and S'.

As the locus of E' is a straight line from A to B, and using k' as a center for inversion, the locus at point S' is a circle which lies on both k' and S' and has a tangent at S'. Thus as Ok' increases, the diameter of the circle, k'S', increases, and hence the rays which propagate in the direction of the Poynting vector, **S**, lie on a slanted cone represented here two dimensionally as the triangle Ok'S' and the circle with diameter k'S'.

Each point on the ring corresponds to a different polarisation direction, with a 90^{o} rotation in polarisation corresponding to a 180^{o} rotation about the ring. Meaning any two diagonally opposite points are orthogonally polarised, as indicated by the red arrows in figure 2.6.

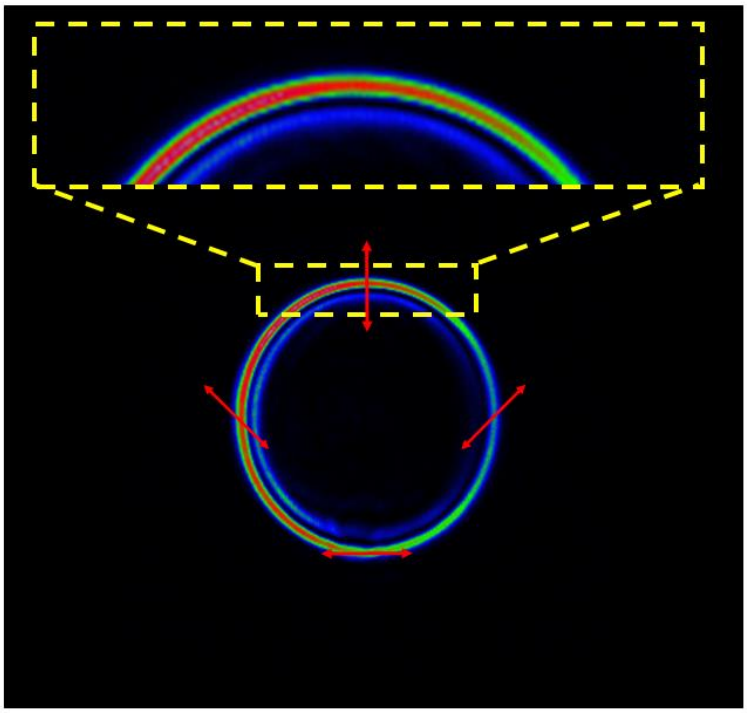

Figure 2.6 Typical ring pattern with polarisation indicated by the red arrows for points around the ring. The inset shows a zoomed in portion of the ring, showing the dark ring separated by two bright rings.

The observed ring is also, in actual fact, two closely spaced bright rings surrounding a central dark ring, inset of figure 2.6. This is due to light from directions very close to, but not precisely lying on, the optic axis giving rise to rings slightly offset from the ring itself. These slightly displaced rings are the two bright rings, as there is only a very small amount of light propagating along the actual optic axis. The ring produced by the light that falls precisely on the optic axis is observed as a dark ring with respect to the much brighter offset rings.

Observation of the phenomenon has also advanced in the last decade or so. The CD beam is now routinely viewed directly, in free space, with no imaging optics. The entire evolution of the beam can be observed outwith the crystal, conforming to neither Hamilton's internal nor external CD exactly, but illustrating features of both.

A rigorous mathematical derivation of the phenomenon based on the work of Berry is contained in appendix 1.

Useful parameters from this theoretical treatment, which are used in this experimental work, are the crystal strength parameter, ρ_0, and the dimensionless propagation variable, ζ, from which the ring radius, R, and Raman to Raman spot distance, Z_F, are derived, more detail on these variables is contained in the next section. In addition to this the intensity expression derived in appendix 1 is used in the theoretical comparison at the end of this chapter.

2.2 Experimental Section

The parameters of interest from Berry's work [30] are the ring radius, R, the distance from the ring plane to the Raman spot, Z_f, and the longitudinal shift introduced by the crystals. Figure 2.7 is a schematic showing the experimental apparatus and containing each of the parameters of interest.

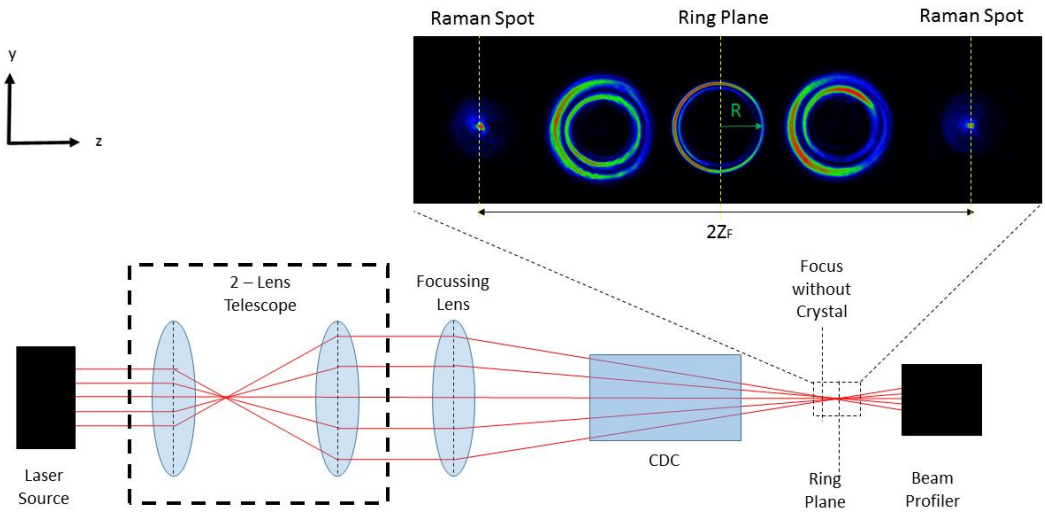

Figure 2.7 Experimental system used to observe single crystal CD. The laser source was either a 635 nm diode laser or a 633 nm Helium Neon laser depending on the experiment as noted in the text. A 2 lens telescope with magnification 2 was used only with the HeNe. A focussing lens with focal length 100 mm then focusses the beam (radius 13.6 μm) through the crystal (acceptance angle > 0.1°). A beam profiler, mounted on atranslation stage is then used to manually record the beam profile at various points along its propagation in free space. The inset images show the beam profile at the front raman spot, as it undergoes poggendorff splitting, the ring plane. The ring plane is a symmetry plane. The green arrow is the ring radius.

The longitudinal shift, Δ, is the difference between the systems focus without the crystal in place and its focus with the crystal in place. The focus with the crystal in place is designated the ring plane. The nature of the longitudinal difference introduced by the crystal is the same as that from any other optical material. As such it is found by the normal longitudinal shift equation from geometrical optics [37]:

$$\Delta = L\left(1 - \frac{1}{n_2}\right) \tag{2.1}$$

where L is the length of the crystal and n_2 is the intermediate refractive index.

The ring radius, R, (indicated by the green arrow in figure 2.7) and the Z_F parameter (shown below the beam evolution in figure 2.7) are taken from equations for the crystal strength, ρ_0, and the scaled distance parameter, ζ, as shown below. (Equations A1.14 and A1.17 in appendix 1.)

$$\rho_0 \equiv \frac{AL}{w} \tag{2.2}$$

$$\zeta \equiv \frac{L + (z - L)n_2}{n_2 k_0 w^2} \tag{2.3}$$

where ρ_0 is the aforementioned crystal strength, A is the semi angle, L is the length of the crystal, w is the radius of the incident beam waist, and z is the propagation distance. ζ is a dimensionless variable for the propagation distance in the field outwith the crystal measured from the ring plane.The ring radius, R, and the Z_f value are found using [26]:

$$R = AL \tag{2.4}$$

$$Z_F = \sqrt{\frac{4}{3}}\frac{2\pi}{\lambda}AwL \tag{2.5}$$

where A is the semi-angle of the cone of light propagating in the crystal, L is the length of the crystal, and λ is the wavelength of the incident light.

The hypothesis to be tested is that the parameters introduced in the recently advised theory conformed to experimentally measured values. The apparatus

shown in figure 2.7 was used to test these parameters. The collimated beam from a diode laser (2mW at λ = 635 nm) was used. This was coupled into a monomode fibre and has a spot of radius w = 13.6 μm ($1/e^2$) in the focus of an f = 100 mm lens (Newport KPX034).

The crystals used are of the monoclinic tungstate family, potassium gadolinium tungstate, ($KGd(WO_4)_2$ or, for simplicity, KGW). These crystals have high birefringence and almost equidistant refractive index values. The three distinct principle refractive indices for KGW at 632.8 nm were reported to be n1 = 2.01348, n2 = 2.04580, and n3 = 2.08608 [38]. This means that, as the differences ($n_2 – n_1$) and ($n_3 – n_2$) are small, refraction and diffraction effects can be considered paraxial. These properties make KGW an ideal candidate for good performance when used to produce CD. The aforementioned crystal strength parameter, ρ_0, is used as a measure of how well a given material can produce the CD pattern. For KGW, using the parameters of these experiments (L = 19.4 mm and w = 13.6 μm), $\rho_0 = 25.2$. The equivalent values for aragonite (as used in Lloyd's experiments) and for potassium titanyl phosphate (KTP) are 22.3 and 23.8 respectively [39]. The crystals used here were manufactured by Conerefringent Optics S.L. based in Barcelona, Spain [40]. They were rectangular cuboids with a cross section of 4 x 3 mm and were of the following lengths: L1 = 7.40 mm, L2 = 16.94 mm, L3 = 19.40 mm, and L4 = 24.50 mm.

In order to observe the phenomenon, the beam must pass along one of the optic axes of the crystal. To facilitate this the crystals were cut such that their end facets were perpendicular to one of the optic axes. The angular misalignment between

the optic axis and the end surface normal was 1.75 mrad, 1.25 mrad, 1.5 mrad, and 1.75 mrad for L1, L2, L3, and L4 respectively.

The sensor used to image the patterns was a Spiricon SP620U beam profiler with 1600 x 1200 pixel resolution. This is a USB silicon charge coupled device (CCD) camera with spectral response from 190 – 1100 nm and an active area of 7.1 mm x 5.4 mm [41]. These wavelength and size specifications make it suitable for all experiments carried out in this work and as such this beam profiler and the crystals are the essential pieces of equipment for this thesis.

In order to test the parameters, the crystal was placed after the lens and before its focus (approximately 3 cm from the lens). The crystal's position in the converging beam has no effect on the patterns, whereas the radius of the incident beam does. The crystal was placed such that its height was the same as that of the incident beam. The beam spot was aligned with the end face of the crystal. The beam profiler was placed beyond the crystal and moved along the z direction until the sharpest image was found. At this point a double refraction pattern will be observed on the live beam profiler output. Using this output as a guide, the adjustable screws on the crystal mount were used to rotate the crystal in the xy and yz planes. The pattern will transition from double refraction to two rounded lobes and finally to the characteristic Hamilton Lloyd pair of rings once the crystal is properly aligned and the beam lies along its optic axis (Figure 2.8). This is a non-trivial alignment procedure with an acceptance angle for the crystal of less than 0.1^{o}. The sensitivity of the operation is greatly aided by precise adjustment screws on the crystal holders and experience of the experimentalist.

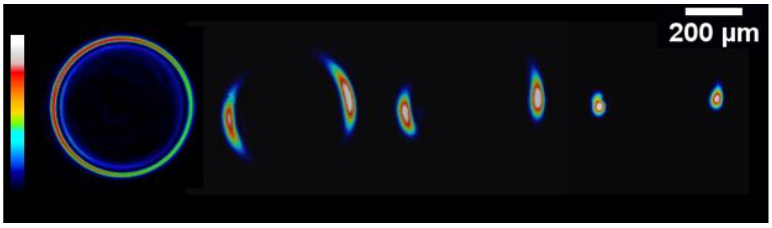

Figure 2.8 The transition from CD on the left to double refraction on the right. The points of double refracted light stretch into lobe type shapes before, quite suddenly, forming the ring.

In all experiments the crystal's pseudo vector **G** was oriented vertically upwards. The **G** vector is one of the unique properties of the effect. The vector is perpendicular to the direction of propagation of the beam and its magnitude is equal to the ring radius and thus dependent on the crystal length. The vector determines the lateral shift of the pattern and rotating the crystal will rotate the produced pattern about the incident beam position as shown in figure 2.9. For example, a crystal with the vector oriented vertically upwards (figure 2.9 (a)) will produce a pattern with the ring center directly above the incident beam position. Rotating the crystal clockwise as in the figure will rotate the entire pattern in the same direction.

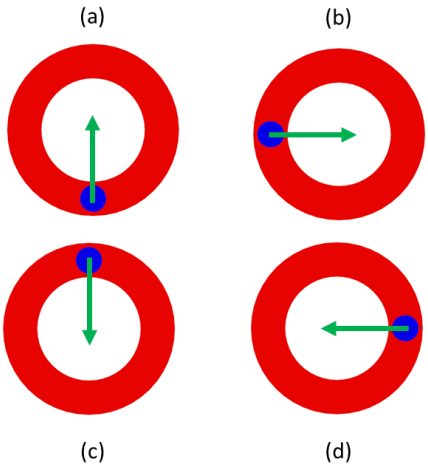

*Figure 2.9 Lateral shift of the ring position based on the crystal's **G** vector. The green arrow indicates the vector direction, while the blue spot is the position of the incident beam before undergoing CD. In the case of (a), the ring sits 'on top'of the incident beam position and is rotaed as the crystal's vector is rotated.*

Images were taken with no imaging optics directly from the beam profiler. The beam profiler was mounted on a mechanical travel translation stage (Newport M-436) allowing it to be moved along the propagation direction of the beam.

To measure the longitudinal shift, Δ, the position of the focus of the beam without the crystal was measured using the translation stage. Once the crystal was in place on the stage and aligned as above, the point where the Hamilton Lloyd rings were sharpest, and thus had the highest intensity peaks, was noted. The difference between these two measurements was the longitudinal shift.

The ring radii were taken by obtaining images of the ring pattern in the ring plane and measuring the distance between the highest intensity peaks.

The Z_F values were measured by noting the position of the ring plane on the stage and moving the camera until the highest intensity peak of the Raman spot was found. This distance is the Z_F value. This was done in conjunction with capturing the cross section.

This was obtained by manually taking images at 0.5 mm intervals over the range of the beam's free space evolution. The central columns of these image matrices were then extracted using MATLAB. This series of column arrays was then padded with zeroes to ensure uniform dimensions across all arrays and combined into a single matrix. MATLAB's 'averaging' image processing filter was then used to produce the final image.

The measurements of Δ, R, and Z_F were repeated for all crystals. The cross section was taken for L3 only.

In order to test the dependence of the pattern in the ring plane on the ratio of ring radius to incident beam radius, a slightly different architecture was used. The laser diode was replaced by a 633 nm Helium-Neon (He-Ne) laser (Newport R-30602), whose linearly polarised output, converted to circular polarisation with a λ/4 plate (AQWP05M-600 from Thorlabs), was collimated using a two-lens telescopic system with linear magnification of 2 (consisting of a 100 mm Newport KBX064 and 200 mm Newport KPX106). Lenses of various focal lengths (100 mm - KPX034, 150 mm - KPX064, 300 mm - KPX112, and 750 mm - KPX121) were used to produce a variety of spot radii at the beam waist. The spot radii ($1/e^2$ values) used were 75 µm, 110 µm, 193 µm, and 283 µm, giving values for crystal strength, ρ_0, of 4.5, 3.1, 1.8, and 1.2 respectively.

As the position of the focus of the system, without the crystal in place, and the location of the ring plane, once the crystal is added, are both determined using the intensity measurement provided by the Beamgage software that accompanies the Spiricon SP620U beam profiler, the error in that measurement contributes to potential error in the location of the ring plane. As further measurements (Z_F and Δ measurements), are made relative to the ring plane, this potential error is further compounded. The measurement of the ring radius was again made utilizing Beamgage software to determine the point of highest intensity and measure the diameter across the ring.

Beamgage estimates its accuracy to within 1%, estimated to correspond to an error in the position of both the ring plane and the systems focus, of ± 0.5 mm. The error associated with using the Vernier scale on the translation stage was ± 0.25 mm.

Allowing ± 0.25 mm for random and human error, the estimated error in the Δ measurements was ± 2 mm.

For measurement of Z_F, the location of the front and back Raman spot was identified in a similar fashion using Beamgage and thus introduced additional error of the same amount of ± 0.5 mm for both the front and back Raman spots. This gives an estimated error of ± 0.5 mm for each position determination, of which there are 3, and ± 0.25 mm for each measurement made with the Vernier scale, a total of 5, as well as an additional ± 0.25 mm for human error, giving an estimated error of ± 3 mm.

In the case of the ring radius measurements the estimated 1% error from Beamgage corresponds to a potential error in the position of the intensity maxima on the ring. In addition to this the markers used for measurement in the software are manually placed on the live feed of the beam profile from the profiler. As the ring thickness was approximately the width of the incident beam radius (in this case 13.6 ± 0.2 μm), and has an approximately Gaussian distribution, a decrease of 1% in intensity corresponds to approximately a ± 0.7 μm change in position or ≈ 5% error. This is present for both sides of the ring introducing an estimated error of 10% of the incident beam radius into the measurements of the ring radius. Allowing an estimated ± 1 μm for human error in the placement of the measurement markers, this gives an estimated error of ± 2.5 μm in the ring radius measurements.

2.3 Results

2.3.1 Ring Plane Patterns

The Hamilton-Lloyd pair of rings was observed in the ring plane for 4 different crystals. Figure 2.10 shows the pattern in the ring plane as well as Poggendorff splitting and the Raman spot for crystal 1 (L1= 7.4 mm) and crystal 2 (L2 = 16.94 mm), while figure 2.11 shows the patterns for crystals 3 and 4 (L3 = 19.4 mm and L4 = 24.5 mm). The direction of propagation in all images is from left to right as indicated by the green arrow.

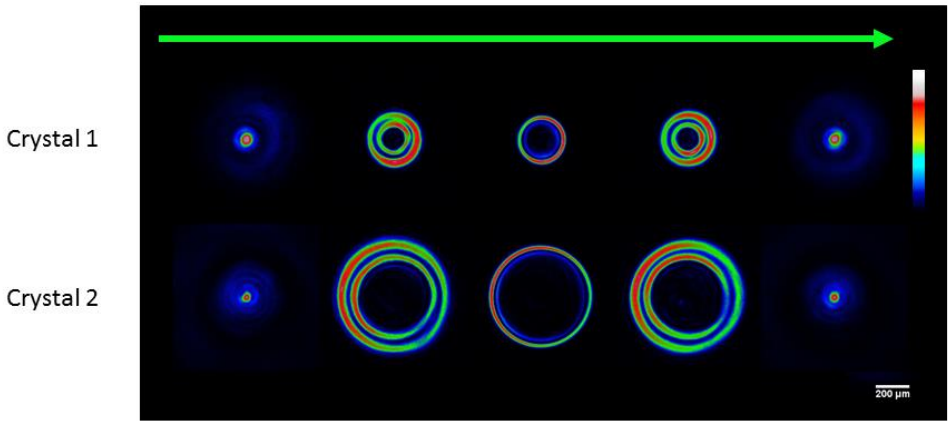

Figure 2.10 Ring patterns at 5 points along the beam path using crystal 1 and 2. The green arrow is the direction of propagation of the incident light.

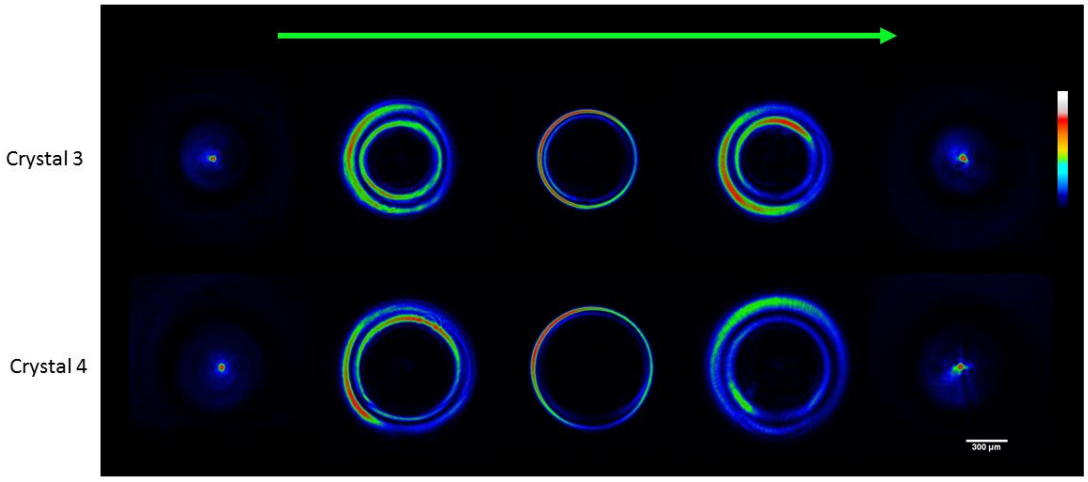

Figure 2.11 Ring patterns at 5 points along the beam path using crystal 3 and 4.

2.3.2 Longitudinal Shift, Δ

The first parameter measured was the longitudinal shift introduced by the crystal. The longitudinal shift is the same as that from geometrical ray optics, and as such the theoretical values were obtained using the standard formula (2.1). The experimental values were found to be in good agreement with the theoretical values. Figure 2.12 shows a comparison of the values shown in table 2.1.

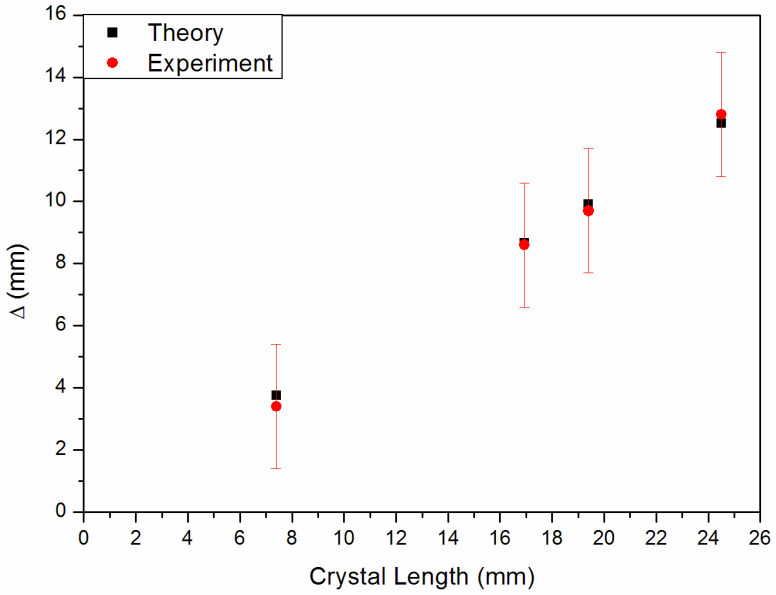

Figure 2.12 Comparison of theoretical (black squares) and experimental (red circles) values for longitudinal shift for all crystals (1-4)

	Δ (mm)	
Crystal Length (mm)	Theory	Experiment
7.40	3.75	3.4 ± 2
16.94	8.66	8.6 ± 2
19.40	9.92	9.7 ± 2
24.50	12.52	12.8 ± 2

Table 2.1 Theoretical and experimental values of longitudinal shift for each crystal (1-4)

2.3.3 Ring Radius

The ring radius is measured from peak to peak of the intensity profile of the ring pattern in the ring plane as shown in figure 2.13. The theoretical ring radius is given by (2.4). The theoretical and experimental values were found to be in good agreement with each other, all values were within ±6.5 µm of each other with a maximum percentage error of less than 2%. Figure 2.14 shows a comparison of the theoretical and experimental values shown in table 2.2.

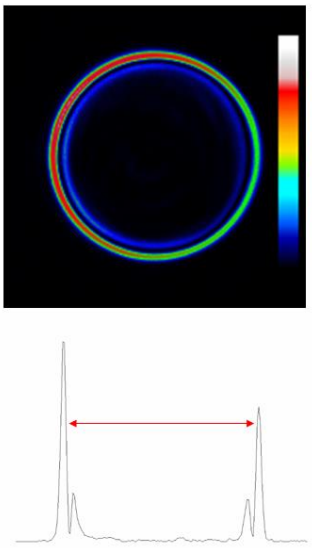

Figure 2.13 The peak to peak distance was measured to determine the ring radius.

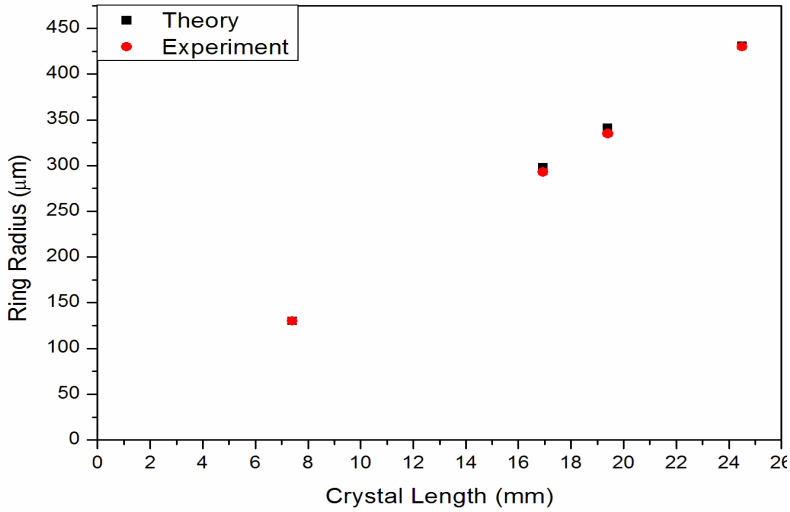

Figure 2.14 Comparison of theoretical (black squares) and experimental (red circles) values for ring radius for all crystals (1-4)

	Ring Radius (µm)	
Crystal Length (mm)	Theory	Experiment
7.40	130.23	130 ± 2.5
16.94	298.14	293 ± 2.5
19.40	341.33	335 ± 2.5
24.50	431.16	430 ± 2.5

Table 2.2 Theoretical and experimental values for ring radius

2.3.4 Distance from ring plane to Raman spot, Z_F

Z_f is the distance from the ring plane to the appearance of the Raman spot. The theoretical value is given by (2.5). The experimental value is obtained using a translation stage to measure the distance between the ring plane and the brightest point of the Raman spot. With the ring plane being a symmetry plane the forward and backward Z_f distance is equal. In this case the distance from the ring plane to the back Raman spot was measured for each crystal. Figure 2.15 shows a comparison of the theoretical and experimental values shown in table 2.3.

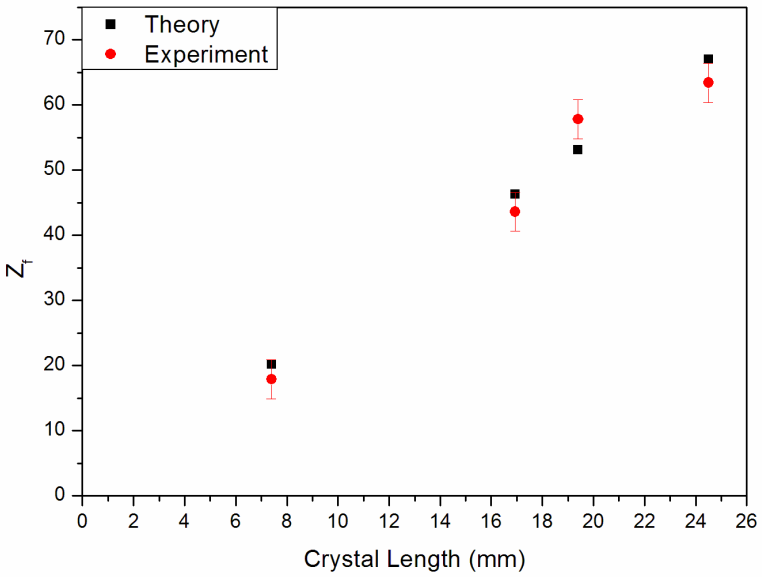

Figure 2.15 Comparison of theoretical (black squares) and experimental (red circles) values for Z_f for all crystals (1-4)

	Z_f (mm)	
Crystal Length (mm)	Theory	Experiment
7.40	14.4	16.4 ± 3
16.94	32.97	33.8 ± 3
19.40	37.75	33.5 ± 3
24.50	47.68	45.3 ± 3

Table 2.3 Theoretical and experimental values for Z_f

2.3.5 Cross Section

To see these parameters simultaneously the cross section of the propagating beam was taken. This showed the full range of the beam, corresponding to a length of $2Z_f$. The evolution in free space of a Gaussian beam conically diffracted by crystal 3 (L3= 19.4 mm) is shown in figure 2.16. From the front Raman spot the beam transforms into the Poggendorff rings creating a so-called bottle beam about the ring plane, before transforming back through Poggendorff rings to the back Raman spot. The beam is formed by two oppositely propagating cones, their point the Raman spot, their base the sharpest point of the ring plane. The overlap of the cones gives rise to the diffuse Poggendorff rings. This image was obtained by taking images at 0.5 mm intervals along the beam path by manually adjusting the translation stage position. The central column, as highlighted in red in figure 2.16, was then extracted from each image and these columns then stacked using MATLAB. Finally

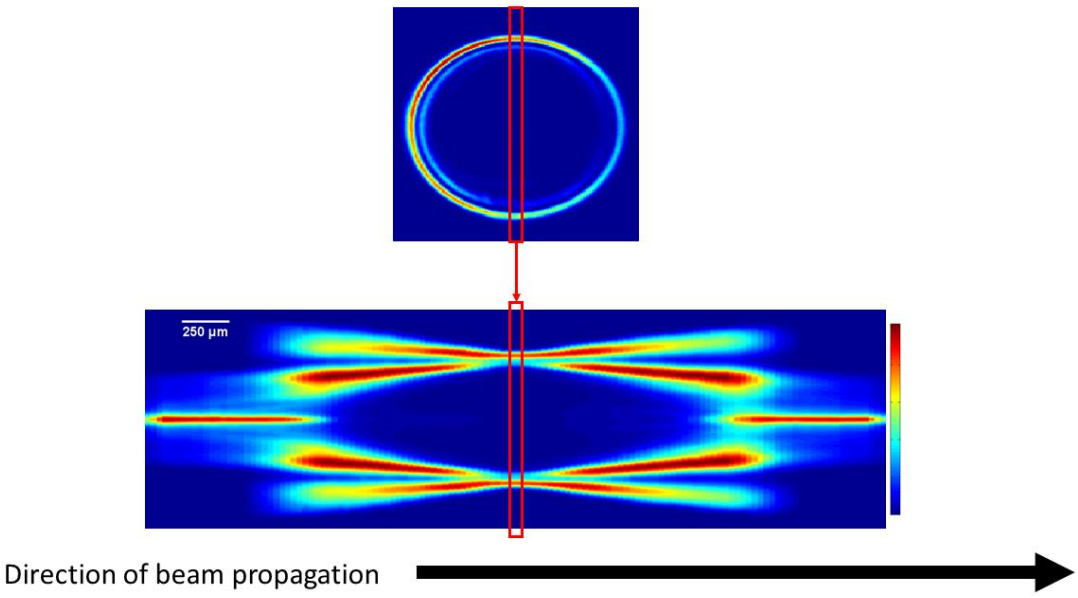

Figure 2.16 The shape of the CD beam in free space. The cross section reveals the 'bottle-beam' and the intersection of two cones of light.

an ‘averaging’ smoothing filter was applied to smooth the edges where the images were slightly misaligned to create the final image. This MATLAB code (C1) can be found in the appendix 4.

2.3.6 Poggendorff Free Ring Pattern

The effects of the ratio of the radius of a CD cylinder to the beam waist of the incident beam on the pattern produced was investigated to ascertain if the predictions of [36] held true. Those predictions state that the pattern observed in the ring plane depends on the incident beam size and that for sufficiently large incident beam size a large single ring with a dark central region will be observed. Figure 2.17 shows the CD patterns for four ρ_0 values as the incident spot size was increased, along with radially averaged images to give a clearer view

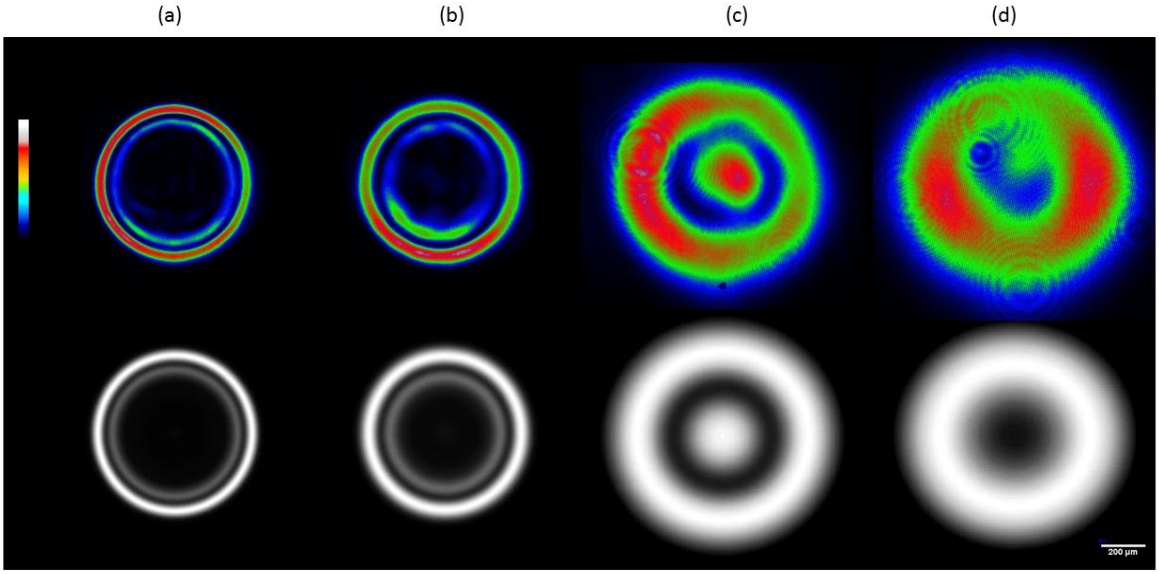

Figure 2.17 Patterns produced for different ρ_0 values, (a) ρ_0 = 4.5, w = 75 µm, (b) ρ_0= 3.1, w = 110 µm, (c) ρ_0 = 1.8, w = 193 µm, and (d) ρ_0 = 1.2, w = 283 µm. The images on the left are directly from the beam profiler, while the images on the right are radially averaged images to afford a clearer view of the changes with decreasing ρ_0.

of the effect. As ρ_0 decreases it can be seen that the typical CD pattern (fig. 2.17a) becomes more diffuse (fig. 2.17b) until the inner ring radius falls to zero producing a bright central spot (fig. 2.17c) before finally the spot disappears altogether leaving a thick bright outer ring with a dark central area (fig. 2.17d).

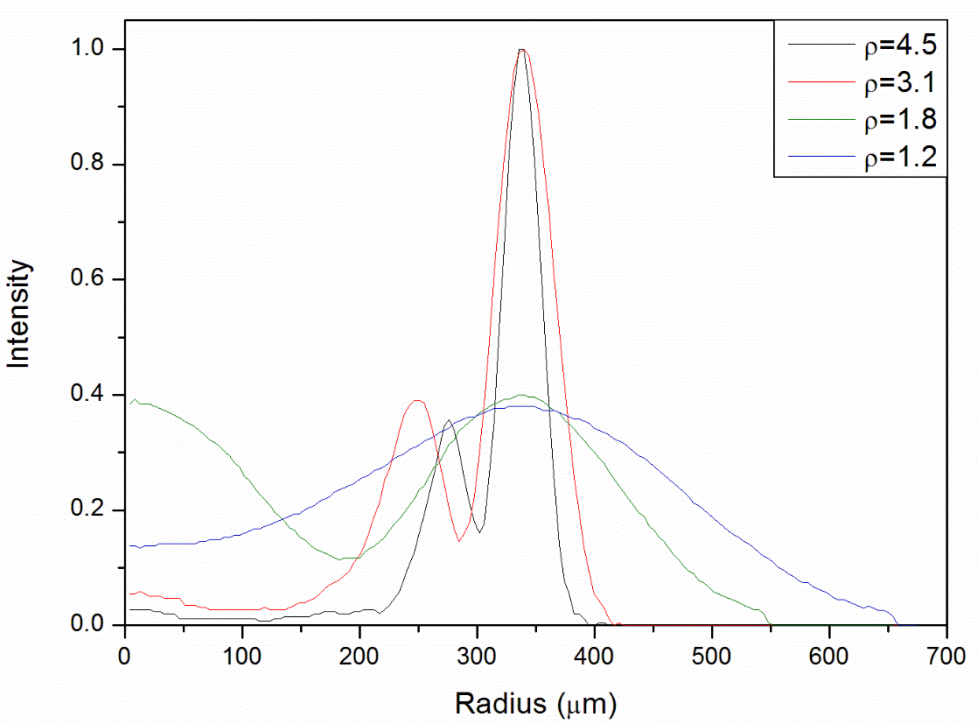

Figure 2.18 Intensity profiles of radially averaged images for different ρ values. Higher ρ values give the familiar CD pattern, while lower values lead to spread out, diffuse rings producing a single ring surrounding a bright spot, and a single ring with no central intensity as ρ gets smaller.

The dark central area and bright ring appear when the incident spot size and the cylinder radius are approximately equal. Figure 2.18 shows the intensity profiles of the radially averaged images obtained using ImageJ and custom MATLAB code written by Dr. Guang Tang of the MAPS group in the University of Dundee available in appendix (C2). The intensity, as expected, drops off for the more diffuse rings (ρ_0 = 1.2, 1.8) when compared to the more typical CD pattern (ρ_0 = 3.1, 4.5).

2.3.7 Comparison with theory

Figure 2.19 shows the theoretical intensity profiles of the four crystals used in this chapter.

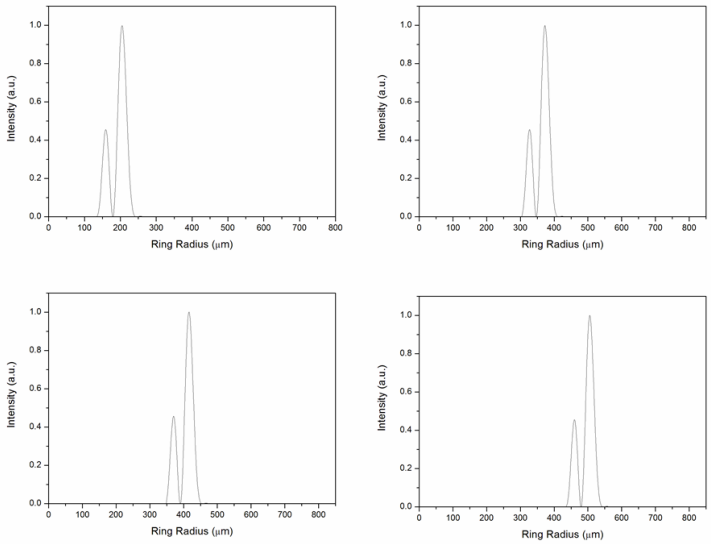

Figure 2.19 Intensity profiles calculated using equation (2.6) as implemented with code C3 for the four biaxial crystals used

These were calculated using equation (2.6).

$$I_{rings} = \frac{2}{\rho_0(1+\zeta^2)^{3/4}}\left|f\left(\frac{\rho-\rho_0}{\sqrt{1+i\zeta}}\right)\right|^2 \qquad (2.6)$$

The intensity profiles were generated using code (C3) in appendix 4, an excerpt of which is shown below:

```
for o=1:1:numel(p)
          s(o)=(p(o)-p0)/(sqrt(1+i*Zeta));
          K3=besselj(3/4,(0.25*(s(o))^2));
          K1=besselj(1/4,(0.25*(s(o))^2));
          I3=besselj(3/4,(0.25*(s(o))^2));
          I1=besselj(1/4,(0.25*(s(o))^2));
          fun(o)=(1/(4*sqrt(2*pi)))*(abs(s(o)))^(3/2)*exp(-
          0.25*(s(o))^2)*(K3+(sign(s(o))*K1)+(pi*sqrt(2)*heaviside(s
          (o))*(I3-  I1)));
          Irings(o)=(2/(p0*(1+Zeta^2)^(3/4)))*(abs(fun(o)))^2;
end
```

This portion of code combines the variables in equation (2.6), as outlined in appendix 1, equation (A1.19 – A1.23), and calculates the intensity of the ring at a single point along it's circumference. This value for `Irings` is then drawn about the whole ring to produce theoretical ring pattern images for crystals of various sizes.

Figure 2.20 Theoretical images produced using the intensity profiles shown in 2.19.

This is the most basic theoretical model used in this work as it is to describe the simplest case of a single crystal with unpolarised light (UPL). The addition of more complicated experimental methods is reflected in later sections with more detailed theoretical models.

2.4 Discussion

The results confirmed various aspects of the recently advised paraxial theory as described by Berry [30], and the prediction by Belsky and Stepanov [36]. The various parameters of interest compared favourably with the expected theoretical values and trends for the factors tested. Consideration of these parameters together gives a better overall picture of the CD phenomenon in terms that are simple to understand and practically applicable. The facility to theoretically predict, quickly and easily, the broad features of a CD beam is essential to experimental design and allows for a much lower barrier to entry into CD experiments. This is an important aspect of any field as practicality of use is paramount when considering potential applications.

A number of experiments using single crystal CD exploring other avenues of research have been described in the period covered by this work including white light CD [42] and using an incident top hat beam rather than a Gaussian beam [43].

The use of white light to produce CD results in a pattern that is effectively the superposition of diffracted beams for each constituent wavelength of light. Blue light is double refracted and red light is conical diffracted. Intermediate points undergo diffraction at various points in the transition between double and CD. The ring radius and position of the ring plane were both shown to vary with wavelength in accordance with the differences in refractive index for the different wavelengths that make up white light.

Having the incident beam have a top hat profile gives rise to a high intensity inner ring and an outer wedge shaped feature. This showed that the structure of the

produced CD pattern strongly depends on the profile of the incident beam and altering it can produce strikingly different effects in the ring plane pattern.

The results shown in this chapter set the foundation for the rest of the work carried out in this thesis. The goal of this more fundamental work was to provide insight and experience into the production of a CD beam using biaxial crystals and the various parameters governing the appearance and characteristics of that beam. In a broader sense fundamental work like this establishes a base from which practical applications can be built by confirming or refining the theoretical area of the field. The stronger the theoretical understanding of the phenomenon the more possibilities exist for it to be exploited into a tangible expansion into the practical space.

2.5 Summary

In this chapter a number of parameters were investigated using four biaxial crystals to verify the recently advised paraxial theory [30]. Images from the ring plane are presented along with experimental and theoretical values for the longitudinal shift Δ, the ring radius R, the length of the evolution from Raman Spot to ring plane Z_F, and the image of the cross section for the beam in free space. There was good agreement in all cases between the theoretical values obtained from simple expressions extracted from Berry's paraxial theory and the experimentally registered values. The prediction of Belsky and Stepanov was also investigated and the effect of the ratio of r/w was shown to be as theoretically predicted in [36].

3 Cascade Conical Diffraction

The next step to advance from single crystal conical diffraction (CD) is to consider the effect of adding additional crystals to the experiment. To do this, a cascade of two or more crystals is used. The parameters of interest are the same as in the single crystal case so as to facilitate direct comparison between the two. Once again, the cross section is also investigated. Additionally an alternate experimental setup is used to illustrate the potential of alternate optical configurations.

Figure 3.1 Ring pattern from a two crystal cascade system.

3.1 Introduction

In this chapter the effects of additional crystals on the CD beam are investigated. Preliminary demonstrations of this aspect of the phenomenon by Prof Amin Abdolvand at the University of Dundee led Michael Berry to develop a theoretical description in 2010 [17]. This description is outlined in appendix 2. The initial observations which were demonstrated to him at that time were subsequently published the following year in [44]. The field of CD lasers stems from cascade CD and a patent for the initial CD laser design [45] was awarded to those same University of Dundee researchers. The work in this thesis was carried out between 2012 and 2015 leading to the work contained in [32]. In the interim a number of applications [25], [47], a new theoretical model [48], and a new experimental set up [49] have been proposed.

Cascade CD occurs when two or more crystals are arranged in series and light propagates along their common optical axis. When light is passed through the first crystal, the typical CD pattern, as seen in chapter 2, is observed.

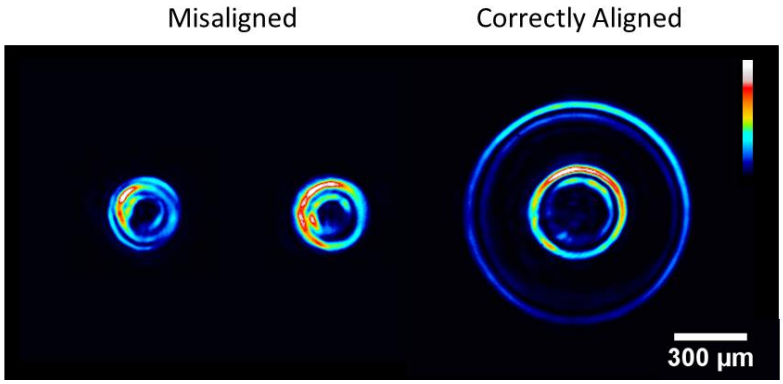

Figure 3.2 The double ring pattern observed when the second crystal is misaligned. The first crystal produces CD rings which are subsequently double refracted by the second crystal. When aligned the two rings come together to form the cascade CD ring pattern on the right.

Upon passing, in an arbitrary direction, through the second crystal, double refraction occurs. However, in place of the two beams with the incident beam's profile, two rings are observed corresponding to the CD beam from the first crystal, as shown on the left hand image in figure 3.2.

Aligning the second crystal so the light passes along the optic axis gives rise to a pattern consisting of 2^{N-1} concentric rings, where N is the number of crystals in the cascade [44], as depicted in the right hand image in figure 3.2.

A method to gain an understanding of this aspect of the phenomenon has been utilized by Loiko et al. [50] and in the master's thesis work of A.Turpin [51]. It involves filtering of the CD beam after the first crystal in a cascade and determining the corresponding pattern produced after the second crystal when only a small segment of the first CD ring propagates through it.

For example in figure 3.3, (a) is the CD ring after the first crystal in a cascade, and (b) is the CD ring pattern after the second crystal. The coloured rings represent the part of the ring allowed through the filter in (a), and the corresponding parts of the rings illuminated in the cascade pattern in (b).

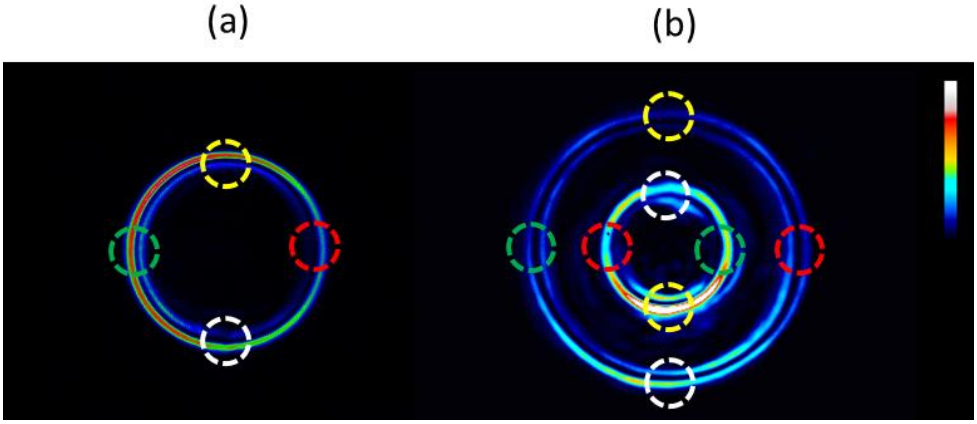

Figure 3.3 Ring patterns after (a) 1 and (b) 2 crystals. The colured circles show the section of the first ring which gives rise to two sections of the second pattern, one on each of the two rings.

The pattern observed using this method is not dissimilar to a double refraction pattern, i.e. just the parts of the pattern enclosed in red circles in figure 3.3 will be seen after the second crystal, as represented schematically in figure 3.4. Here, the coloured area shows the filtered and observed sections after the first and second crystals respectively.

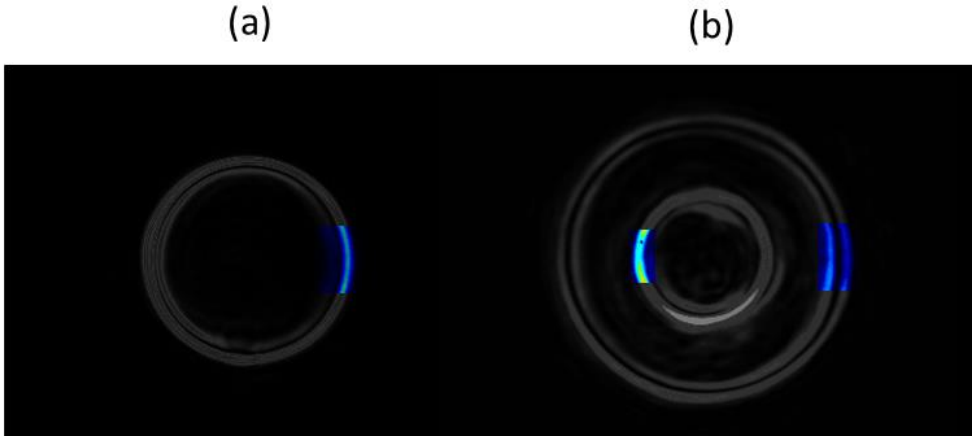

Figure 3.4 Schematic representative of the pattern observed if only a filtered section of the CD ring after a single crystal is allowed through the second crystal. The colured area on (a) is what is allowed through the filter. This will produce the coloured area of (b) after the second crystal, indicating that a single point on the first CD ring gives rise to two points in a cascade CD pattern.

This shows how a two crystal cascade produces two rings, as each point on the CD ring after the first crystal produces one point on *each* of the rings in the final pattern. Moving the filter on the CD ring after the first crystal to different positions (i.e changing from the red circled area to the green, yellow, white or any intermediate point) moves the segments observed on the emergent beam after the second crystal. Thus, tracing this pattern from every point on the single crystal CD ring gives rise to the pattern of 2^{N-1} rings observed in the ring plane of the system as a whole.

3.2 Experimental Section

Using the available crystals to create cascades of two, three and four crystals allowed for imaging of the more intricate ring plane patterns obtained with multiple crystals. The parameters of interest are shown in figure 3.5. They are the same as those in chapter 2 for the single crystal case with the exception of the ring radius. Using a cascade of N crystals to produce CD should lead to the production of 2^{N-1} concentric rings [17]. In figure 3.5, an inner and outer ring radius is annotated on the schematic, this is the case for a two crystal cascade.

In order to observe cascade CD patterns, the system shown in figure 3.5 was used. It is similar to that shown in fig 2.7 in chapter 2 for single crystal CD with the addition of multiple crystals to produce the cascade. As before, the ring plane images were registered with no imaging optics using the Spiricon SP620U beam profiler.

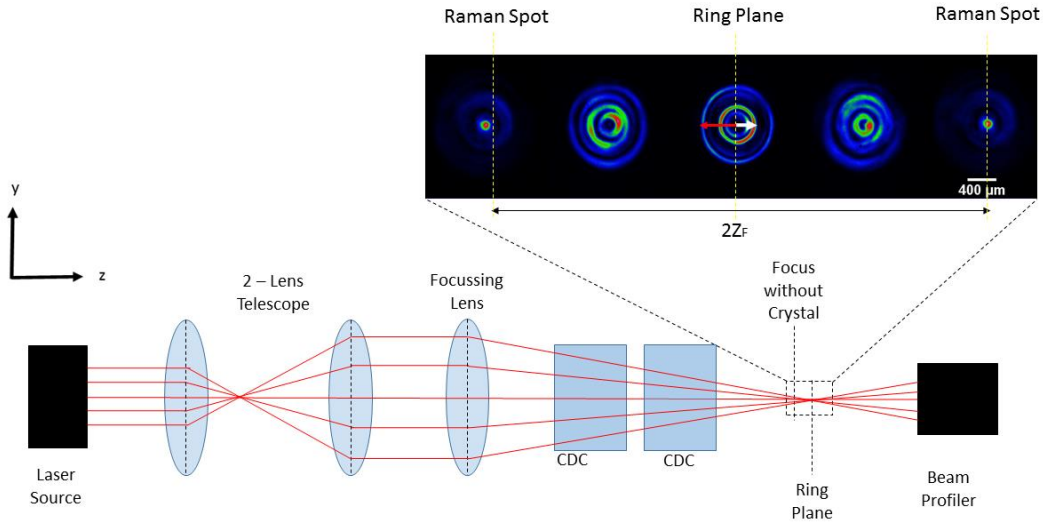

Figure 3.5 Schematic experimental apparatus used to observed cascade CD. The system is the same as that used for single crystal CD (figure 2.7), but with the addition of a second (or more) crystals. The red and white arrows indicate the outer and inner ring radii respectively.

Most parameters were measured in the same manner as those for the single crystal case, using the translation stage to allow movement and measurement along the direction of beam propagation. The main difference between the single crystal and cascade experiments was the range over which the measurements were taken, being larger in the case of the cascade experiments.

The cross section was captured using the same method as before however placement of the translation stage was more critical in the cascade case; if the range of the free space evolution is larger than the range of the translation stage, the stage needs to be repositioned during measuring the cross section. This can lead to a slight 'kinks' or a discontinuity in the final cross section image due to any difference in alignment that may not be perceptible until the final image is constructed as shown in figure 3.6.

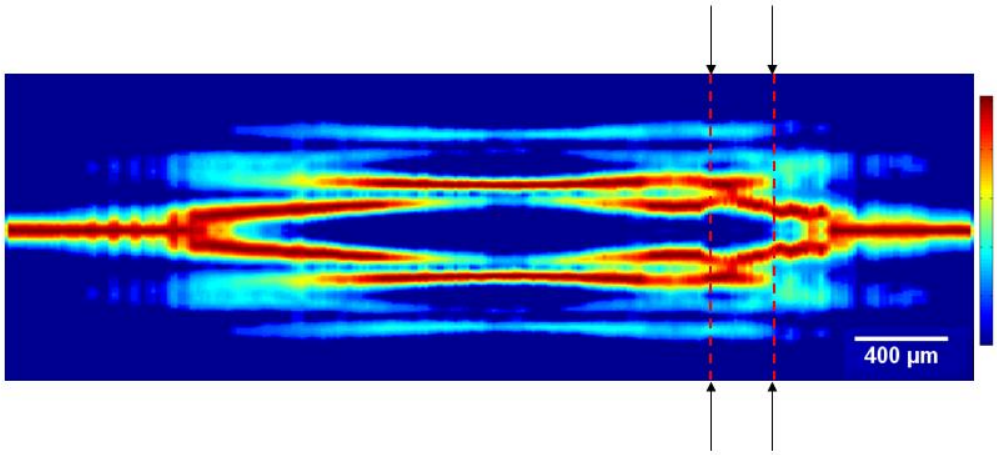

Figure 3.6 Effect of poor stage placement on cross section of a cascade system. The indicated areas show a 'kink' or discontinuity in the cross section due to movement of the translation stage during recording of the images.

The errors in this chapter are the same as those from the single crystal work in section 2.3, as the same system and method was used to measure the parameters for the cascade experiments.

3.3 Results

3.3.1 Ring Plane Patterns

The ring patterns shown are images from the ring plane for various combinations of two crystal cascades as well as three and four crystal cascades. Figure 3.7 shows the effect of crystal orientation on a two crystal cascade (L2 & L4).

In this case the first crystal always had its pseudo vector, **G,** oriented vertically upwards (y direction in figure 3.5) and the second crystal's G vector was oriented at 90^{o} to this (x direction in figure 3.5).

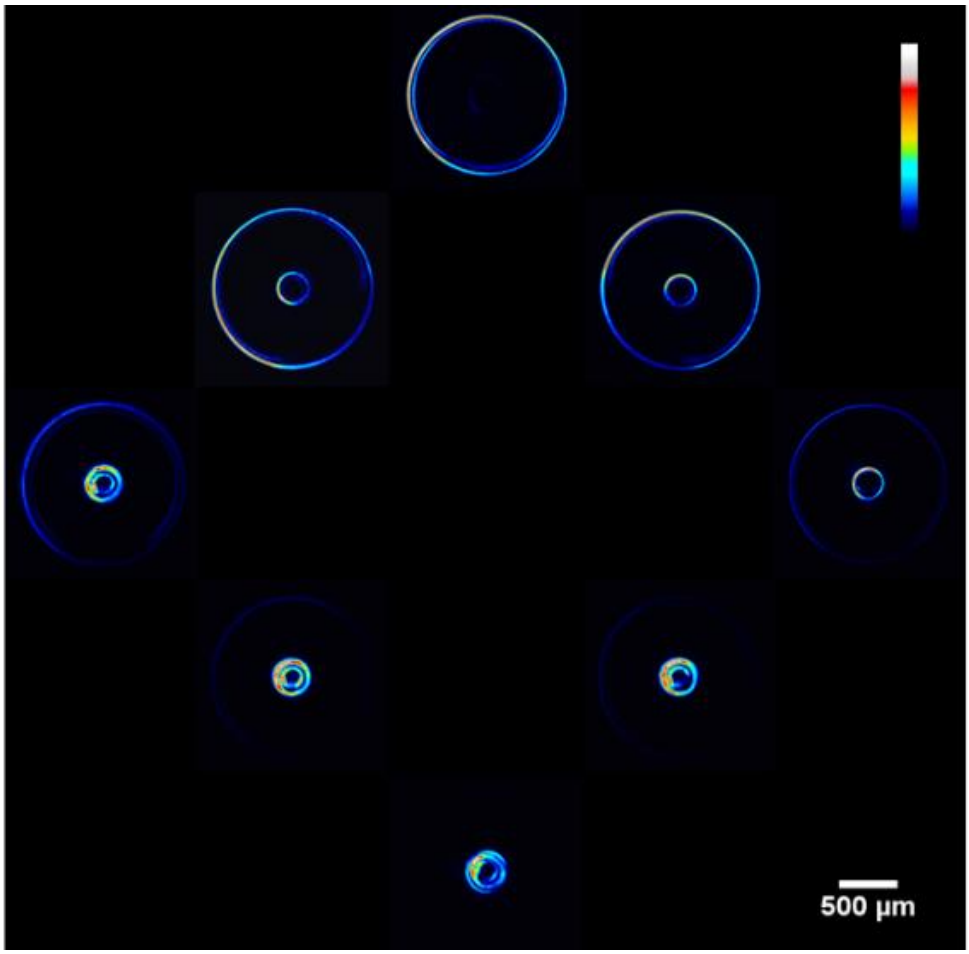

Figure 3.7 Ring plane patterns for a two crystal cascade as the second crystal's pseudo vector is rotate through 360^{o}

Figure 3.8 shows ring plane patterns for two crystal cascades with various crystal combinations (L1 & L2, L1 & L3, L1 & L4, L2 & L3, L2 & L4, and L3 & L4). There is no difference in the obtained pattern when the order of crystals is changed as seen with cascade configurations with descending crystal length (L3 & L2 and L4 & L3). This marks a particular, special case wherein the use of circularly polarised light (CPL), and observing the pattern in the ring plane, eliminates differences introduced by the order of the crystals.

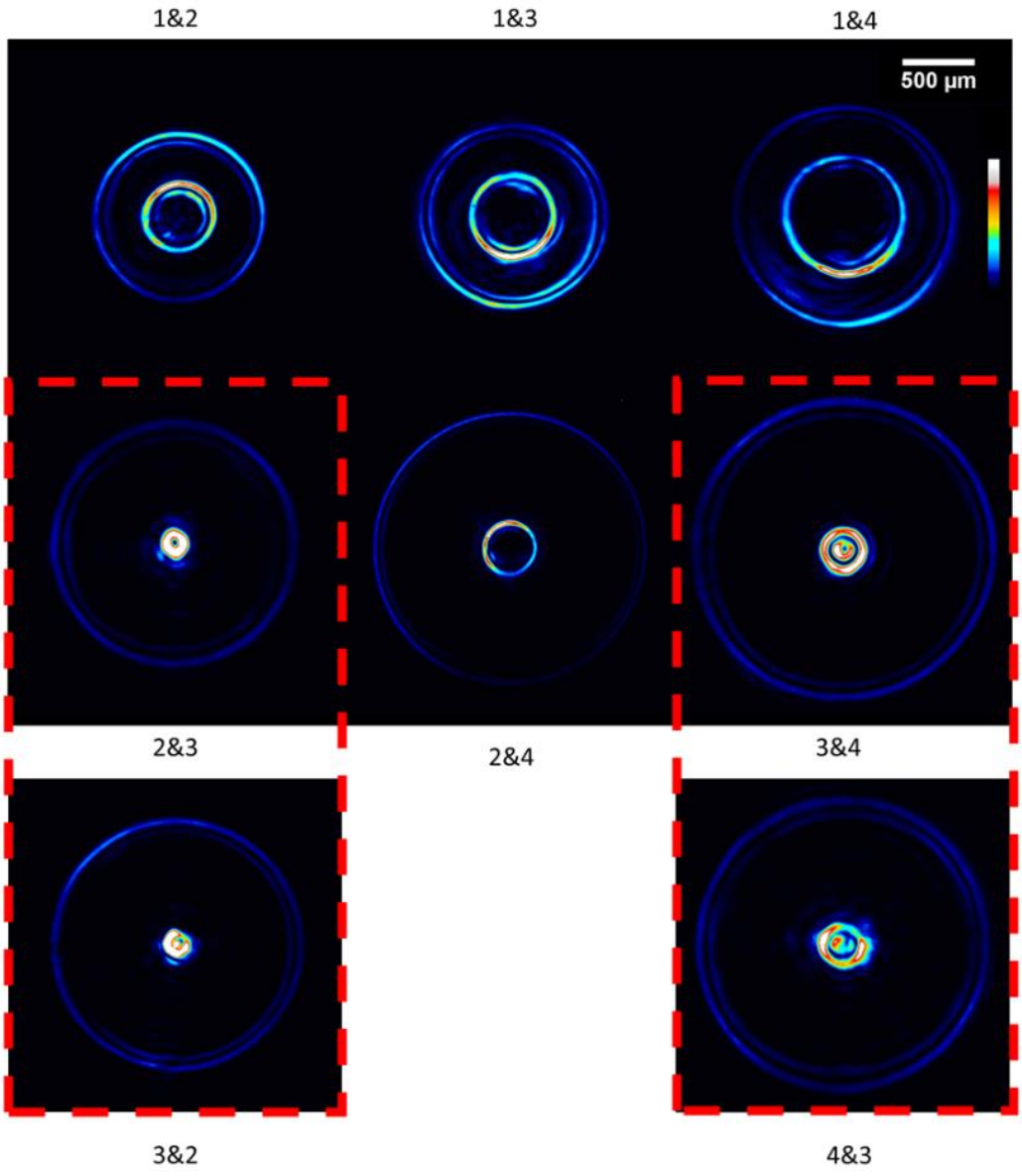

Figure 3.8 Cascade patterns for all two crystal combinations of the four available crystals. The bottom images show that the order of the crystals in the cascade does not affect the ring radii

Figure 3.9 shows a cascade consisting of three crystals and one consisting of four crystals. As the images are more spread out and the relative intensity of the rings is lower in this case, the intensity about the ring is inconsistent. Due to this, a radially averaged version of each image is included to illustrate the ring pattern more clearly. All angles between each subsequent crystal in the cascade were, in this case, equal to 90^{o}.

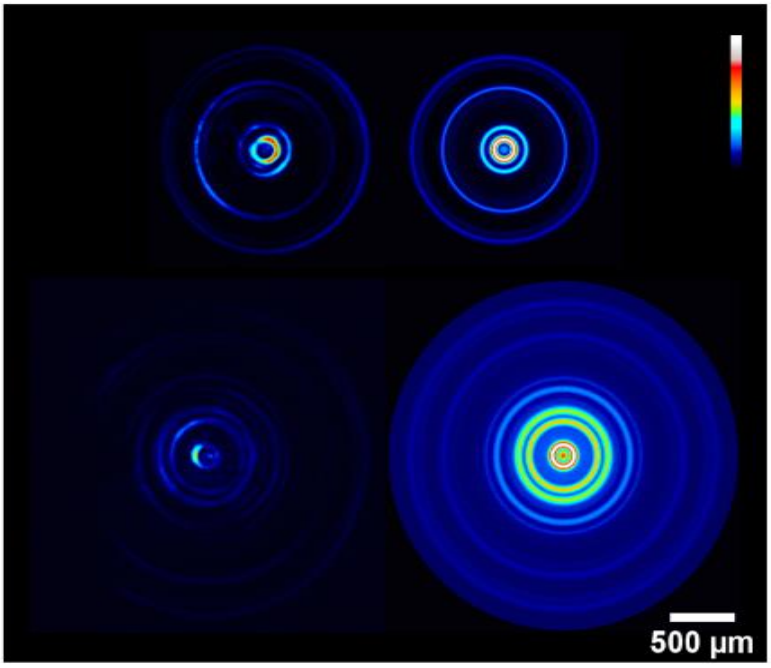

Figure 3.9 Three and four crystal cascade images. The three crystal cascade produces a pattern with 4 concentric rings, while the four crystal cascade produces 8 concentric rings. The left hand images are raw data from the beam profiler, whereas the right hand side are radially averaged images.

3.3.2 Longitudinal Shift, Δ

The Δ values as measured were simply the sum of those for the individual crystals in whatever combination they are used. This holds for any combination of any number of crystals. Figure 3.10 shows the comparison between theoretical and experimentally measured values for longitudinal shift for all two crystal combinations shown in figure 3.8, with the measured and theoretical values shown in table 3.1.

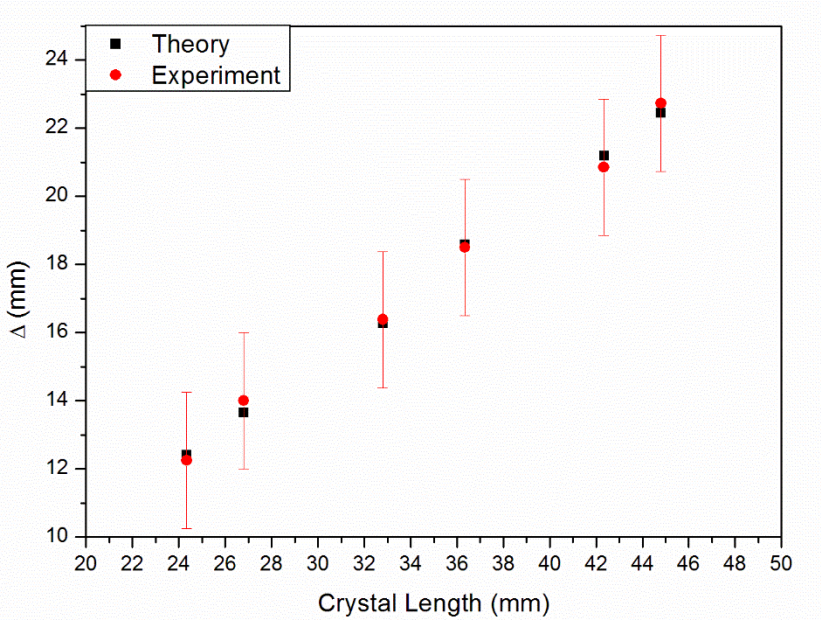

Figure 3.10 Comparison of theoretical (black squares) and experimental (red circles) values for longitudinal shift for all crystals combinations in figure 3.5

	Δ (mm)	
Combined Crystal Length	Theory	Experiment
24.34	12.4	12.3 ± 2
26.80	13.7	14.0 ± 2
31.90	16.3	16.4 ± 2
36.34	18.6	18.5 ± 2
42.34	21.2	20.9 ± 2
44.80	22.4	22.7 ± 2

Table 3.1 Theoretical and experimental values of longitudinal shift for each crystal combination

3.3.3 Ring Radius

The ring radius was found by the same method used in chapter 2 for single crystal CD.

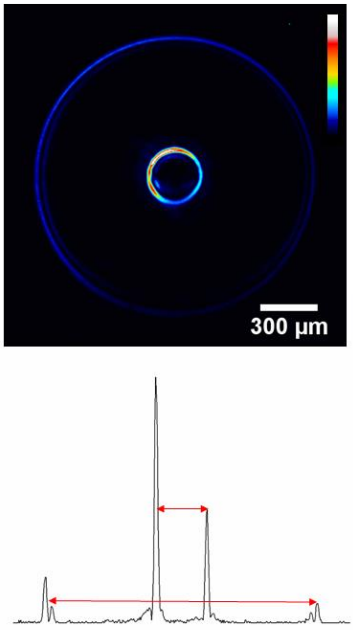

Figure 3.11 Peak to peak distances for the inner and outer ring radius measurements

Figure 3.11 shows the intensity profile for the two crystal cascade (L2 & L3). The transition from double refraction to CD is shown in Figure 3.12. The two spots usually observed for double refraction are in this case replaced with two CD patterns. The center point of these smaller ring patterns lies on the ring created by the second crystal. In this way it can be seen that the inner and outer radii arise from the radius of the first crystal (yellow line) minus and plus the radius of the second crystal (red line) respectively. This gives rise to the two observed concentric rings at the positions shown (green dashed circles).

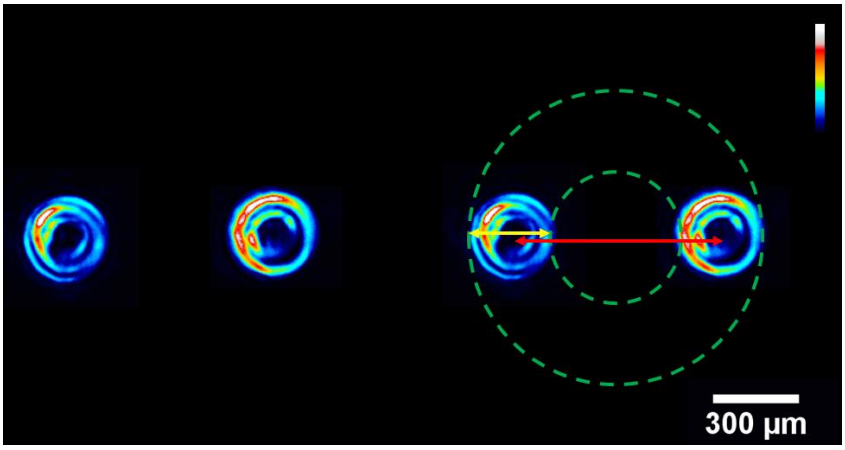

Figure 3.12 A CD beam from a single crystal, when passed through a second crystal undergoes double refraction before alignement. The dashed green lines show the inner and outer ring radii.

Figure 3.13 shows a comparison of the experimental and theoretical values for ring radii for the various cascades shown in Figure 3.8 with the values shown in table 3.2.

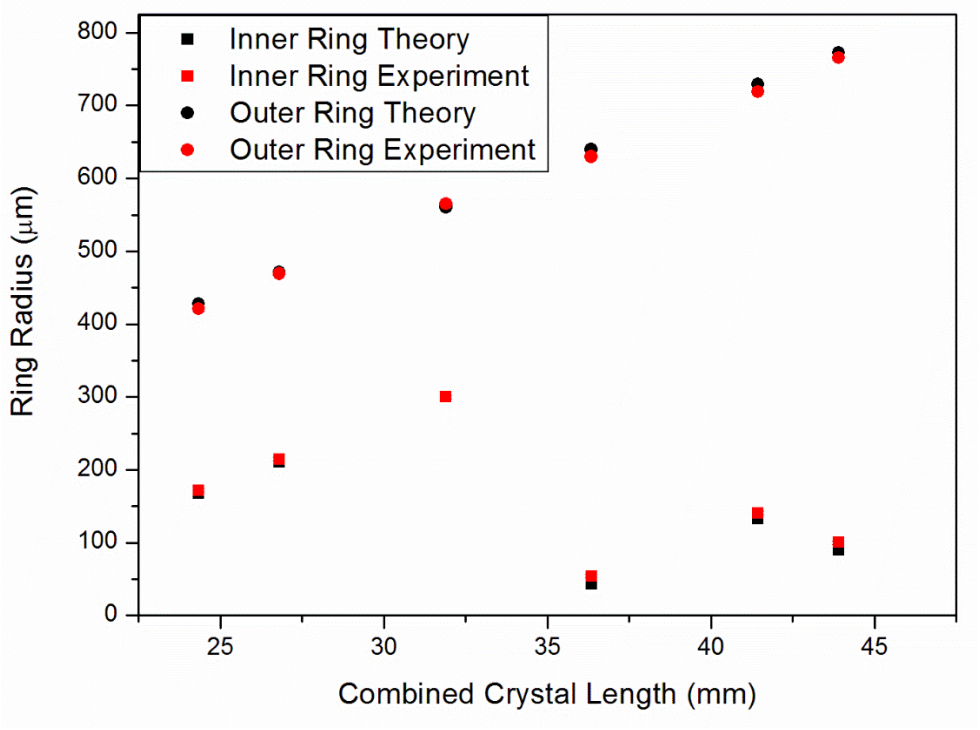

Figure 3.13 Comparison of theoretical (black) and experimental (red) values for inner ring radius (squares) and outer ring radius (circles) for all crystal combinations

	Inner Radius (μm)		Outer Radius (μm)	
Combined crystal length	Theory	Experiment	Theory	Experiment
24.34	167.7	172 ± 2.5	427.9	421 ± 2.5
26.80	211.0	215 ± 2.5	471.2	469 ± 2.5
31.90	300.6	300 ± 2.5	560.8	565 ± 2.5
36.34	43.2	54 ± 2.5	639.5	630 ± 2.5
41.44	133.0	141 ± 2.5	729.3	719 ± 2.5
43.90	89.8	101 ± 2.5	772.5	765.5 ± 2.5

Table 3.2 Theoretical and experimental values for inner and outer ring radius

3.3.4 Distance from ring plane to Raman spot, Z_F

The Z_f values for a cascade, like the Δ value, are the sum of the values for the individual crystals in the cascade. The comparison of values for a sample of the cascades used are shown in figure 3.14, with values in table 3.3.

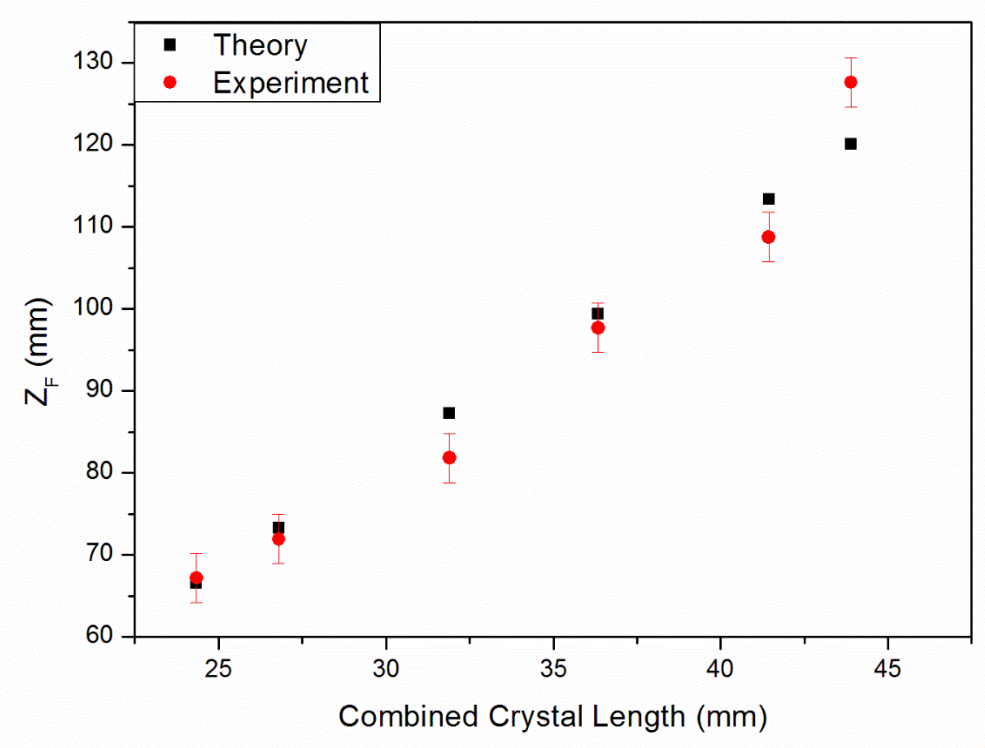

Figure 3.14 Comparison of theoretical (black squares) and experimental (red circles) values for Z_f for all crystal combinations

	2Zf (mm)	
Combined Crystal Length	Theory	Experiment
24.34	66.6	67.2 ± 3
26.80	73.3	71.9 ± 3
31.90	87.2	81.8 ± 3
36.34	99.4	97.7 ± 3
41.44	113.3	108.7 ± 3
43.90	120.1	127.6 ± 3

Table 3.3 Theoretical and experimental values for Z_f

3.3.5 Cross Section

The cross section of a two crystal cascade is shown in figure 3.15. Captured in the same manner as the single crystal cross section in chapter 2, this particular cascade consisted of crystals L1 and L3. The inner ring, formed by the two oppositely propagating cones, can be seen to be of higher intensity than the outer ring. All of the features described above can be seen in the image and are consistent with the single crystal analogue, indeed the central most intense section of this cross section is identical to that of a CD beam from a single CD crystal. Additional crystals would produce a more complex cross section with further intersecting sections outside the outer ring. The same MATLAB code (C1) used for the single crystal cross section was again used to produce this cross section.

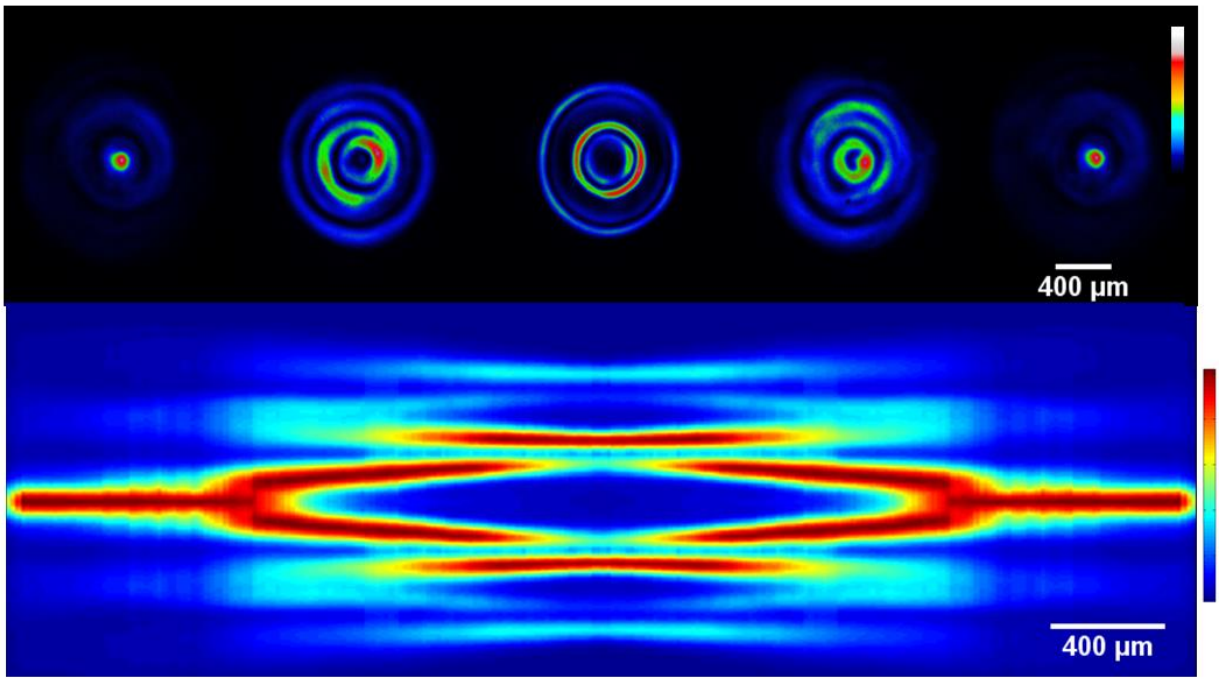

Figure 3.15 The cross section of the CD beam from a two crystal cascade consisting of crystals L1 and L3.

3.3.6 Comparison with theory

The theory of cascade CD was relatively recently advised with papers in 2010 [17] and 2013 [48] providing the bulk of information used here. A rigourous treatment is available in appendix 2. As stated earlier an N crystal cascade system will produce 2^{N-1} rings in the ring plane.

The geometric center of the ring pattern so produced can be found using:

$$\mathbf{r}_2 = \mathbf{r}_0 + \mathbf{G}_1 + \mathbf{G}_2 \tag{3.1}$$

where $\mathbf{r}_2$ is the center following a two crystal cascade, r_0 is the initial position of the incident beam and $\mathbf{G}$ is the lateral shift in the direction of the pseudovector for each crystal. The relative angles between the crystals is defined as:

$$\varphi_{21} = \varphi_2 - \varphi_1 \tag{3.2}$$

where φ_1 and φ_2 are the orientations of crystal 1 and 2 respectively. Using these parameters the intensity after the crystal for each ring, using incident CPL, can be found using:

$$\begin{aligned} \mathrm{I}_{2,\mathrm{CP}}^{(1)} &= \frac{\mathrm{I}_0}{4\pi \mathrm{w}_0 \mathrm{R}_2^{(1)}} \cos^2\left(\frac{\varphi_{21}}{2}\right) \\ \mathrm{I}_{2,\mathrm{CP}}^{(2)} &= \frac{\mathrm{I}_0}{4\pi \mathrm{w}_0 \mathrm{R}_2^{(2)}} \sin^2\left(\frac{\varphi_{21}}{2}\right) \end{aligned} \tag{3.3}$$

where I_0 is the incident intensity and $\mathrm{R}_2^{(1)}$ and $\mathrm{R}_2^{(2)}$ are the first and second ring radii found as the difference and the sum of the rings formed by the individual crystals respectively.

This was once again carried out using MATLAB script, an excerpt of which is included below. The code in its entirety is in appendix 4 (C4).

```
CR21=abs(abs(G2(2))-abs(G1(1)));
CR22=abs(abs(G1(1))+abs(G2(2)));
I21=(I0/(4*pi*w0*CR21))*(cos((phi21)/2))^2;
I22=(I0/(4*pi*w0*CR22))*(sin((phi21)/2))^2;
I21gauss=ygauss.*I21;
I22gauss=ygauss.*I22;
```

This method was used to obtain the images shown in figure 3.16. This is a good guide for the position and radius of the rings given certain crystal combinations in cascade, but lacks detail by not including any of the structure of the patterns (i.e. pair of rings with dark ring separating them.)

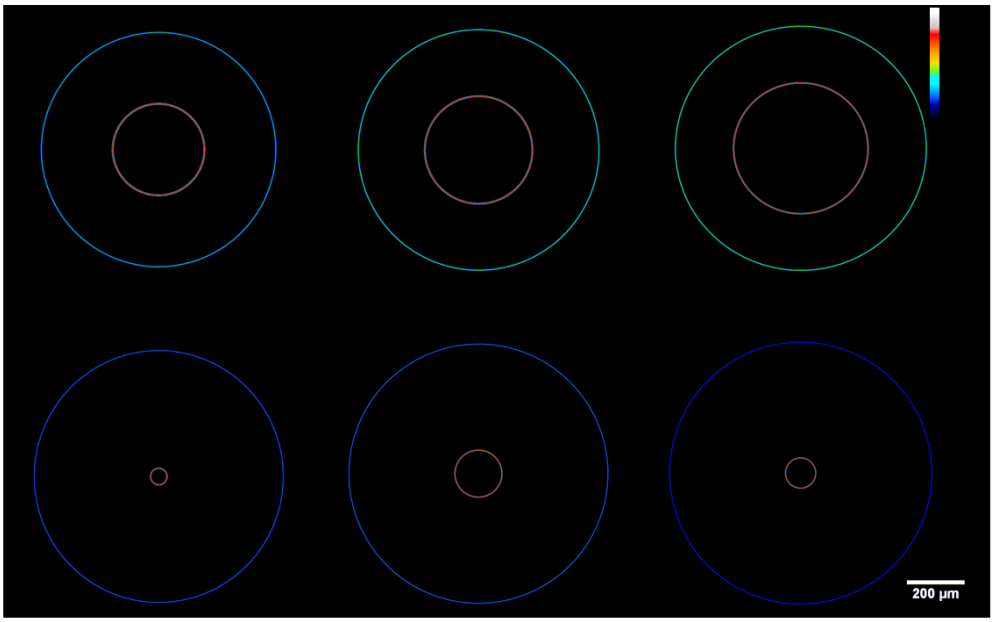

Figure 3.16 Cascade Ring plane patterns corresponding calculated using equation (3.3)

A relatively simple adjustment of combining this theoretical method with the method used in the previous chapter can give the detail of the single crystal case

for the cascade case as shown in figure 3.17. This involves substituting I_0 in (3.3) with the intensity values found from (2.6) in chapter 2.

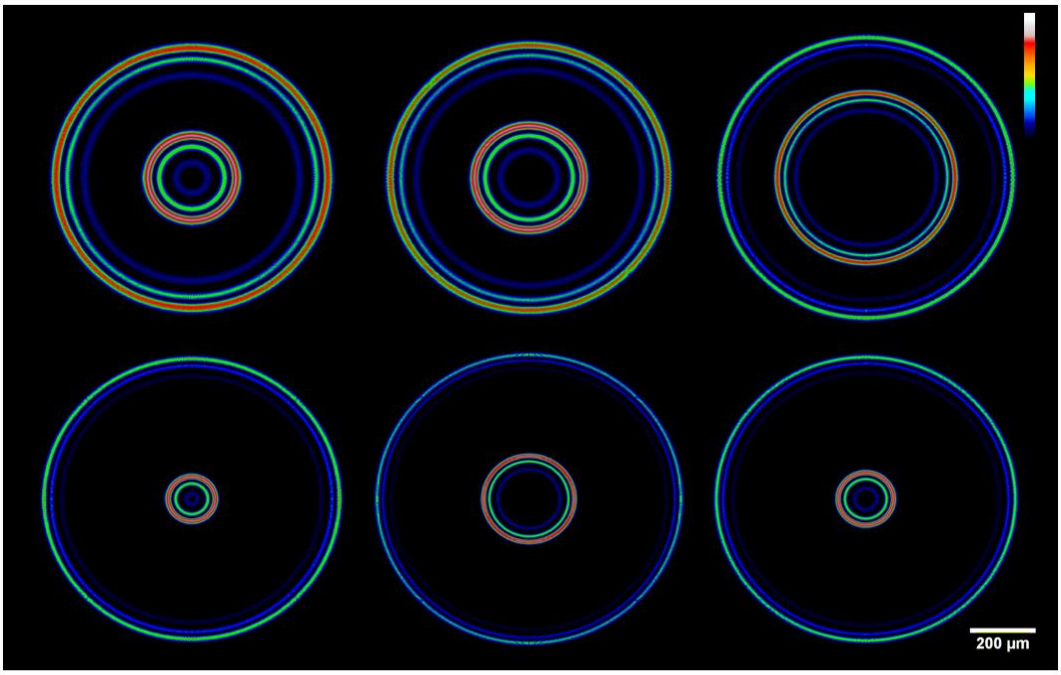

Figure 3.17 Theoretical images using a combination of equation (3.3) and the method outlined in chapter 2 using equation (2.6)

This is done by simply replacing the incident beam intensity in equation (3.3) with a vector containing the intensity profile found using the previously outlined method from chapter 2, where equation (2.6) gave the intensity profile of the CD ring. Again, the code in its entirety is available in appendix 4 (C5).

3.4 Discussion

The effects of the expansion from single crystal to cascade CD were investigated and found to be in line with the previous predictions of Berry [17]. The parameters of interest established in chapter 2 for the single crystal case were found to scale in the expected manner. The longitudinal shift, Δ, and the distance from the ring plane to the Raman spot, Z_f, were found to be the sum of the values for the individual crystals in the cascade. The ring radius however is slightly more complicated with rings formed based on a sum and difference relationship between the crystals in the cascade, as shown in figure 3.12, and in the values in table 3.2. It is worth noting that all the crystals used here are of different lengths. In the degenerate case where crystals of the same length are used, the inner 'ring' will simply be a reproduction of the incident beam, effectively a ring with radius zero. The cross section, collected in the same manner as before showed the same features as the single crystal case with additional structure outwith the central region.

An alternate experimental set up, as shown in figure 3.18, was used for 'variable' cascade experiments [49]. In this set up the order of the elements in the set up are rearranged with an imaging lens placed between the two crystals in the two crystal cascade.

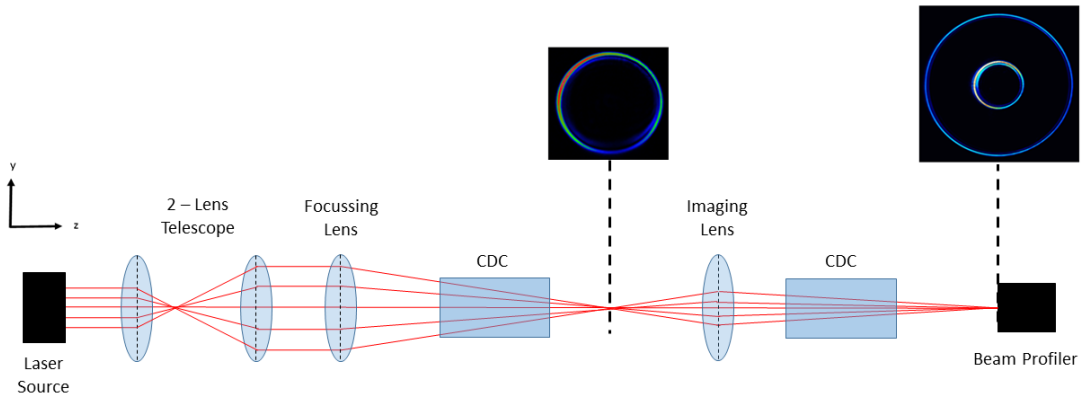

Figure 3.18 The alternative experimental set up for the 'variable' cascade set up with the additional imaging lens placed between the two crystals.

This type of experimental arrangement was first reported in 2015 [49] and allows for the production of almost any size of rings in the ring plane: i.e. not limited by the lengths of the available crystals as it is in typical cascade CD.

The ring plane images produced from a variable cascade are shown in figure 3.19. The images shown were all obtained using only two crystals (L4 and L2). The magnification of the system was changed using different focal length lenses to produce rings of different sizes, ordinarily only possible using different crystals as the properties of the ring produced depends only on the crystal length. The images show patterns produced using focal lengths of 100 mm (Newport KPX034), 50 mm(Newport KBX034), 25 mm (Newport KBX019), and 18 mm (Newport KPX358) resulting in magnifications M=1, 0.5, 0.25 and 0.18, for a-d respectively. The ring radii of the images are shown in table 3.4.

As the inner and outer ring radii are made up of the difference and sum of the ring radii produced by the individual crystals in the cascade respectively, solving simultaneous equations of $Radius\ 1 - Radius\ 2 = Inner\ Radius$ and $Radius\ 1 + Radius\ 2 = Outer\ Radius$ and using equation (2.4) (R=AL) the cascade needed to produce the observed patterns with the typical cascade setup can be found. This is also shown in table 3.4. As can be seen, the second crystal introduces a limitation on the system whereby all ring radii values are formed as if only the first crystal in the variable cascade was changed.

Figure 3.19 Images produced from the variable cascade (crystals L4 and L2) with different magnifications, (a) M = 1, (b) M = 0.5, (c) M= 0.25, and (d) M = 0.18.

			Equivalent Cascade	
Magnification	Inner Ring Radius (µm)	Outer Ring Radius (µm)	First Crystal Length	Second Crystal Length
1	150 ± 2.5	682 ± 2.5	23.6 mm	15.1 mm
0.5	252 ± 2.5	779 ± 2.5	29.3 mm	15 mm
0.25	506 ± 2.5	1039 ± 2.5	43.9 mm	15 mm
0.18	620 ± 2.5	1132 ± 2.5	49.77 mm	14.5 mm

Table 3.4 Radii values for different magnifications in the variable cascade. The crystal lengths normally needed to produce these ring radii are shown in the right hand columns.

The results shown are the first steps in expanding from the simplest single crystal experiments to the more complex and interesting aspects of the phenomenon that are explored later on in this work. Indeed cascade CD is a relatively new field and as such is one of the areas to emerge from the renewed interest in the phenomenon in the last two decades. The simplified theoretical aspects in this chapter are once again practical in nature allowing for quick and easy ring plane patterns to be simulated aiding in experimental design and the search for applications.

Having now achieved a grasp of the fundamentals of CD experiments, we turn our attention to perhaps its most interesting sub-theme, its unique polarisation properties.

3.5 Summary

In this chapter the expansion from single to multi crystal experiments was investigated. The addition of more crystals was seen to increase the number of rings seen in the ring plane such that for an N crystal cascade there are 2^{N-1} concentric rings. The parameters measured (longitudinal shift, ring radius, and distance from Raman spot to ring plane) were all found to be increased from the single crystal case, with the increases showing that the values for a cascade are the sum of the individual crystals used in the cascade. All the measurements were consistent with the Berry theory [17]. The recently described variable cascade offers a useful alternative setup to overcome the limitations on possible ring radii influences caused by the crystal dimensions.

4 Polarisation effects in conical diffraction

Apart from the crystals themselves, perhaps the biggest factor determining the appearance of the ring pattern in the ring plane is the polarisation of the incident beam. The polarisation state of a conical diffraction (CD) beam is one of its most unique and interesting features. In this chapter a number of different incident polarisations are used to determine the effects on the patterns produced both in and away from the ring plane.

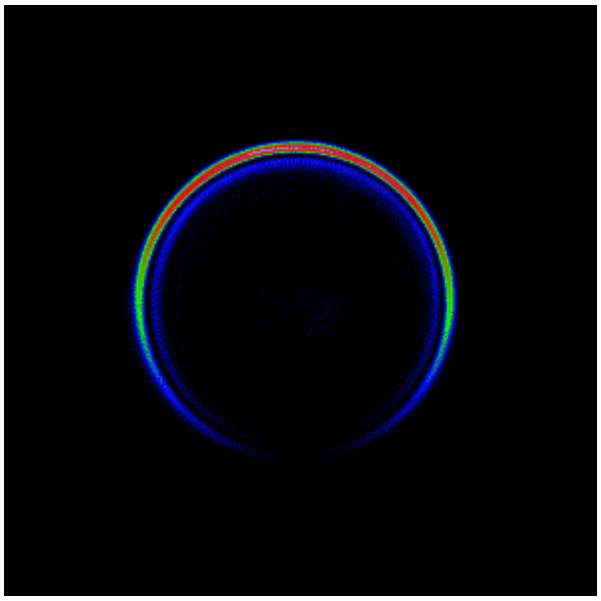

Figure 4.1 Effect of linear polarisation on a CD ring pattern.

4.1 Introduction

In this chapter one of the more interesting aspects of conical CD is explored. The polarisation state of a CD beam is such that any two diametrically opposite points are orthogonally polarised, as shown in figure 4.2 The use of different incident polarisations has various effects on the patterns observed in the ring plane of the system. The polarisations examined in this chapter are: unpolarised light (UPL); circularly polarised light (CPL); linearly polarised light (LPL); and azimuthally (APL) and radially polarised light (RPL).

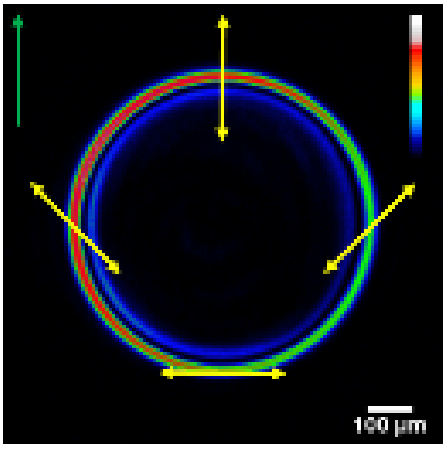

Figure 4.2 Polarisation state of a CD ring using CPL/UPL. The green arrow indicated the crystal's **G** *vector orientation*

In order to observe the effect of these various polarisations, a number of different experimental arrangements were needed.

The experimental arrangement and resultant ring plane images from chapter 2 are illustrative of the UPL case.

In order to achieve CPL, the system shown in figure 4.3 was used. The LPL beam from a 633 nm helium-neon laser (Newport R-30602), having earlier been collimated (2 – lens telescope consisting of a 100 mm Newport KBX064 lens and a

200 mm Newport KPX106 lens), was incident on a quarter wave plate (AQWP05M-600 from Thorlabs) placed before the system's focussing lens (100 mm Newport KPX034 lens). This quarter wave plate was used to produce CPL. Right handed circularly polarised light (RCPL) was produced by placing the fast axis of the wave plate at 45^{o} to the plane of incident polarisation and left handed circularly polarised light (LCPL) was produced by rotating the wave plate through 90^{o}.

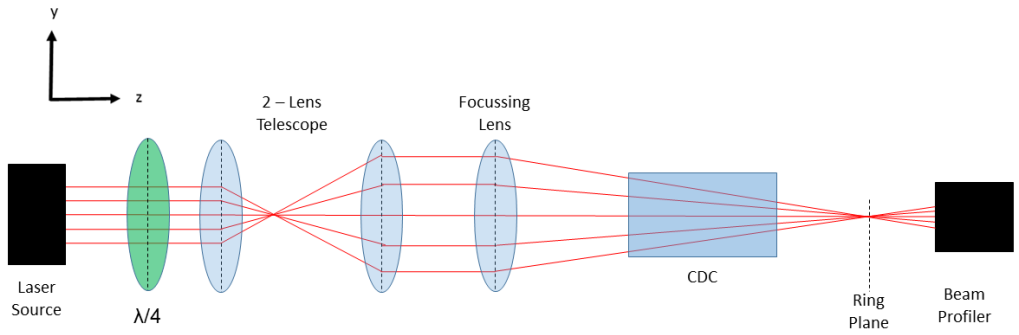

Figure 4.3 Optical arrangement used to produce CPL and CD. The addition of a quarter wave plate with it's fast axis at 45º or 135º to the incident beam polarisation was used to produce RCPL and LCPL respectively

CPL is expected to produce ring plane patterns in the same way as UPL as the rotation of polarisation in the case of CPL results in intensity being present at all areas of the CD beam. Indeed UPL, LCPL and RCPL incident beams produce the same results in the ring plane for single and cascade set ups. However, as predicted in [17], the effect of L/RCPL on the patterns produced away from the ring plane by a three crystal cascade differs for the two polarisations.

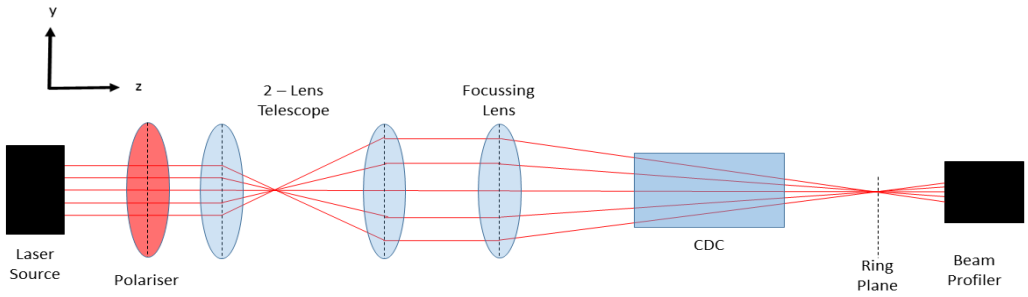

Figure 4.4 A linear polariser allows for rotation of the plane of polarisation of the incident beam.

Due to the polarisation state of the CD beam, the absence of any particular polarisation direction will result in a section of the ring corresponding to that polarisation being missing. That is the case for LPL. When an LPL beam is used, the section of the ring with orthogonal polarisation to the plane of the incident beam's polarisation is missing, resulting in a crescent shaped beam. The optical arrangement used to show this is illustrated in figure 4.4 and consists of the typical arrangement as seen in figure 2.7 with the addition of a polariser (LPVISB050-MP2 from Thorlabs) to polarise the beam and facilitate the rotation of the incident beam's polarisation.

The most unusual types of polarisation used in these experiments were APL and RPL. As shown in figure 4.5, these are annular beams with polarisation such that a

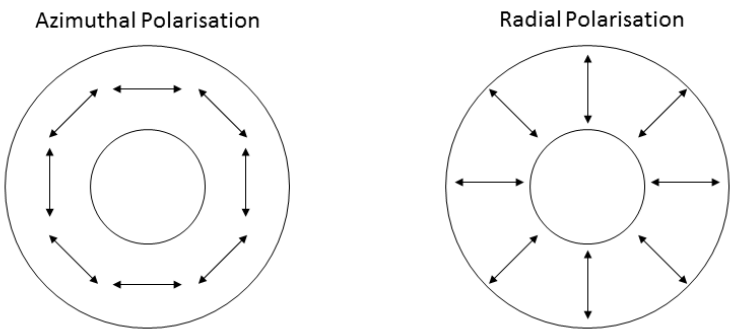

Figure 4.5 Schematic diagrams of APL and RPL

line drawn radially out from their center will be perpendicular (in the case of APL) or parallel (RPL) to the plane of polarisation of the beam at the point where it crosses the annulus [52].Experiments involving RPL and CD have been carried out before [53] but they involved the production of RPL beams from incident Gaussian beams utilising the CD phenomenon and not the use of an incident RPL beam to produce CD.

The experimental arrangement used to produce these polarisations is shown in figure 4.6. An S-waveplate converter is used to produce the polarisations using different linearly polarised input beams, controlled by a half wave plate (AHWP05M-600 from Thorlabs). The S-waveplate is a nano-structured waveplate which converts LPL to RPL or APL. It is available commercially from UAB Altechna, Lithuania [54], and its functionality is based on a technique developed by the Optoelectronics Research Centre at Southampton University [52]. Vertically polarised input produces APL from the S-waveplate, while horizontally polarised input produces RPL.

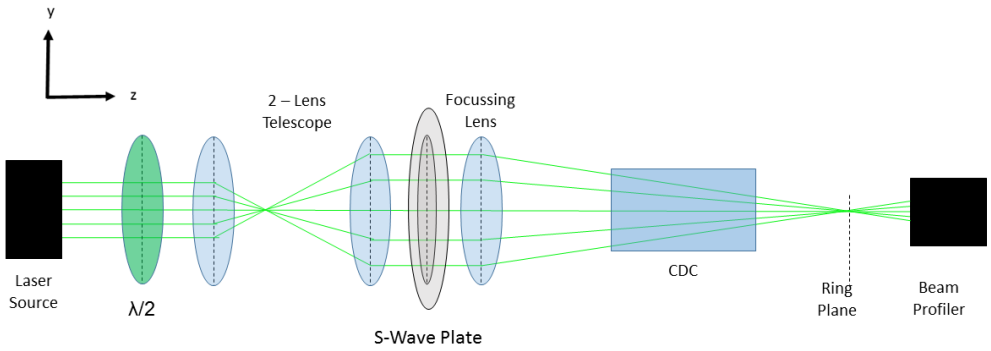

Figure 4.6 Experimental arrangement to produce APL, RPL and CD. The half wave plate controls the linear polarisation of the incident beam and the S-wave plate produces the APL and RPL. A 150 mm focal length lens (KPX064 form Newport) was used.

Figure 4.7 shows the beam profiles after the S-waveplate. A vertically polarised incident beam is shown on top for illustrative purposes, the left hand side of the second row shows the APL beam and the third row shows the RPL beam. The polarisations were verified using a polarising beam splitter. The reflected beams are shown on the right hand side of the second and third row. Either a vertical or horizontal pair of lobes was observed corresponding to APL and RPL respectively.

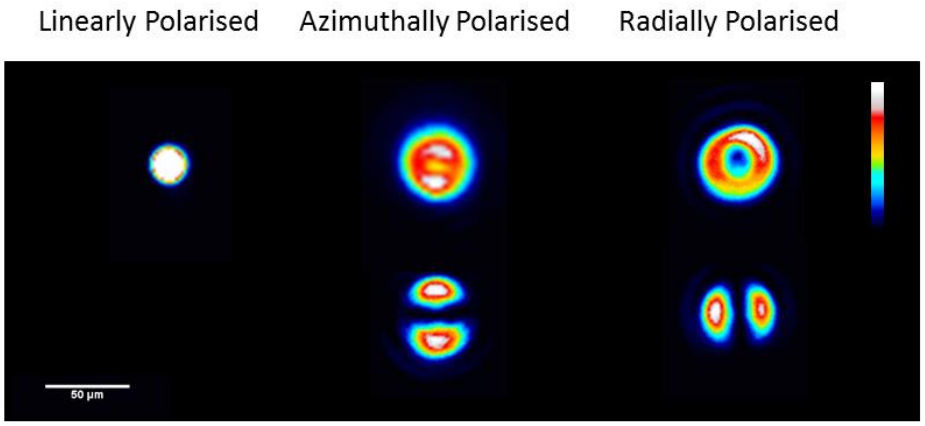

Figure 4.7 Beam profiles for LPL, APL, and RPL. The bottom row is the same profile having passed through a polarising beam splitter.

4.2 Results

4.2.1 Circularly Polarised Light

As previously mentioned, CPL is expected to produce a full ring in the same way as the images using UPL from chapter 2. As seen in figure 4.8, that is indeed the case: the images are identical to those seen for UPL and there is no discernible difference in the ring plane between RCPL (figure 4.8 (a)) and LCPL (b).

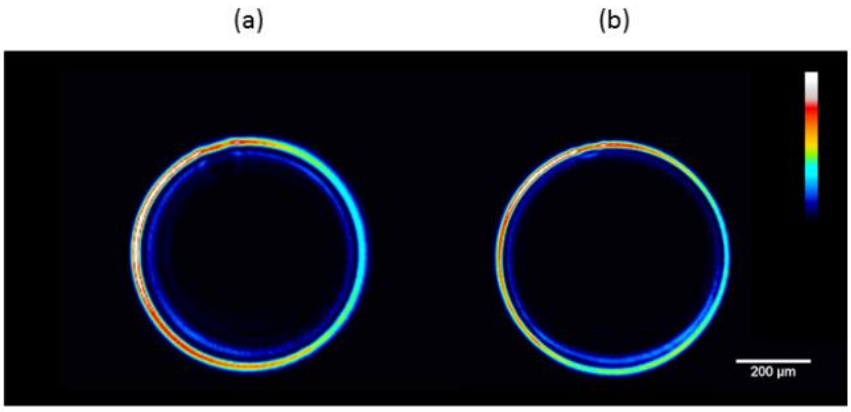

Figure 4.8 Comparison of ring plne images using (a) RCPL and (b) LCPL with crystal L3 (19.4 mm)

In order to test if the predicted variations arising from the incident light's handedness do actually occur, the system shown in figure 4.3 that employs a three crystal cascade (similar to the cascade the cascade shown in figure 3.5) was used. However, as per Berry's prediction, the angle of each crystal's **G** vector relative to the preceding crystal was 45^{o}, not 90^{o}, as in the cascades in chapter 2. The cascade was used to record images away from the ring plane at three propagation distances (in the z direction on figure 4.3), measured in units of Rayleigh range, the distance from the narrowest point of the beam waist to where the waist cross section is doubled. This value is given the notation of ζ as mentioned in equation (2.3). Values

of ζ = 2.75, 3.00, and 3.25 were used, corresponding to values of 48.2 mm, 49.8 mm and 51.3 mm respectively.

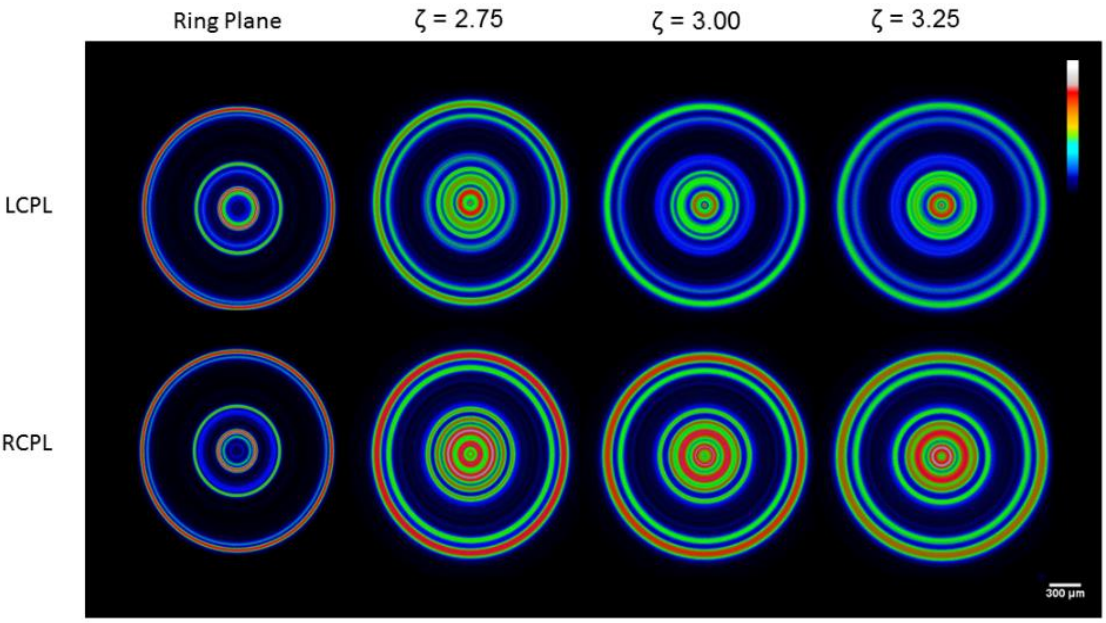

Figure 4.9 Ring patterns for a three crystal cascade using LCPL and RCPL for the ring plane and three additional propagation distances.

The ring plane patterns at these propagation distances are shown in figure 4.9. These images were radially averaged to highlight the features and allow for extraction of the intensity profiles shown in figures 4.10 and 4.11. The ring plane images, as expected, are identical for both LCPL and RCPL. Moving further from the ring plane some distinguishing features emerge. The positions of the concentric rings is the same in all cases but variations exist in the fine structure of the patterns and the overall intensity is different with RCPL having higher intensity than LCPL. Some of the variations in structure are better illustrated in figure 4.11 on the intensity profile graphs, with a single peak at 500 µm for RCPL being replaced by two close peaks in the same position for LCPL in the ζ = 3.00 and 3.25 case. The

main difference between the two is the appearance of a bright central spot in the case of LCPL, which is absent for RCPL.

The differences are thought to arise due to the complex nature of the Belskii-Khapalyuk equations away from the ring plane and that the transformation matrix for the cascade as a whole is made up of the product of the matrices for each individual crystal, which are non-commutative. The central spot is similar to the degenerate case where path cancellations lead to a zero radius ring and the central spot is in fact a reproduction of the incident Gaussian beam as described in the discussion section of chapter 3.

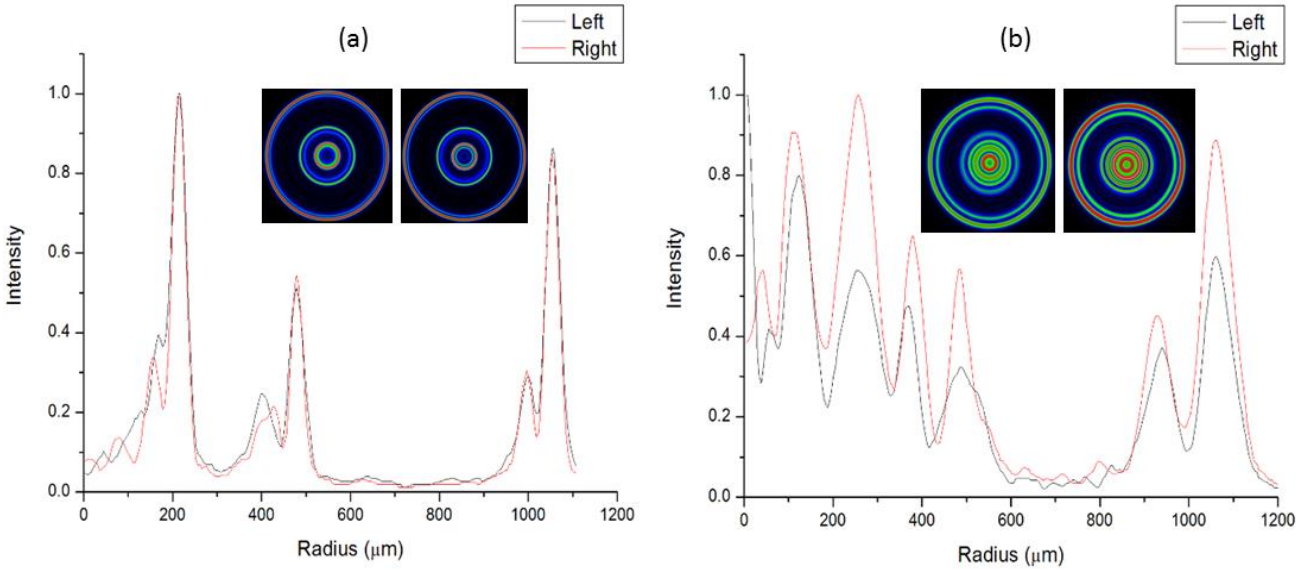

Figure 4.10 Intensity profiles for (a) ring plane and (b) ζ = 2.75. The ring plane patterns are effectively indistinguishable for both LCPL (black line) and RCPL (red line). For the ζ = 2.75 case the differences in intensity and the central spot are evident.

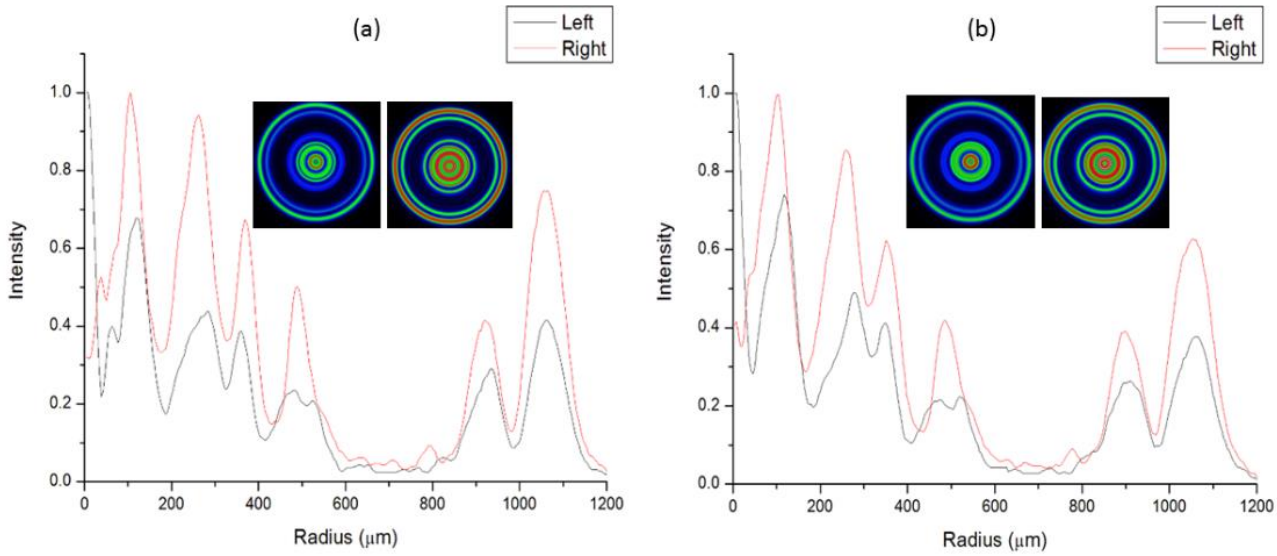

Figure 4.11 Intensity profiles for (a) ζ = 3.00 and (b) ζ = 3.25. Again the intensity is different between LCPL and RCPL and the central spot is present for LCPL only. Additional fine structure differences are also visible, around 500 μm for example.

4.2.2 Linearly Polarised Light

As shown in figure 4.2 the polarisation of a CD beam is such that any two diametrically opposite points on the ring are orthogonally polarised. As such the use of LPL will result in the section of the ring orthogonally polarised to the plane of polarisation of the incident beam being missing, resulting in a crescent shaped beam. Figure 4.12 (overleaf) shows a complete CD ring pattern overlain with arrows showing its polarisation. The surrounding images show the resulting patterns when LPL is used and the plane of the incident beam's polarisation is rotated through 180^{o}. The top image corresponds to vertically polarised incident light, resulting in the bottom section of the ring being missing. The bottom image is horizontally polarised light resulting in the top section of the ring being missing. The other images are intermediate points in steps of 30^{o}.

On the following page corresponding theoretical images are shown in the same layout in figure 4.13. For LPL, the intensity value found for CPL is in essence modulated along the circumference of the ring to produce the variation observed as the orthogonally polarised section of the ring pattern falls to 0. To do this the CPL intensity found in chapter 2 is adjusted by a term taking the angular position on the ring into account:

$$\mathrm{I_{LP}} = \mathrm{I_{CP}}\frac{2}{\pi}\cos^2\left(\frac{\chi + \varphi_1}{2} - \Phi_0\right) \qquad (4.1)$$

where Φ_0 is the polarization azimuth of the incident beam and χ is the angular position on the ring. Using equations (2.6) and (4.1) a theoretical ring pattern (Figure 4.13) can be found for LPL using MATLAB (Appendix 4 (C6)).

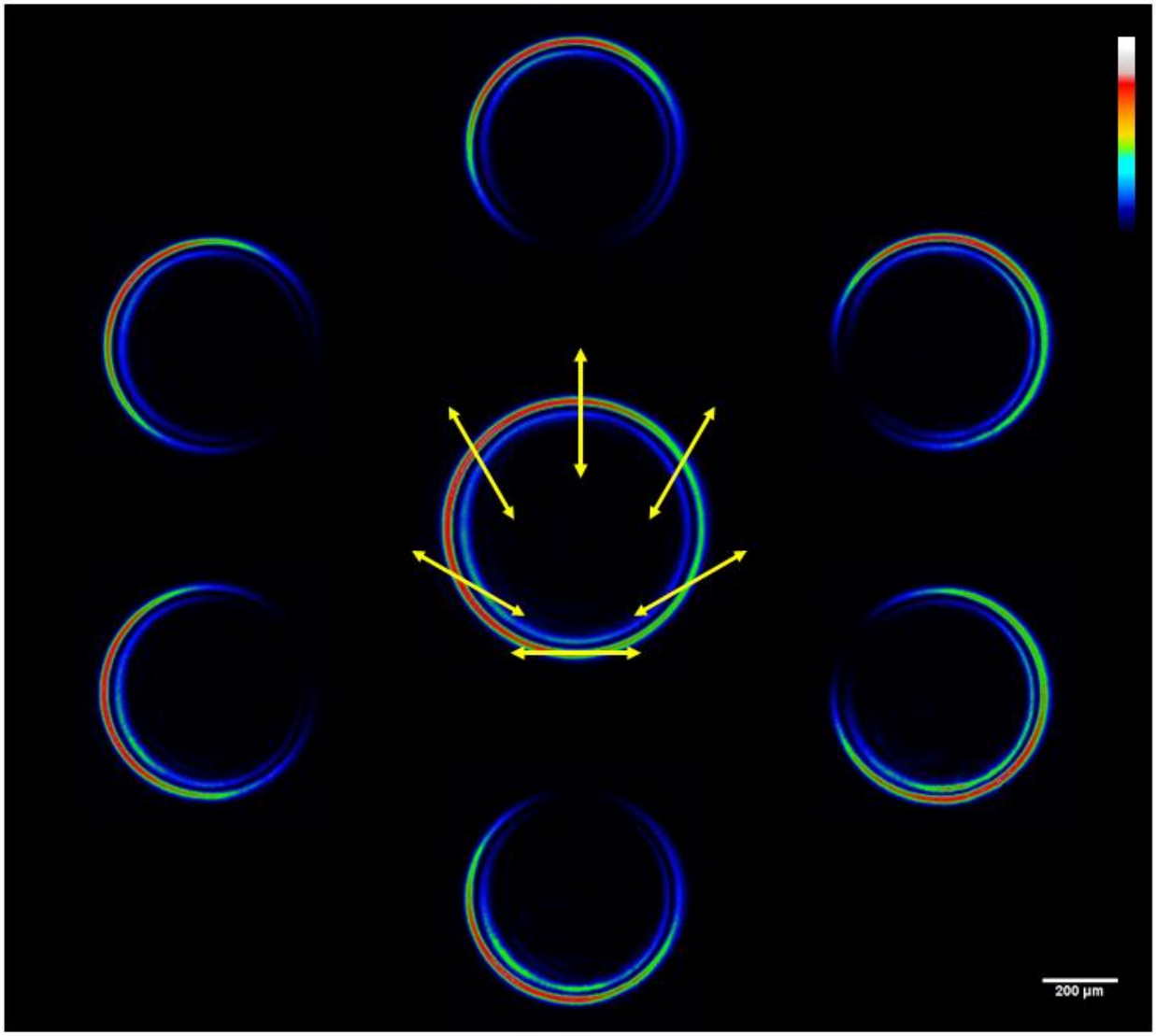

Figure 4.12 Experimental images of a CD beam with UPL/CPL incident beam. The yellow arrows indicate polarisation at that point on the ring. The surrounding images are of the ring pattern using LPL

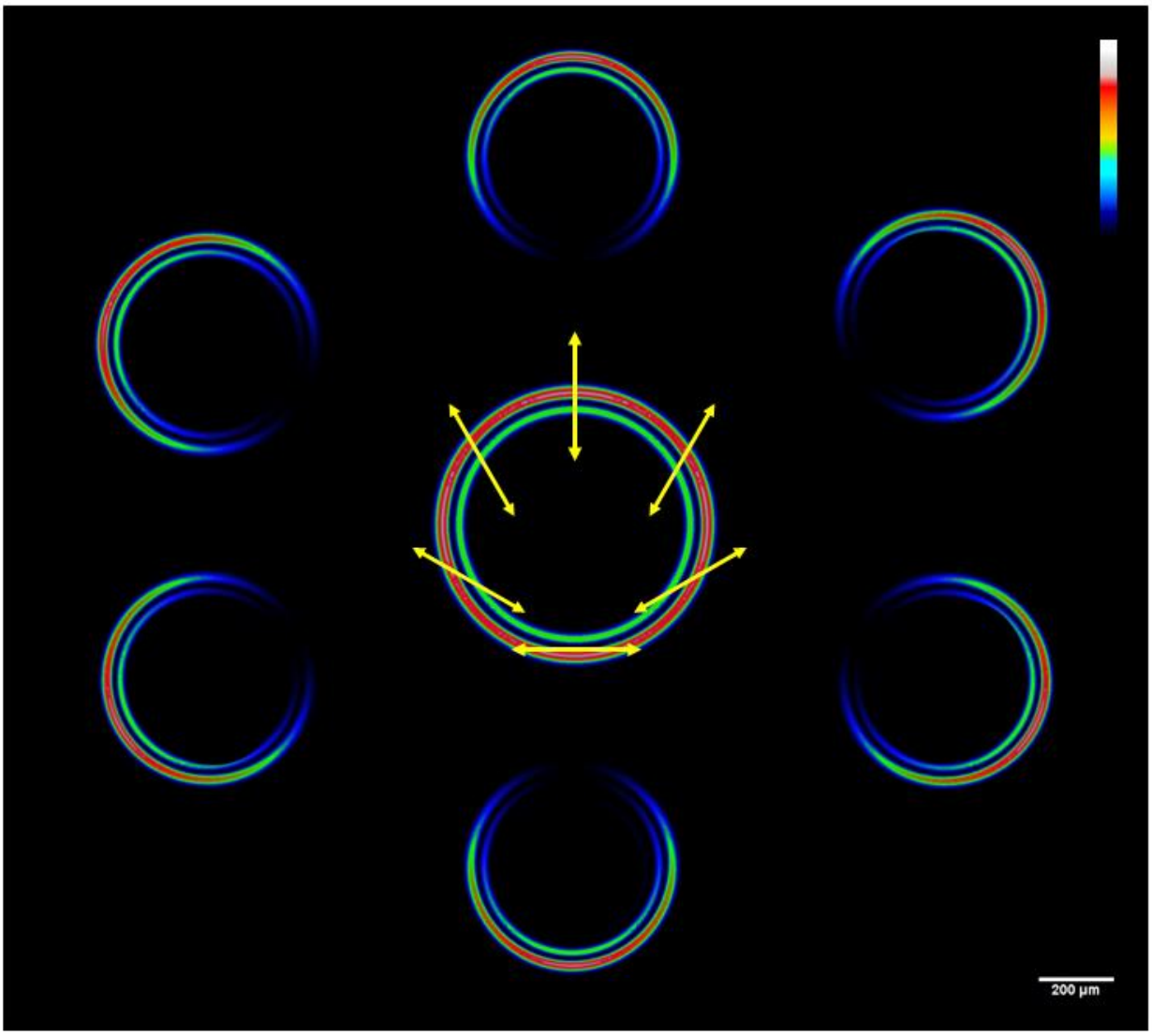

Figure 4.13 Theoretical images corresponding to the experimental images in figure 4.12

```
for j=1:401
    for i=1:2881
      ILP(i,j)=Irings(min(ind)+j)*(2/pi)*(cos((chi(i)+phi)-
      (((chi(i)+phi)/2))))^2;
    end
end
```

This code excerpt creates a running variable filled with intensity values along the circumference of the ring, which is used to make the ring patterns in figure 4.13

This method can then be expanded upon to provide theoretical intensity patterns for two, three, and four crystal cascades by following the same method as that in chapter 3 and introducing the modulation described above.

For a two crystal cascade equation (4.1) becomes:

$$\begin{aligned} I_{2,LP}^{(1)} &= I_{2,CP}^{(1)} \frac{2}{\pi} \cos^2\left(\frac{\chi + \varphi_1}{2} - \Phi_0\right) \\ I_{2,LP}^{(2)} &= I_{2,CP}^{(2)} \frac{2}{\pi} \cos^2\left(\frac{\chi + \varphi_1}{2} - \Phi_0 + \frac{\pi}{2}\right) \end{aligned} \tag{4.2}$$

where the superscript indicates the order of the rings in the ring pattern counting out from the center. This is implemented by slightly modifying the previous code to add the additional ring:

```
for j=1:401

for i=1:2881


      ILP(i,j)=Irings(min(ind)+j)*(2/pi)*(cos((chi(i)+phi)-
      (((chi(i)+phi)/2))))^2;
      ILP2(i,j)=Irings(min(ind)+j)*(2/pi)*(cos((chi(i)+phi2)-
      (((chi(i)+phi2)/2))))^2;


end
end
```

Utilising the same filtering argument as outlined in chapter 3, the effect of polarisation on cascade CD can be illustrated by rotating the filter about the ring of the first CD pattern and observing the effects on the pattern produced after the second crystal.

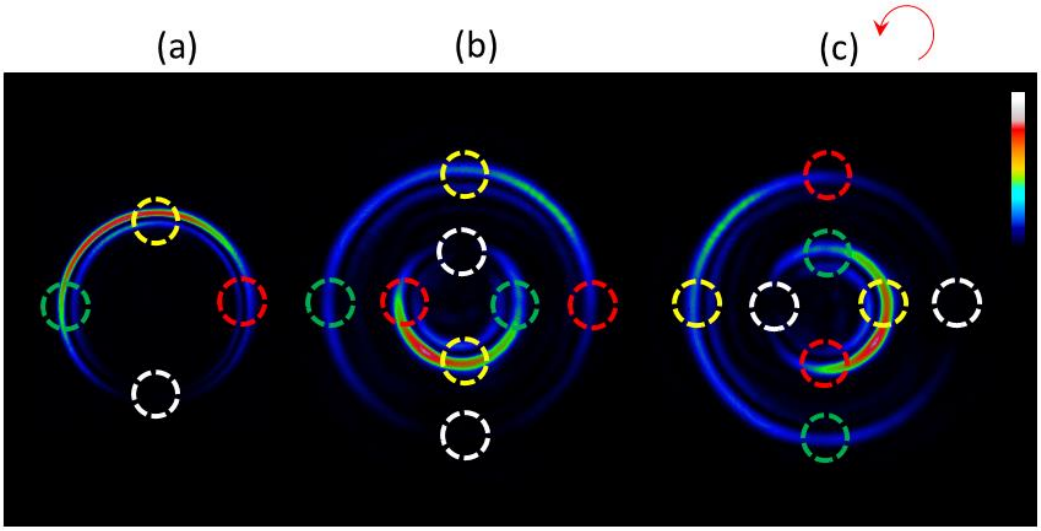

Figure 4.14 Ring patterns for (a) single crystal CD, (b) two crystal cascade, and (c) two crystal cascade with rotation (indicted by the red arrow) introduced by the second crystal's **G** *vector orientation. The coloured circles show the points on the single crystal CD ring which contribute to the corresponding points on the two crystal ring pattern.*

When one area of the single crystal pattern is missing due to the effect of linear incident polarisation, this effect is carried through to the cascade pattern. In the case of figure 4.14, the section of the ring highlighted in white is missing in the single crystal CD ring and subsequently missing from the two crystal cascade image.

The overall pattern produced by the entire cascade will be rotated according to the orientation of the crystals that make up the cascade. So, for example, the figure shows (a) the ring plane pattern after the first crystal, (b) after the second crystal without rotation, and (c) finally after the second crystal with the rotation introduced by the second crystals orientation (indicated by the red arrow). The rotation is always observed; (b) is for illustrative purposes only.

Figure 4.15 shows a comparison of the patterns for (a) a two crystal cascade consisting of L1 and L3, and (b) a three crystal cascade consisting of L1, L3, and L2. In this case horizontally polarised light is used. The top row shows experimentally registered images using a combination of the arrangement shown in figure 3.5 and the linear polarisation set up shown in figure 4.4. The bottom row shows theoretical images using a combination of the theoretical method for cascade systems shown in chapter 3 (figure 3.17) and the intensity modulation discussed earlier in this chapter.

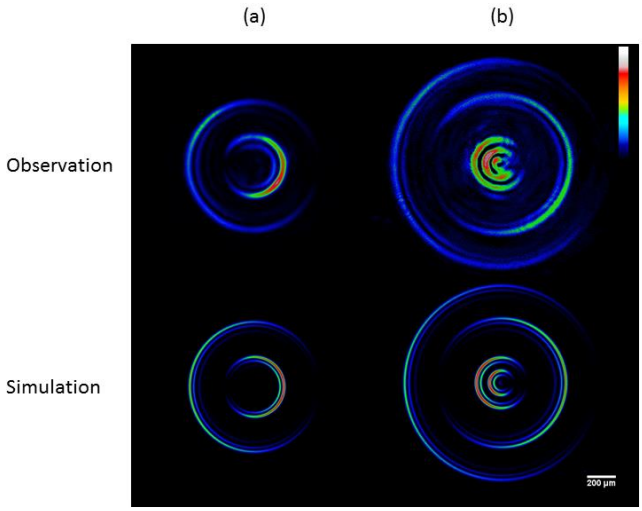

Figure 4.15 Ring plane patterns for two and three crystal cascade using horizontally polarised incident light. The top row shows experimental images and the bottom row shows theoretical images.

4.2.3 Azimuthally and Radially Polarised Light

The use of the annular beams with azimuthal and radial polarisation, as shown in figure 4.5, produces a more unusual effect than those present when using more conventional types of polarisation. Using the system shown in figure 4.6 the annular beam propagates along the crystal and emerges not as a single ring, but as two closely spaced concentric rings of equal intensity. Figure 4.16 shows a comparison between the LPL, APL, and RPL cases at 5 different points along the beams propagation. The LPL case shows the previously reported Raman spots, Poggendorff splitting and ring pattern consisting of the Hamilton-Lloyd ring, with the inner ring having significantly less intensity than the outer ring. This intensity is redistributed in the case of APL and RPL giving the two effectively equal rings seen in rows 2 and 3 of figure 4.16. The missing section of the ring changes due to the method by which the annular beams are produced with APL being created using vertical polarisation and RPL created using horizontal polarisation. The separation between

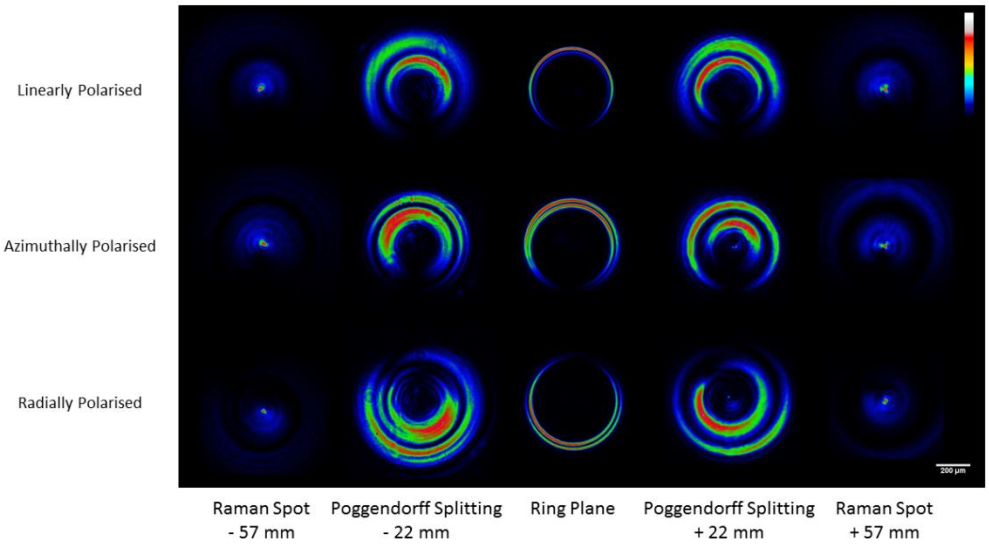

Figure 4.16 Comparison of vertical LPL (top row), APL (middle row), and RPL (bottom row) ring patterns along with front and back Raman spots and Poggendorff splitting.

the rings was found to be ≈ 25 μm, the radii of the annular beams in the focus of the system.

Figure 4.17 shows the intensity profiles for the three cases shown in figure 4.16. The intensity redistribution can be seen when comparing the high and low intensity ring pair of LPL (green dashed line) to the equal intensities of both the APL (red dashed line) and RPL (solid black line) ring pairs.

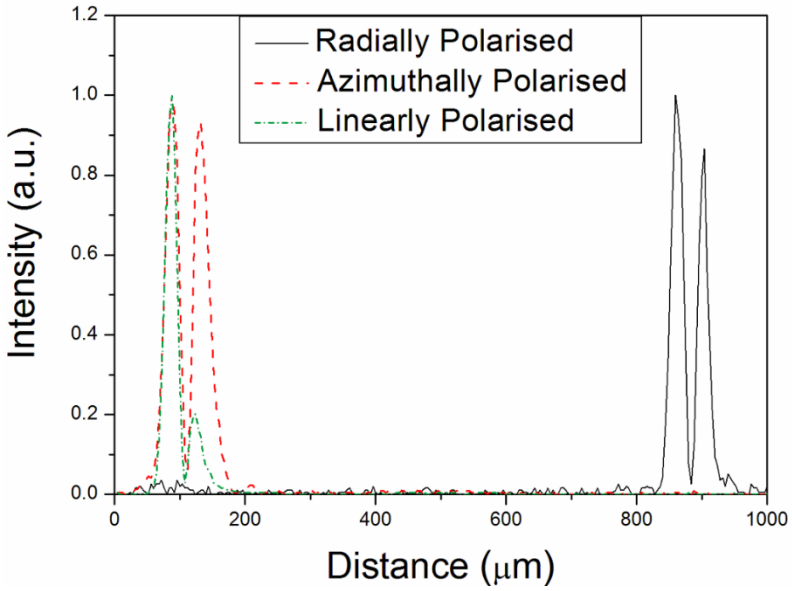

Figure 4.17 Intensity profiles for RPL (black line), APL (dashed red line), and LPL (dashed green line).

The polarisation state of the rings was examined using a polariser in a number of positions. Figure 4.18 shows the ring plane pattern without the polariser in place (first column) and with the polariser in four positions (vertical, horizontal, 45^{o}, and 135^{o}). Using the polariser shows different sections of the ring to be comprised of different combinations of horizontal and vertical polarisations between the top and bottom points of pure vertical and horizontal polarisation respectively. This follows in the same manner as the LPL case. There is in fact no variation in the ring plane polarisation between the linear case and the two other cases presented. The

polarisation states of the APL and RPL patterns correspond to the linear cases of vertical and horizontal polarisation respectively.

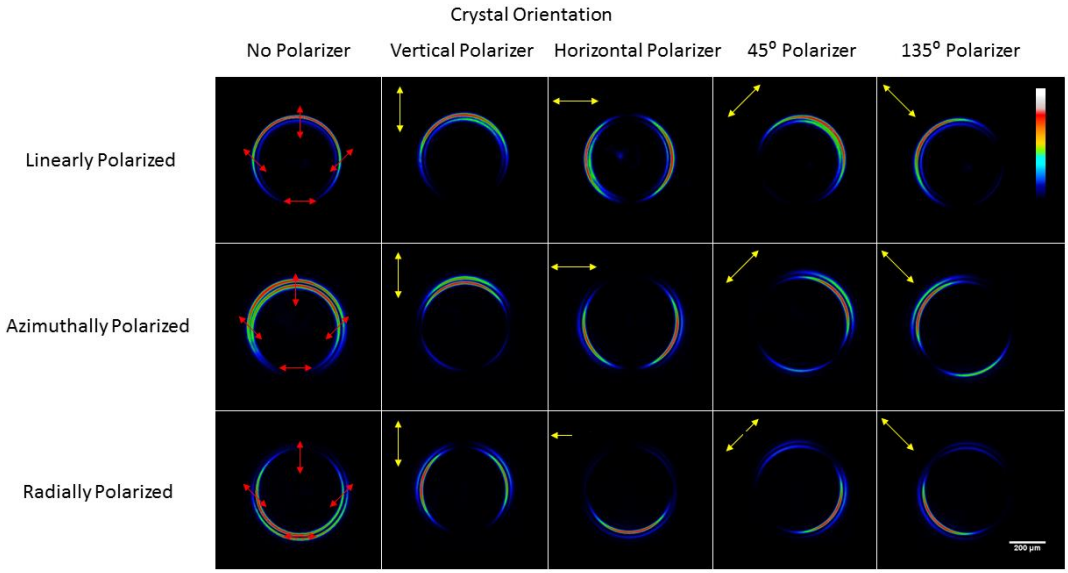

Figure 4.18 Polarisation state in the ring plane for LPL (top row), APL (middle row), and RPL (bottom row) polarisation. Four polariser positions were used, vertical, horizontal, 45°, and 135° (column 2 – 5 respectively.)

Alignment in this case is critical and slight misalignment can result in erroneous, but visually striking, patterns, such as those shown in Figure 4.19.

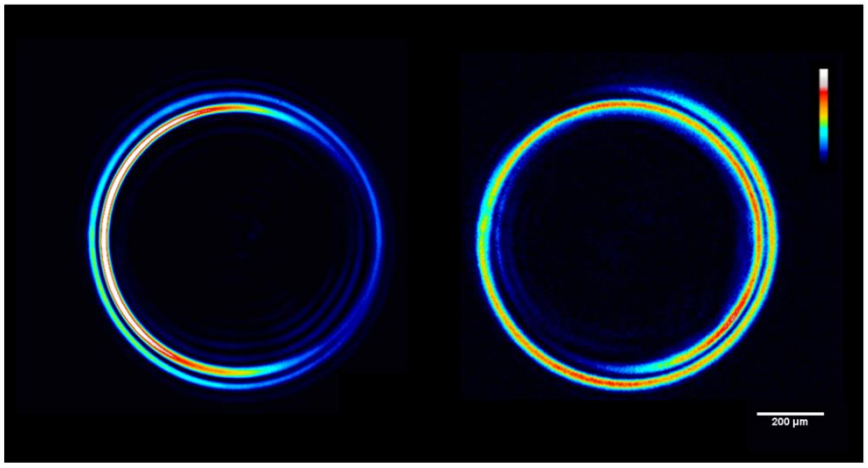

Figure 4.19 Slight misalignment for APL (left) and RPL (right)

The left hand image is a misaligned case of APL and appears to show a redistribution of intensity, not making both the inner and outer rings equal, but making the inner ring more intense than the outer ring. The right hand image shows an analogous situation for RPL and produces a spiral pattern in the ring plane. Both are interesting results but appear to arise only in the case of misalignment.

The beam generated by the S-plate is an annular beam with radius r_0. When this beam passes through the crystal it is split into two rings $R_+ = r_0 + R_0$ and $R_- = |r_0 - R_0|$ where R_0 is the radius of the CD ring from the crystal.

The intensity distribution of the annular beam after it has been conically diffracted depends on the polarization state of the incident annular beam as well as the sign of R_-. In the case described here $R_- < 0$ so the intensity distribution of both rings is the same and given by:

$$I(\varphi) = \cos^2\left(\frac{\chi(\varphi)}{2}\right) \tag{4.3}$$

where φ is the polar angle of the points about the ring. The function $\chi(\varphi)$ is given by $\chi(\varphi) = 2\varepsilon(\varphi) - \varphi$ where $\varepsilon(\varphi)$ is the angle of polarisation of the incident beam at the point with polar angle φ on the CD beam. In other words the polarisation of the incident beam at the corresponding location on the CD ring.

This differs for RPL and APL incident beams. For the RPL beam $\varepsilon(\varphi) = \varphi$, giving $\chi(\varphi) = \varphi$. Therefore equation (4.3) gives $\cos^2(\varphi/2)$.

For the APL beam $\varepsilon(\varphi) = \varphi + \pi/2$. This gives $\chi(\varphi) = \varphi - \pi$ and equation (4.3) will give $\sin^2(\varphi/2)$.

Using equation (4.3) to determine the intensity, and knowing the incident polarisation ε(ϕ), the theoretical images shown in figure 4.20 were obtained, once again, using a MATLAB script. An excerpt is shown here with the whole code available in appendix 4 (C6).

```
for i=1:2881

    Erad(i)=phi(i);                         %Radial Epsilon value from
                                             theory
    EAz(i)=phi(i)-pi;                       %Azimuthal Epsilon value
                                             from theory
    chirad(i)=(2*Erad(i))-phi(i);           %Radial Chi value from
                                             theory
    chiAz(i)=(2*EAz(i))-phi(i);             %Azimuthal Chi value from
                                             theory
    Irad(i)=(cos((phi(i)-phig)/2))^2;       %Radial Intensity
    Iaz(i)=(sin((phi(i)-phig)/2))^2;        %Azimuthal Intensity

    %Same as above but for the Inner Ring
    Erad2(i)=phi(i);
    EAz2(i)=phi(i)-pi;
    chirad2(i)=(2*Erad2(i))-phi(i);
    chiAz2(i)=(2*EAz2(i))-phi(i);
    Irad2(i)=(cos((phi(i)-phig)/2))^2;
    Iaz2(i)=(sin((phi(i)-phig)/2))^2;

end
```

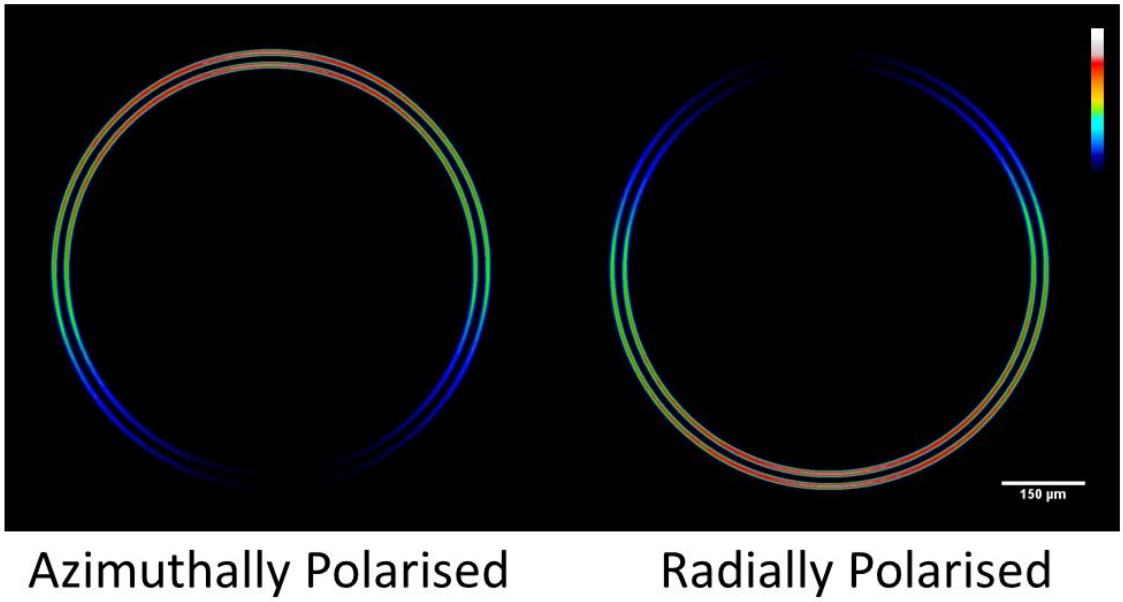

Figure 4.20 Theoretical ring patterns for APL and RPL incident beams. The intensity in this case is almost equal in both the inner and outer rings, differing from a typical CD pattern which has a higher intensity outer ring.

The theoretical images in figure 4.20, correspond closely to those observed in figures 4.16 and 4.18. The intensity is at a maximum at points corresponding to maximum intensity for the linear polarisations incident on the S-wave plate but with the intensity distributed evenly between the inner and outer rings.

4.3 Discussion

The results in this chapter illustrated one of the most interesting aspects of the linear, passive regime of CD: polarisation. Looking at four different types of polarisation states: UPL; CPL; LPL; and APL & RPL beams, the effects of incident polarisation on the polarisation state of the resultant ring has been shown.

UPL produces a full CD ring pattern as seen in all preceding chapters. The polarisation state of a CD ring is such that diametrically opposite points are orthogonally polarised. Thus if the incident beam consists of light oscillating in all directions then there are photons available to populate all areas of the ring.

This is also true of CPL, however the use of different handedness of light produces subtle differences in the ring patterns observed away from the ring plane, most notably the appearance of a bright central spot for LCPL which is absent from RCPL.

Eliminating specific oscillation directions, by polarising the incident light in a single direction, a section of the ring will then be missing. This arises LPL, whereby a section of the ring which is orthogonally polarised to the plane of incident polarisation is missing, resulting in a crescent shaped beam. This is one of the most straightforward polarisation effects but one that has numerous interesting implications for applications. Among the applications found so far that take advantage of the polarisation properties of CD are its use in multiplexing and demultiplexing in free space for communications purposes [24], where a crystal is used to produce a CD ring, certain sections of which are then selectively amplitude modulated before a second crystal transforms the ring back to the incident beam now encoded with the amplitude information. The formation of a so-called ‘Optical

Vault' is another application, a three dimensional optical trap which can be selectively opened and closed by changing the polarisation of the incident beam [26]. The effect has also been utilised in one such application in this work, a polarisation detector, the details of which comprise chapter 6.

The use of the more unusual polarisation states results in changes to the intensity distribution but the polarisation of the ring plane pattern remains unchanged, with the use of a polariser illustrating that the same sections of the ring have the same polarisation states. The intensity is redistributed into two equal, close, concentric rings from the usual pair of high intensity outer ring and much lower intensity inner ring.

4.4 Summary

In this chapter a number of different polarisation states and their effects on a CD beam were investigated. Images, both experimental and theoretical, were shown for UPL; CPL; LPL; and APL & RPL polarised beams. The case of UPL and CPL was found to be identical in the ring plane, but differences emerge with the use of CPL away from the ring plane. This work formed the basis for our earlier Optics Letters paper in this area [32]. LPL results in sections of the ring being missing, thus producing a crescent shaped beam rather than a complete ring. The results from this section of the work we published in Optics Express [31]. APL and RPL produce beams whose intensity is redistributed from the typical CD ring pattern giving two equal intensity concentric rings. These results were published in 2014 in a further Optics Letters paper [33].

5 Non Linear Conical Diffraction

A further area for investigation that has been mostly overlooked is the expansion from linear to nonlinear conical diffraction (CD). This chapter outlines efforts to update and expand on the pioneering work of Shih and Bloembergen in the 1960s [12] and that of Schell and Bloembergen in the late 1970s [13-14] into second harmonic (SH) CD. Using improved techniques and equipment, the image quality of their original work is replicated in greater detail and the effects of polarisation on the type of second harmonic generation (SHG) and patterns produced is investigated.

Figure 5.1 An example of a simultaneously frequency doubled, CD ring pattern.

5.1 Introduction

The early 1960's played host to a revolution in optics with the introduction of the laser. For the first time, a high powered, high intensity light source was readily available and it wasn't long before previously unobservable effects were being seen in new experiments. The main area for new discoveries was the area of nonlinear optics. SHG is widely recognised as the first example of nonlinear optics when it was first demonstrated in a famous 1961 paper by Franken et al. [55] following shortly after the first lasers were made available. The process involves a beam of light incident on a medium which has non zero second order susceptibility. The polarisation of this beam in the crystal consists of two terms, described generally as:

$$\tilde{\mathrm{P}}^{(2)}(\mathrm{t}) = 2\epsilon_0\chi^{(2)}\mathrm{E}\mathrm{E}^{*} + \left(\epsilon_0\chi^{(2)}\mathrm{E}^2\mathrm{e}^{-\mathrm{i}2\omega\mathrm{t}}\right) \qquad (5.1)$$

The expression consists of a term at zero frequency and one at double frequency (2ω). This second term in the polarisation expression can lead to generation of radiation at 2ω, the second harmonic. This can be understood as the annihilation of two photons at ω to simultaneously create a single photon at 2ω.

Depending on the polarisation states of the incident photons (whether perpendicular to the optic axis (ordinary (o)) or in the direction of the optic axis (extraordinary (e)), different types of SHG can occur. The types of SHG are: Type 0 (ee → e), Type I (oo → e), and Type II (oe → e). The crystal used in these experiments, Potassium Titanyl Phosphate (KTP), is typically used for Type II SHG.

In order to observe the phenomenon the condition of phase matching needs to be met in order for constructive interference to lead to the SH field having an

appreciable intensity. The phase matching condition is such that the wave vectors of the incident beam and the generated beam lie in the same direction giving $\Delta k = 0$.

As introduced in section 1.1.4, experiments combining CD and nonlinearity were carried out soon after the introduction of the laser. In 1969 Shih and Bloembergen published their first work [12] detailing CD in nonlinear media, describing the

nonlinear analogue to internal conical refraction.

These results were expanded upon by Schell and Bloembergen in 1977 [13], and again in 1978 [14], with the publication of a more in depth theoretical study together with new experimental results.

The work in this chapter is purely experimental, but by way of providing a background of pertinent information, the theoretical treatment given by Schell and Bloembergen [14] is described in Appendix 3.

Figure 5.2, taken from Schell and Bloembergen's paper, shows the progression from nonlinear birefringence to CD and superimposed images of the fundamental and the generated SH signal.

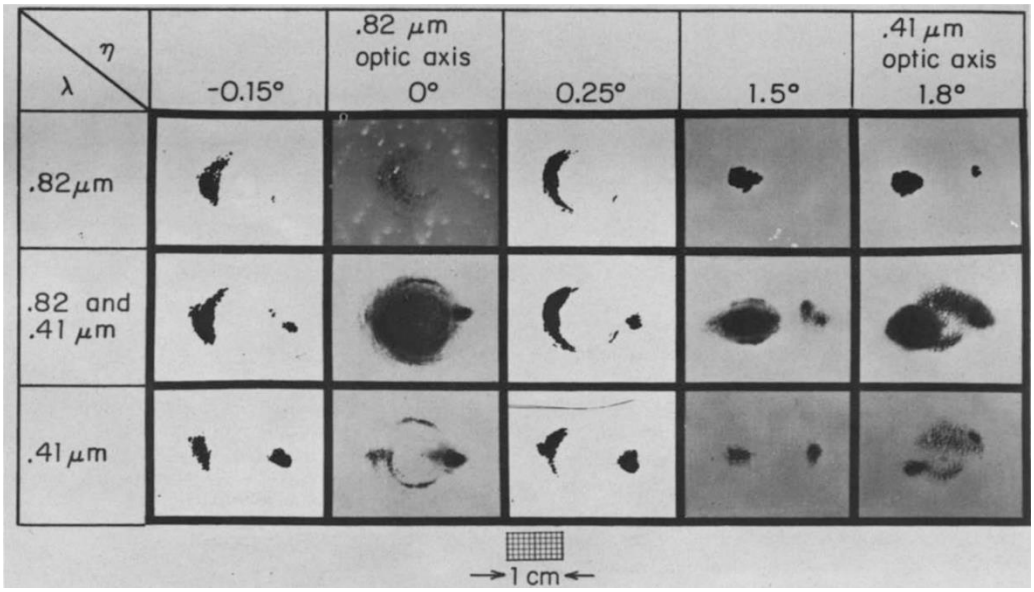

Figure 5.2 Original images from Schell and Bloembergen's 1978 paper showing the transition from before the fundamental optic axis (-0.15 ^{0}) to the SH optic axis (1.8 ^{0}) for the fundamental (820 nm, top row), the SH (410 nm, bottom row), and the superimposed image of both in the middle row.

The combination of two images, coupled with the techniques available at the time the experiments were carried out, led to images which, by today's standards, are unclear and lacking detail. In this chapter the aim of the work was to update Schell and Bloembergen's work with an improved imaging capability and increased power, whilst also carrying out an additional examination of the effects of polarisation on the produced SH beam.

The 1978 paper by Bloembergen et al. [14] also outlined the 'free' and 'forced' description of the phenomenon, whereby one of the generated SH beams is confined to the area of the crystal containing fundamental frequency. This is illustrated in the schematic shown in figure 5.3. The red area shows the position of

the beam confined to the region with fundamental frequency when the crystal is aligned to the fundamental optic axis (left). The blue areas are the 'free' spots which are unconfined. If the crystal is moved to the 532 nm optic axis (right) the 'free' and 'forced' patterns reverse with the ring now 'free' and the spots 'forced'.

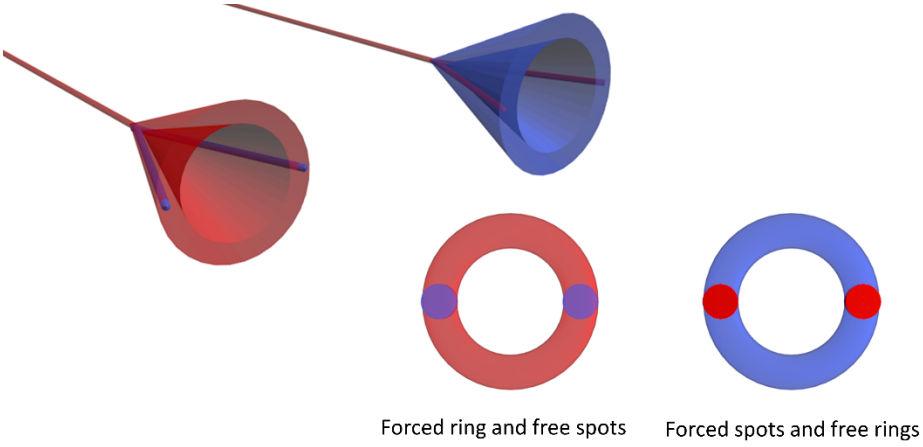

Figure 5.3 The 'free' and 'forced' scheme as described in Schell and Bloembergen's work. The beams confined to the area of fundamental frequency are shown in red while the 'free' beams are shown in blue. At the fundamental optic axis (left), the confined beam forms a ring, while at the SH optic axis the confined beam is the spots and the ring is 'free'.

Since those seminal papers in the 1970's there have been few efforts to re-examine nonlinear CD. In recent years theoretical work by Indik [20] as well as experimental work by Zolotvoskaya [56] comprise the major new work on the topic. Papers similar to the work presented here were reported in 2011 by Peet et al. [57] and by Turpin et al. in 2013 [58] and used a CD beam to then generate a frequency doubled beam in a second crystal. This differs from the work in this chapter, wherein CD and SHG occur simultaneously within the same crystal.

In order to carry out these experiments the system shown in figure 5.4 was used. The incident beam is a linearly polarised 1064 nm beam from a Coherent *Talisker* Ultra Nd:YVO_4 picosecond laser. Nonlinear effects, including SHG are dependent on intensity, as seen by the second term in (5.1) being proportional to E^2 and thus the intensity of the incident electric field. Prior to this investigation nano-second or less intense lasers were used in similar experiments. In the present case, the pico second laser facilitated higher intensity, and thus more intricate detail and feature definition within the observed rings. The polarisation was controlled using a half wave plate and the incident beam was collimated by a two lens system with a linear magnification of 2 (consisting of a 100 mm Newport KBX064 lens and a 200 mm KPX106 lens). A 250 mm focussing lens (Newport KPX073) was then used to obtain a spot size of ≈ 90 µm. The beam was then incident on a 10 mm KTP crystal, with its **G** pseudovector oriented vertically upwards (y direction in figure 5.4). An imaging lens (f = 35 mm Newport KPX376) was used to image the beam profile at various points and a coloured glass bandpass filter (BG-18 from Thorlabs) was used to isolate the SH 532 nm signal from the fundamental 1064 nm signal. The system was

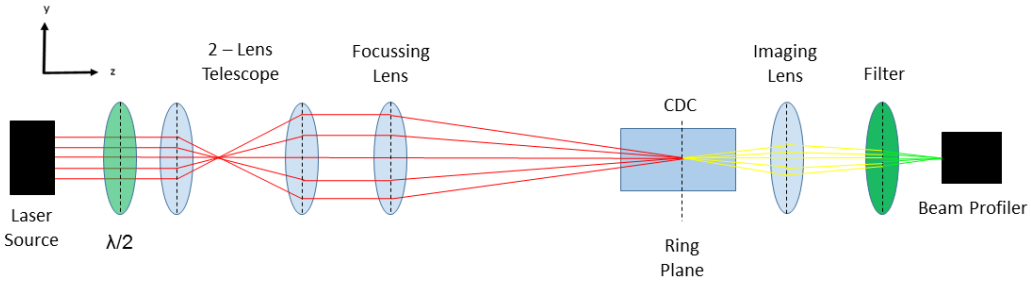

Figure 5.4 The experimental system used. The incident beam passes through a wave plate(λ/2) which was used to control polarisation, a collimating telescope with magnification m = 2, a focussing lens of 250 mm focal length, the KTP crystal, an imaging lens (IL) and finally a bandpass filter (f) to isolate the SH signal from the fundamental before being captured by the beam profiler

aligned and the images shown in figure 5.5, 5.6, and 5.7 in the results section of this chapter were produced. Where needed, an analyser was placed between the bandpass filter and the beam profiler. The crystal was mounted on a series of stacked translation stages to allow for movement on all axes. To obtain analogous images to those shown in figure 5.2 the crystal was rotated between two points of interest, the fundamental and SH optic axes. These were found using the laser's 1064 nm and 532 nm outputs. The power for the fundamental images was > 1 mW, while the power to produce SHG was ≈ 1 W.

5.2 Results

5.2.1 Linear conical diffraction with KTP crystal

Figure 5.5 shows the case of linear CD, with a number of linear incident polarisations as shown by the red arrows on the left hand side. As expected, the patterns observed for KTP are relatively indistinguishable from those of KGW. The only difference would be in the size of the ring due to the crystal length. An equivalent length KGW crystal was not available. Regardless, the four different polarisations produce the familiar crescent shape pattern in the ring plane with a section missing corresponding to the section of the ring orthogonally polarised to the incident beam polarisation. This is carried through from one Raman spot to the other. These images were taken at the fundamental harmonic of the Talisker laser.

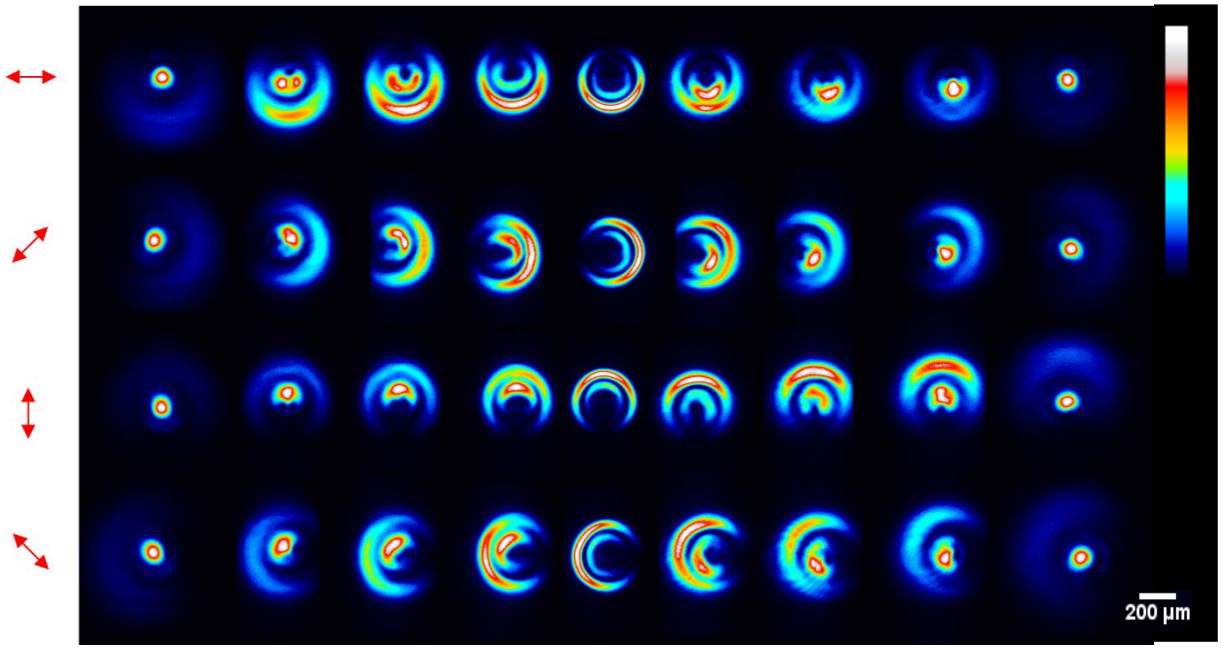

Figure 5.5 Images spanning the range of a CD beam propagation for four incident polarisations (indicated by the red arrows) using a KTP crystal.

Figure 5.6 shows the patterns in the ring plane for the fundamental (a), and the SH beams (b - c). The red arrows indicate polarisation, as in figure 5.5. Column (b) shows the SH pattern as it seen by the beam profiler immediately following the filter ('F') in figure 5.4. Using a polariser, the SH pattern was analysed to determine its polarisation. The yellow arrows at the top of columns (c) and (d) show the orientation the of the analyser during image acquisition. As can be seen in rows 1 and 3, horizontal and vertical incident polarisations lead to the appearance of two spots with orthogonal polarisation and a ring made up of a mixture of the two polarisations. Rows 2 and 4 show only a single spot and a ring where again the ring is made up of a mixture of horizontal and vertical polarisation.

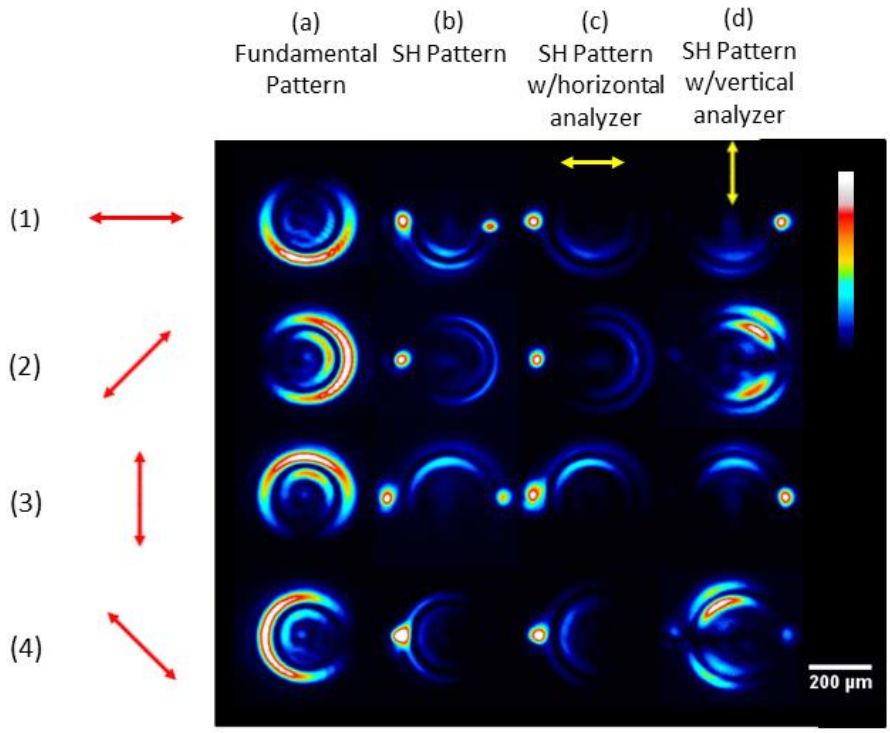

Figure 5.6 SH CD patterns in the ring plane for four incident polarisations. The red arrows indicate incident polarisation, the yellow arrows indicate the orientation of a polariser used to analyze the polarisation state of the SH pattern. (a) Fundamental pattern, (b) SH pattern, (c) SH pattern with horizontally oriented polariser, and (d) SH pattern with vertically oriented polariser.

The conversion efficiency was approximately 0.02% for the ring and around 0.08% for the high intensity spot. The intensity of the spot was redistributed to two spots in the cases where two spots are observed so the conversion efficiency for each individual spot in those cases was ~0.04%. Figure 5.7 shows the transition between the fundamental optic axis and the SH optic axis. Row (a) and (d) show the transition from CD to double refraction as the crystal is rotated for the fundamental. The polarisation of the first three rows is the same; the final two rows are analogous to Bloembergen's experiments shown in figure 5.2. Row (b) shows the transition from double refraction at the fundamental optic axis to CD at the 532 nm optics axis for an incident 532 nm beam. Row (c), the SH pattern, can be seen to be made up of a combination of rows (a) and (b). Row (e) is the equivalent of row (c) for the alternative polarisation shown by the red arrows.

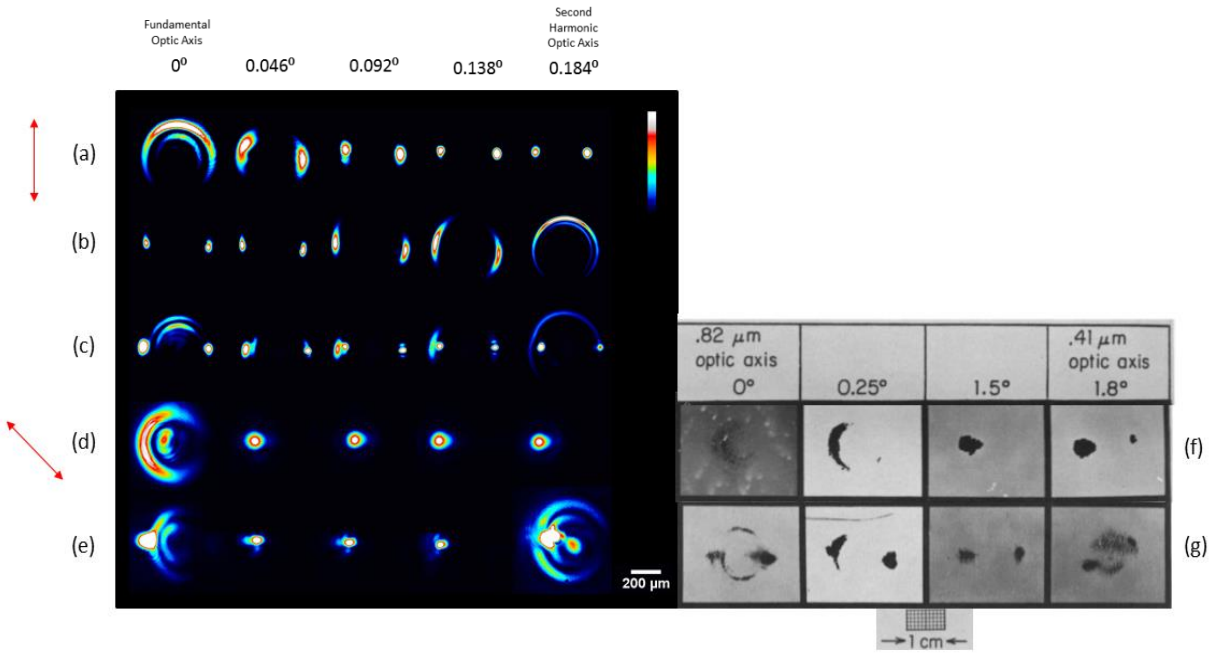

Figure 5.7 Transition between the fundamental and SH optic axes for (a) an incident fundamental beam with polarisation as indicated by the red arrow, (b) an incident 532 nm beam with the same polarisation, and (c) the SH beam of the same polarisation, consisting of the sum of the two patterns (a) and (b). Row (d) and (e) are equivalent to rows (a) and (c) for an alternative polarisation as shown by the second red arrow. The equivalent images from Bloembergen et al. are shown in (f) and (g).

5.3 Discussion

As mentioned in the introduction, SHG typically occurs in one of three types under phase matched conditions. The types are determined by the polarisations of the photons which combine to form a single new photon which has the SH wavelength, or is frequency doubled. The types are: Type 0 (ee → e), Type I (oo → e), and Type II (oe → e). The crystal used in these experiments, KTP, is typically used for Type II SHG. However, here, both Type I and Type II are observed depending on the incident polarisation.

The nature of the conditions under which CD can be observed necessitate phase matching to occur, so phase matching in this case is automatic. Phase matching normally requires the path length in the medium to be less than the coherent length, the length over which a phase difference of π will be introduced. This condition typically requires careful consideration of the polarisation of the fields in the crystal and the orientation of the crystal itself to ensure phase matching occurs. However, in this case, this requirement is met by the shape of the CD beam within the crystal.

As shown in figure 5.8, the length of forward propagation at any given point is less than the coherence length due to the conical nature of the beam's propagation. This leads to SHG occurring as if the coherence length is never exceeded allowing

for ‘phase-matched’ CD to occur without rigorous phase matching measures being taken.

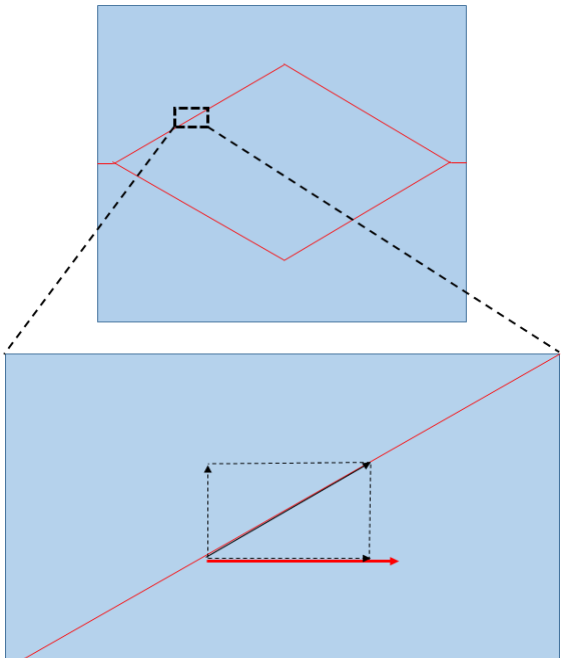

Figure 5.8 Schematic of the beam within the KTP crystal. The red arrow in the larged lower figure corresponds to the coherence length of the crystal. It is longer than the horizontal component of the actual path of the beam and as such the coherence length is not exceeded.

Horizontal and vertical polarisations (row 1 & 3, figure 5.6) give rise to Type I SHG, while angles of ± 45^{o} (row 2 & 4, figure 5.6) lead to Type II SHG. In the case of Type I there are two spots in addition to the forced cone, with the spots being orthogonally polarised to each other. For Type II only one spot is present and for both ± 45^{o} it is horizontally polarised. In all cases the ring consists of a combination of horizontal and vertical polarisations. Additionally in the case of Type II the area of the cone where a second spot would appear is purely horizontally polarised, and is missing when the vertical analyser is used.

Figure 5.7 shows the transition between the fundamental (left hand column) and SH (right hand column) optic axes and the inversion of the ‘free’ and ‘forced’ beams from a ‘forced’ cone and ‘free’ spots at the fundamental axis to a ‘free’ cone and ‘forced’ spots at the SH axis as shown in the schematic in figure 5.3. Row (a) is the transition for a 1064 nm incident beam showing the transition from CD at the optic axis to double refraction at the SH axis. Row (b) shows the same transition for a 532

nm incident beam, going from double refraction to CD. Row (c) is the transition for the SH 532 nm beam from a ‘forced’ cone and two ‘free’ spots to a ‘free’ cone and two ‘forced’ spots as the unconfined beam undergoes CD and the confined beam goes from CD to double refraction.

The final two columns show the fundamental pattern for a 45^{o} incident beam undergoing the transition and a SH beam at 45^{o} undergoing the transition. This is analogous to the case examined by Schell and Bloembergen and is in close agreement with their results.

This work conformed again to the overarching theme of this thesis: to confirm theoretical predictions with state-of-the-art techniques and technology. However this work is part of the fundamental investigations into the phenomenon without which applications are not obvious. Trying to explore new avenues of use for the phenomenon without the necessary groundwork will lead to failure and the topic as a whole may well be put to rest if these applications are not found. So it is of paramount importance that the background information of the effect is thoroughly studied and understood before meaningful steps can be taken to translate this from a laboratory novelty to a real world application.

5.4 Summary

The images shown conform to the expected patterns described and shown by Schell and Bloembergen in their seminal papers from the late 1970s. Improved equipment and techniques allow for increased detail and clarity when compared to the images originally presented and for additional examination of the effects of different polarisation states on the pattern produced by the SH beam. The ‘free’ and ‘forced’ description remains an apt and elegant method of outlining the constituent parts of the pattern, with confined and unconfined beams having different polarisations indicative of types I and II SHG. The work contained in this chapter is also contained in our earlier publication [34].

This marks both an area for further study, as this work was purely investigative and fundamental in nature, and the end of the fundamental work carried out in this thesis. The next chapters outline a simple but effective application for the unique polarisation properties of CD and the potential areas for further and future work in the field.

6 Optical Sensor based on Conical Diffraction

An optical sensor to determine the polarisation of an incident beam utilising the unique polarisation properties of conical diffraction (CD) is designed and taken from the initial concept stage to a prototype device. This is then tested as a polarimeter, measuring the optical rotation introduced by optically active chemicals.

Figure 6.1 Effect on the CD pattern due to rotation of the plane of polarisation of the incident beam due to Carvone (top row) and Limonene (bottom row)

6.1 Introduction

6.1.1 Concept

The unique properties of CD that would potentially lend it to practical applications include the intensity profile in the ring plane, the so called 'bottle-beam' shape of its free space evolution, and its polarisation properties, among others. Some areas where these features have already been utilised include optical trapping [25 - 26], and communications [24] applications, as noted in previous chapters.

In this chapter a simple device, utilizing the unique polarisation properties of the phenomenon, is described to determine the polarisation of an incident beam. The device makes use of the effects of linear polarisation on the ring plane pattern. To refresh what was covered in chapter 4, particularly section 4.2.2, when an incident beam is linearly polarised the section of the CD ring which is orthogonally polarised to the incident beam will be missing (figure 6.2). Using this as a platform the device has a simple goal: to determine which section of the ring is missing and thus determine the angle of polarisation of the incident beam.

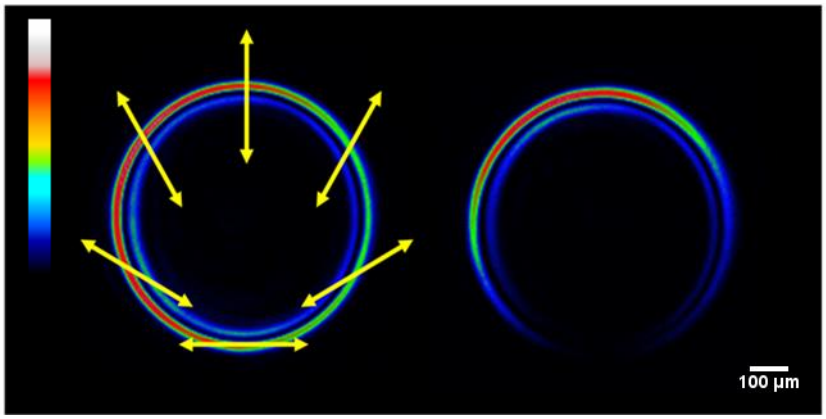

Figure 6.2 Polarisation state of a CD ring using CPL (left) and vertically LPL (right)

Current methods of determining the polarisation of a beam are either crude, using polarisers which need to be aligned and have the angle read manually, or overly sophisticated. One such sophisticated method, the use of subwavelength gratings and photodetectors requires complex subwavelength structures to be fabricated [59]. That device consists of three grating-photodetector pairs integrated on a single substrate. The method is wavelength dependent and additional devices are required for each wavelength to be tested leading to high costs. Other methods, including commercially available devices from ThorLabs [60], boast a high dynamic range, excellent accuracy and even a free laptop! However these devices cost between £5900 and £8750.

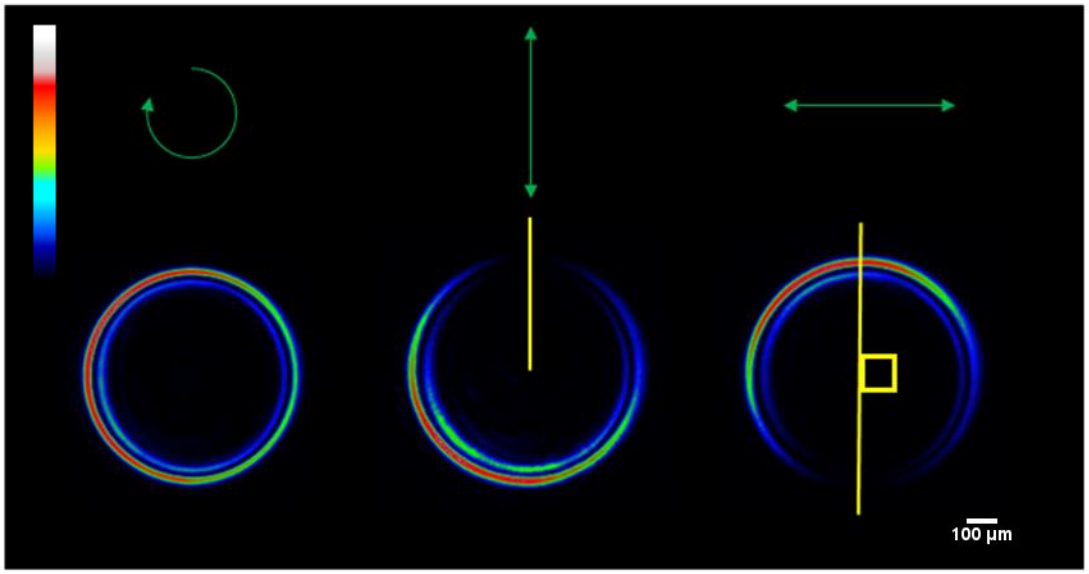

Figure 6.3 The 180^o CD ring shift for a 90^o incident beam shift. The green arrows indicate the incident polarisation with CPL on the left, vertical polarisation in the centre, and horizontal polarisation on the right. The yellow line is the angle of the missing section of the ring as it would be measured by the device. It can be seen that a 90^o rotation in the incident plane of polarisation results in a 180^o change in the CD pattern.

The materials used for the device proposed here are readily available in any well-equipped optics laboratory with the additional costs being for a KGW crystal and

camera. The crystal is not an insignificant investment, however the camera can be any commercially available standard camera. The crystal's response is instantaneous, so the only limiting factor on the speed of the device is the software used to determine the angle of polarisation.

The goals of this device are to design something simple to use, cost effective and fast. Devices based on this principle were independently demonstrated and recently described in [61] and [62]. The first of these devices is a complex two branch, analytical division of amplitude (DOA) polarimeter with high accuracy but also a large footprint and involved operation. While it is similar in principle, the intention of the device is different being designed to offer analytical information for use in optical metrology, among other areas. The second such device, described in [62], is similar to the device described here and achieves the same objectives of a simple and inexpensive configuration when compared to the first device. The device described here aimed to get the most accuracy possible from the simplest device in order to make something practical, fast and effectively 'pocket-sized'.

6.1.2 Design

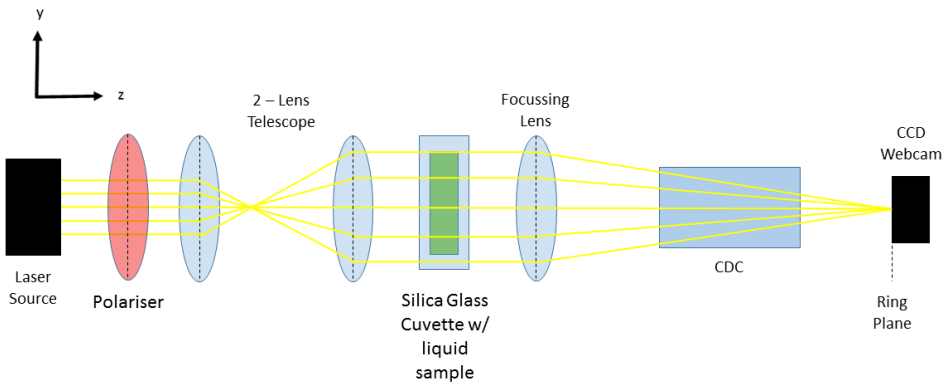

Figure 6.4 The basic schematic of the experimental setup. The collimated beam from a two lens telescope is incident on a focussing lens, CD crystal and a CCD sensor. These three items are the constituent parts of the device.

The design of the device proposed (figure 6.3) was based on the standard setup for a CD experiment. An incident beam would pass through an external telescope (consisting of a 100 mm Newport KBX064 lens and a 200 mm KPX106 lens), then focussing lens, the KGW crystal and finally onto a sensor. The focussing lens, crystal and sensor would be housed together and comprise 'the device'. A lens with a short focal length would be used to reduce the distance between the lens and the sensor and thus the device as a whole, however in these experiments the prototype device was an open bench top set up using a 150 mm focussing lens (Newport KPX064). The crystal was held with its pseudo vector pointing vertically upwards (y direction in figure 6.4) thus giving a constant ring pattern to use as a standard against which the missing section could be compared and the angle of polarisation calculated. The sensor used was a Logitech C270 HD webcam, the camera was disassembled and the housing discarded. The lens covering the camera sensor was also removed. The sensor is 1280 x 720 pixels at 2.8 μm^2 per pixel, giving an active area of 3.58 mm x 2.02 mm. The ring radius from the crystal used was 426 µm. In these experiments a

594 nm yellow HeNe (Newport R-30602) was used but the device works for any wavelength provided a pure, undoped, crystal is used. Changes to the incident wavelength would require slight realignment of the crystal to account for dispersion. The limitations on the spectral range of the device are due to the image sensor used, as the crystal itself is compatible with infrared and near infrared wavelengths.

Figure 6.5 The proposed housing for the device. A simple molded plastic housing which holds the lens, crystal, and sensor. The dimensions of the housing are determined by the focal length of the lens and the crystal length.

The proposed housing (figure 6.5) is one that would contain as the beam entrance an aperture leading to a focussing lens, immediately following the focussing lens the crystal would be held in place and the beam would then fall upon the sensor. A short focal length lens and short crystal could reduce the size of the device to little bigger than a match box.

The software needed for the device was written in MATLAB. Excerpts of the final code (C8) are available in the appendix 4.

The software went through several iterations using various methods before the final method was arrived at. Initially the sensor area was divided into a 2 x 2 grid and the relative intensity was used to determine the position of the missing section of the ring. This was extremely limited in that it gave one of eight possible positions as opposed to giving an actual value for the polarisation angle. Nevertheless it

served as a useful basis for the following iterations. The ring also needed to be centred exactly on the sensor for the measurement to be accurate.

The next iteration further divided the sensor area into an 8 x 8 grid, this provided more accuracy but the same problem was present with a gross value rather than a value in an acceptable range being provided. Another discarded approach was to have a sample reference image against which the live image from the device would be compared. This method was potentially more accurate but even very slight variations in the intensity of the ring patterns between the live image and the reference image led to severely inaccurate readings.

The final code uses a user defined area to determine where the ring and missing section are accurately and calculates the incident polarisation based on this.

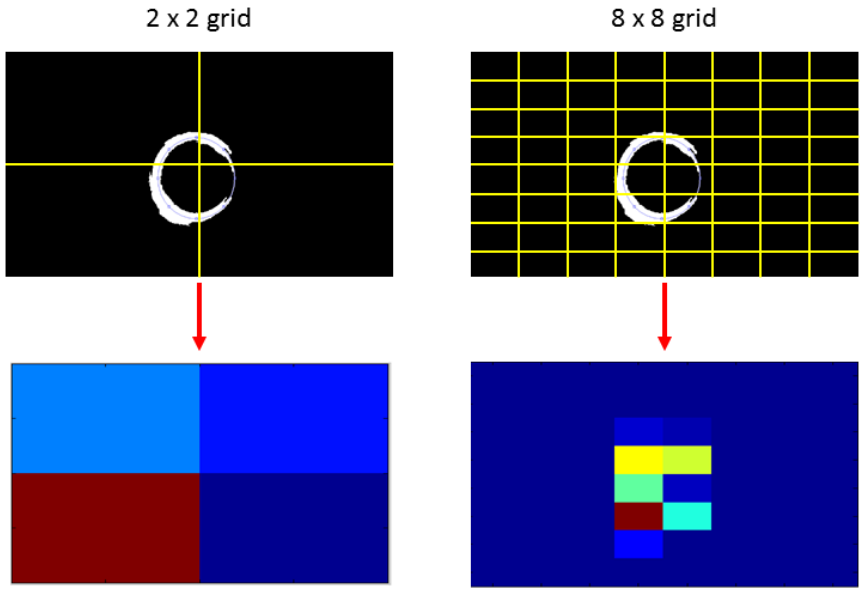

Figure 6.6 The initial two iterations of the MATLAB program to run the device. In the first, on the left, a 2 x 2 grid was used. As can be seen from the sample case, if the beam is not centred there will be a false reading. In this method, the missing section is found by detecting the highest intensity and moving diametrically opposite, a false reading of the location of the highest intensity will give a false reading of the incident beam.

6.1.3 Operation

There are several steps to using the device. Having aligned the device as in all other experiments, the MATLAB script is run. A still image is taken from the live video feed of the ring profile. This image is then binarized producing an image consisting only of values 1 and 0. This is all carried out automatically. At this point user input is required. The user is prompted to draw a circle over the entire ring pattern. Once this is done the rest of the process is also automated. The values along the circle are found (1's or 0's) and from this the missing area is determined. This is then used to calculate the polarisation angle of the incident beam. As noted by Lloyd [6] a full rotation of a CD ring takes place over 180^{o} so if the incident beam is rotated in a complete circle the CD ring will rotate twice. Figure 6.7 shows the steps involved in operation of the device. The whole operation takes approximately 15 seconds.

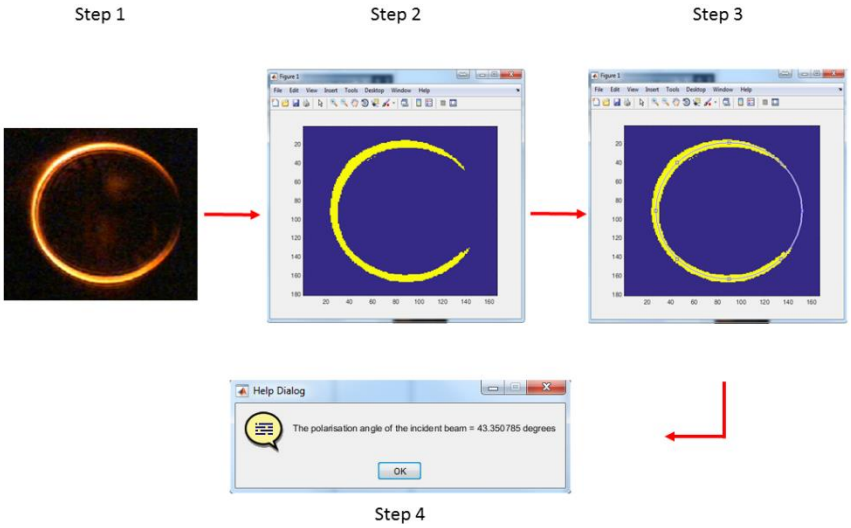

Figure 6.7 The steps involved in operation of the final device. A screenshot from the live video is captured by the program (Step 1), binarized and presented to the user (Step 2), the user then draws a circle over the ring (Step 3), and finally the software determines the location of the missing section of the ring and gives the angle of the plane of polarisation of the incident beam.

6.2 Results

The sensor was tested using incident light at four polarisations corresponding to 0, 45, 90 and 135^{o}, controlled using a linear polariser (AHWP05M-600 from Thorlabs). The results are shown in figure 6.8. The number on top is the target value set using a waveplate to control the incident polarisation. The bottom value is the average of five measurements of the polarisation angle using the device. The angle was found to be in close agreement with the expected values, with the largest deviation being less than 4^{o}. Vertically upwards was arbitrarily chosen as 0^{o}, and the starting point for the measurements can be easily adjusted. While the accuracy of the device lay with ±4^{o} for all measurements taken, the precision was much higher with measurements by the device falling within ±1^{o}. This implies the inaccuracy of the measurements arises in the method of producing the polarised light, i.e. slightly incorrect placement of the waveplate.

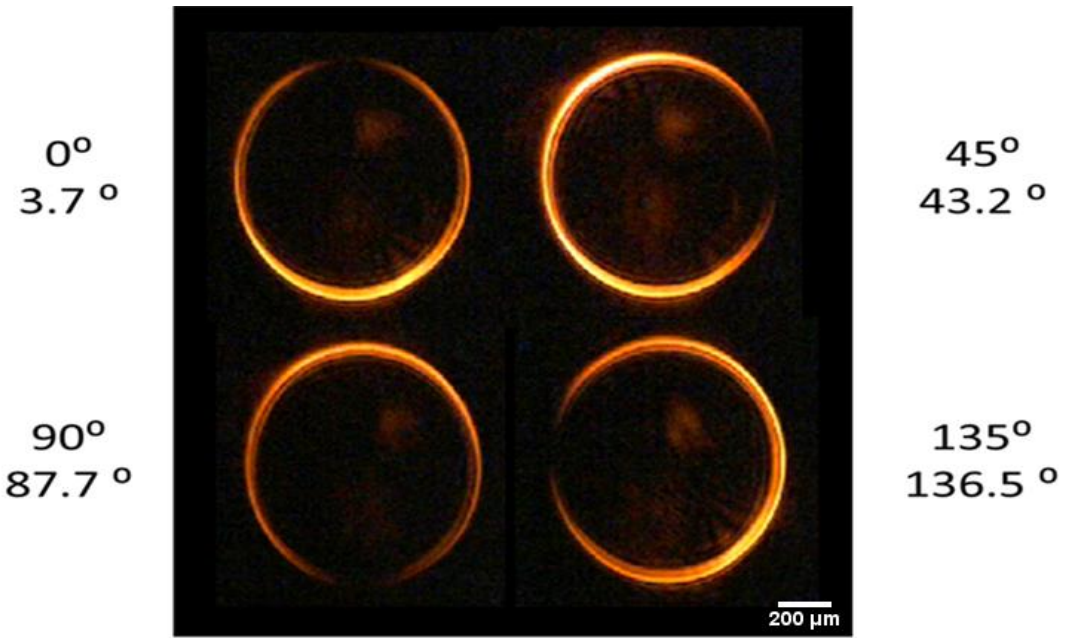

Figure 6.8 Results of test to determine the angle of polarisation of the incident beam. The top values show the target value, while the lower numbers show the measured value. All values are within ±4 ^{0}of the target value.

In order to test the viability and sensitivity of the device in a real-world application, a series of polarimetry measurements were carried out using liquids that rotate the plane of polarization of light passing through them. (R)-(-)-Carvone and (R)-(+)-Limonene were used with a fused silica glass cuvette containing a neat sample of the chemical placed in the beam path. The device was then used to measure the rotation of the plane of polarisation.

Initial experiments made use of L- and D- Alanine, as well as L-Valine, but the level of rotation observed was indistinguishable due to issues with maintaining a steady temperature and a lack of pure, clean hydorcloric acid with which to prepare the solutions necessary. Due to this the decision was made to switch to chemicals that readily produced optical rotation without any preparation needed.

The reported ranges of specific rotation - from Sigma Aldrich - are -61^{o}/dm for Carvone [63] and 96 to 105^{o}/dm for Limonene [64]. The expected rotation for various path lengths were calculated using:

$$\alpha = [\alpha]_{\lambda}^{T} l c \tag{6.1}$$

where $[\alpha]_{\lambda}^{T}$ is the quoted specific rotation value, α is the observed rotation value, c is the concentration of the chemical and l is the path length in dm. In this case as neat liquids were used the concentration was 1 and for a single glass cuvette the path length is 1 cm. Therefore, the expected rotation for each sample was one-tenth the quoted value per cuvette. Three cuvettes were used in series to increase the path length in steps of 1 cm from 1 to 3 cm. The results are shown in figures 6.9 and 6.10 overleaf. The expected values for Carvone at 1, 2, and 3 cm are -6.1^{o}, -12.2^{o}, and -18.3^{o}. The measured values are -6.3^{o}, -10.8^{o}, and -16.1^{o}. For Limonene

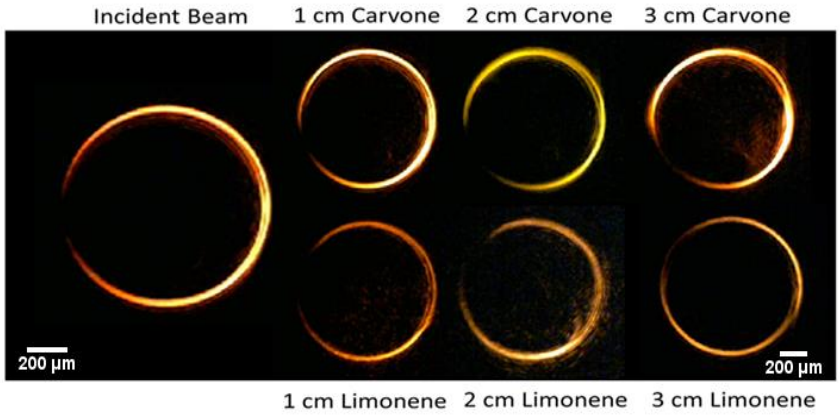

Figure 6.9 Ring plane patterns with and without multiple effective concentrations of Carvone and Limonene showing rotation in opposite directions for each of the chemicals.

the expected values are 9.6°, 19.2°, and 28.8° with measured values of 6.5°, 19.8°, and 25.8°. The sources of error in the measurements arise due to aligning the linear polariser to alter the polarisation state of the incident beam (estimated at ±1°) and in applying the user drawn ring to define the area of interest. This second source of error was much harder to estimate and arises due to the ends of the crescent shaped beam not being clearly defined and the limitations of the camera's resolution. This was estimated to be ±2°. Finally an element of random error due to stray light, camera noise or other sources was estimate to be ±1°, giving a total estimated error of ±4°.

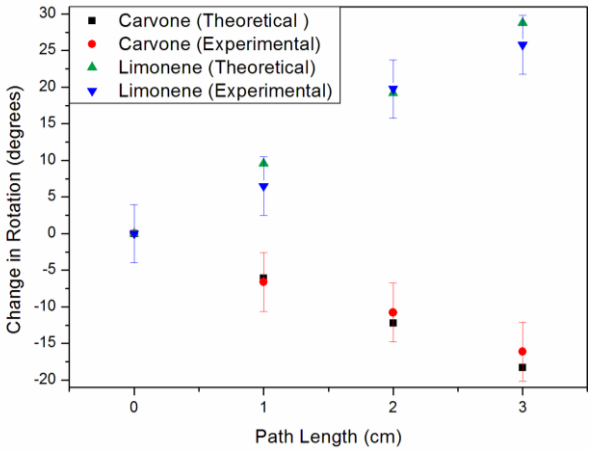

Figure 6.10 The change in the angle of the polarisation of the incident beam due to propagation through optically active liquids. The black squares and green triangles are theoretical values, whole the red circle and blue triangles are experimental values.

6.3 Discussion

The device in its current state offers a proof of concept for an application for CD. Current polarimeters, as mentioned in the introduction, either consist of complex, expensive equipment or cruder methods using polarisers and analysers which while effective and simple, rely on the judgement of the user in most cases to determine the angles involved. This device seeks to bridge the gap between highly sophisticated devices and methods that rely on the user measuring by eye. This has to an extent been achieved as the device gives an accurate measurement based on its determination of the angle, however the fact that a user drawn ring defines the area of interest allows for some human error. Thus, the accuracy of the device is currently limited by a number of factors: human error, crystal purity, camera resolution, incident beam quality, and stray light. The crystal purity was not a factor that could be controlled or easily quantified in this case. Beam quality and stray light were able to be minimised with the experimental setup and working in darkened conditions. Camera resolution was a trade-off between a high end camera and cost effectiveness. The camera chosen had a reasonable 720p resolution and was a consumer grade, mid-range camera. In further iterations of the device this could be replaced with a higher end, perhaps even a research grade beam profiler, such as the Spiricon 720U used in other experiments in this work. The issue of human error in the judgement of the placement of the ring can be addressed in further software versions by fully automating the process and eliminating user input altogether.

For comparison's sake, a tradition polariser analyser set up was used to carry out the same measurements and the accuracy was found to be comparable, falling within ±4^{o} of the expected value but with precision of ±2^{o}, implying a slightly larger problem with human error in the case of the polariser analyser measurements.

As a first proof of concept the device offers promising accuracy and ease of use. It is cost effective and the limiting factors in its effectiveness can be addressed in later iterations with improvements to both hardware and software [35].

6.4 Summary

This prototype device represents another avenue for a potential application for CD. In this first working iteration the device displays promising accuracy and ease of use to provide a simple, cost effective solution to a common optical problem. With further iteration the device could be potentially robust enough to provide accurate reading on additional types of polarisation. Furthermore the device represents the potential of CD to become a practical, commonly used phenomenon in laboratories. The real barriers to the use of CD are the scarcity of current applications, however the only way to increase the number of applications is to get more and more people investigating the phenomenon. A simple and accessible tool such as this one could encourage users to explore other areas where CD could be used and to find those much sought after applications.

7 Summary and outlook

The work presented here consists primarily of fundamental investigations into various aspects of the conical diffraction (CD) phenomenon, expanding in a (somewhat) logical manner from the simplest case of single crystal CD, through complexities such as cascade set ups, polarisation and non-linear systems, to a proposal for a novel application of the phenomenon.

During the time this work was carried out the field has itself expanded at a respectable pace with more fundamental experiments giving way to applicable, practical uses of the phenomenon. This work fits into the bigger picture as a part of the fundamental foundation upon which the next chapter in the story of CD can be built, if you'll forgive the mixed metaphor. This was a very interesting time to work in this area, the initial remit of the project was quickly reached by the larger CD community and the prospect of a single researcher working alone in this area became untenable as groups tackled the problems in a manner more efficient and timely than any lone person could.

The contributions this work has made to the field include experimental confirmation of the prediction of the effect of handedness of circularly polarised light (CPL) in cascade experiments away from the ring plane [32], an update of the pioneering work of Bloembergen et al. in the 1970s including new investigations into polarisation effects in non-linear CD [34], the first examination of the effects of azimuthally and radially polarised light in CD [33], and a prototype of a novel device showing how simply CD can be utilised in the search for applications [35].

Where the field goes from here is anyone's guess. The range of applications being found at the current time is relatively small [24–28], [59], [63–65] but hints at larger possibilities to come. Some of the areas that I think the field could move in and deserve further investigation are outlined below.

7.1 Outlook

7.1.1 Second Harmonic Generation

The second harmonic generation (SHG) in this work was fundamental in nature and an update on the initial work carried out in the 1970s. Apart from [56] the only other SHCD work carried out recently was [57], [58] which both regard using a CD incident beam to produce SHG in a second crystal. Further work in this area would involve a complete and rigorous theoretical treatment incorporating the theoretical advances made since the initial theoretical work in the 1970s. The unique intensity patterns, polarisation properties, and multiple types of SHG occurring in a single beam, as well as the fact that phase matching is not required when using this method means there are a number of potential areas to be investigated in order to further understand the CD phenomenon, perhaps offering further insight into SHG along the way, and, of course, to find any applications which would utilise the properties of a SHCD beam.

7.1.2 Electrogyration

An area that may prove particularly interesting is to use an electrically induced spatial dispersion effect to observe any changes to the observed pattern of CD. This is known as electrogyration [68] and has a number of interesting applications allowing for the control of light electrically in devices such as high-voltage

measurements, electro-optic switches, and as a method to modulate the plane of polarisation of light. This effect is only observable with a limited number of electro-optic materials; biaxial crystals, like the ones used in this work, number amongst them. How this effect would affect a CD beam is unexplored at this time and may offer a fruitful area of investigation as the electrogyration effect is finding use in a number of other areas including nanomaterials science [69].

7.1.3 Sensors

As far as the sensor described in this work, there is potential to increase its functionality by using higher quality parts and designing a method which can determine not only linear polarisations but circular, elliptical, and radial and azimuthal polarisations. In order to maintain the quick-use, small footprint tool design of the sensor there is a limit to the amount of parts which can be added. This presents a challenge on the software end which may be insurmountable without additional parts but is a direction in which the current prototype device could potentially be taken.

Apart from the simple sensor outlined in chapter 6 there are a number of possibilities for other sensors utilising CD. A more sophisticated Division of Amplitude polarimeter has been described in [61] offering a wider range of measured variables and boasting increased accuracy but with a much larger footprint and more complex set up. This is simply one type of sensor which would utilise the polarisation properties of the phenomenon. The use of the phenomenon in potential communications applications [24] has shown that it could prove useful in encoding and decoding information with increased bandwidth and security. This

would require both a method to encode the information and some type of sensor to retrieve the information once it is transmitted or otherwise used.

7.1.4 Lasers

CD lasers were first reported on a number of years ago [27]–[29] with a patent for the first CD laser design awarded at the University of Dundee [45], and have been briefly investigated since by others in a European research project [70]. That project unfortunately ended suddenly in 2014 without reporting on its aims. There are however still a number of benefits to laboratory lasers using CD including high beam quality ($M^2 = 1$) with slope efficiency close to the theoretical maximum and the ability to have both Gaussian and CD output beams. They offer potential applications in brightness and power scaling in solid-state bulk lasers. There has also been some work into improving beam quality and directivity by using CD [65]. Integrating CD into widely available lasers could bring these benefits to the industry at large. There are a number of issues related to efficiency and power that need to be overcome in this effort that provide areas for potential further study.

References

[1] R. P. Graves, *Life of Sir William Rowan Hamilton, Royal Astronomer of Ireland*, vol. 32, no. 835. Dublin: Hodges, Figgis & Co., 1885.

[2] W. R. Hamilton, "Theory of Systems of Rays," *Trans. R. Irish Acad.*, vol. 15, pp. 69–174, 1828.

[3] W. R. Hamilton, "Supplement to an Essay on the Theory of Systems of Rays," *Trans. R. Irish Acad.*, vol. 16, pp. 1–61, 1830.

[4] W. R. Hamilton, "Third supplement to an essay on the theory of systems of rays," *Trans. R. Irish Acad.*, no. 17, pp. 1–144, 1837.

[5] Tcd.ie, "'Humphrey Lloyd - Provost & President : Trinity College Dublin, The University Of Dublin, Ireland,'" *N.P.*, 2015. [Online]. Available: http://www.tcd.ie/provost/history/former-provosts/h_lloyd.php.

[6] H. Lloyd, "On the Phenomena Presented by Light in Its Passage along the Axes of Biaxal Crystals," *Trans. R. Irish Acad.*, vol. 17, no. 1831, pp. 145–157, 1831.

[7] H. Lloyd, "Further Experiments on the Phænomena presented by Light in its Passage along the Axes of Biaxal Crystals.," *Philos. Mag.*, vol. 2, no. 3, pp. 207–210, 1833.

[8] J. C. Poggendorf, "Ueber die konische Refraction," *Ann. der Phys. und Chemie*, vol. 124, no. 11, pp. 461–462, 1839.

[9] W. Voigt, "Bemerkung zur Theorie der konischen Refraktion," *Ann. Phys.*, vol. 324, no. 1, pp. 14–21, 1906.

[10] C. V. Raman, "Conical Refraction in Biaxial Crystals," *Nature*, vol. 107, no. 2702, pp. 747–747, 1921.

[11] Nobel Media AB 2013, "The Nobel Prize in Physics 1981." [Online]. Available: http://www.nobelprize.org/nobel_prizes/physics/laureates/1981/siegbahn-facts.html.

[12] H. Shih and N. Bloembergen, "Conical refraction in second-harmonic generation," *Physical Review*, vol. 184, no. 3. pp. 895–904, 1969.

[13] A. J. Schell and N. Bloembergen, "Second harmonic conical refraction," *Opt. Commun.*, vol. 21, no. 1, pp. 150–153, 1977.

[14] A. J. Schell and N. Bloembergen, “Laser studies of internal conical diffraction. III. Second Harmonic conical refraction in α-iodic acid,” *J. Opt. Soc. Am.*, vol. 18, no. 6, p. 2592, 1978.

[15] A. M. Belskii and A. P. Khapalyuk, “Internal conical refraction of bounded light beams in biaxial crystals,” *Opt. Spectrosc.*, vol. 44, pp. 436–439, 1978.

[16] M. V Berry, “Conical diffraction asymptotics: fine structure of Poggendorff rings and axial spike,” *J. Opt. A Pure Appl. Opt.*, vol. 6, no. 4, pp. 289–300, Apr. 2004.

[17] M. V Berry, “Conical diffraction from an N -crystal cascade,” *J. Opt.*, vol. 12, no. 7, p. 075704, Jul. 2010.

[18] M. V Berry and M. R. Jeffrey, “Conical diffraction complexified: dichroism and the transition to double refraction,” *J. Opt. A Pure Appl. Opt.*, vol. 8, no. 12, pp. 1043–1051, Dec. 2006.

[19] A. M. Belsky and M. A. Stepanov, “Internal conical refraction of light beams in biaxial gyrotropic crystals,” *Opt. Commun.*, vol. 204, no. 1–6, pp. 1–6, 2002.

[20] R. A. Indik and A. C. Newell, “Conical refraction and nonlinearity.,” *Opt. Express*, vol. 14, no. 22, pp. 10614–10620, 2006.

[21] V. Peet and D. Zolotukhin, “Free-space evolution of focused Gaussian beams transformed by conical diffraction in a biaxial crystal,” *Opt. Commun.*, vol. 283, no. 15, pp. 3011–3016, Aug. 2010.

[22] D. Carnegie, G. S. Sokolovski, T. Kalkandjiev, and E. U. Rafailov, “Conical refraction: Beam evolution,” in *2011 Conference on Lasers and Electro-Optics Europe and 12th European Quantum Electronics Conference, CLEO EUROPE/EQEC 2011*, 2011.

[23] C. F. Phelan, D. P. O’Dwyer, Y. P. Rakovich, J. F. Donegan, and J. G. Lunney, “Conical diffraction and Bessel beam formation with a high optical quality biaxial crystal.,” *Opt. Express*, vol. 17, no. 15, pp. 12891–12899, 2009.

[24] A. Turpin, Y. Loiko, T. K. Kalkandjiev, and J. Mompart, “Free-space optical polarization demultiplexing and multiplexing by means of conical refraction,” *Opt. Lett.*, vol. 37, no. 20, p. 4197, 2012.

[25] D. P. O’Dwyer, K. E. Ballantine, C. F. Phelan, J. G. Lunney, and J. F. Donegan, “Optical trapping using cascade conical refraction of light,” *Opt. Express*, vol. 20, no. 19, p. 21119, 2012.

[26] A. Turpin, V. Shvedov, C. Hnatovsky, Y. V. Loiko, J. Mompart, and W. Krolikowski, “Optical vault : A reconfigurable bottle beam based on conical refraction of light,” vol. 21, no. 22, pp. 26335–26340, 2013.

[27] A. Abdolvand, K. G. Wilcox, T. K. Kalkandjiev, and E. U. Rafailov, “Conical refraction Nd : KGd (WO 4) 2 laser,” vol. 18, no. 3, pp. 2753–2759, 2010.

[28] K. G. Wilcox, A. Abdolvand, T. K. Kalkandjiev, and E. U. Rafailov, “Laser with simultaneous Gaussian and conical refraction outputs,” *Appl. Phys. B*, vol. 99, no. 4, pp. 619–622, May 2010.

[29] J. Hellstrom, H. Henricsson, V. Pasiskevicius, U. Bunting, and D. Haussmann, “Polarization-tunable Yb : KGW laser based on internal conical refraction,” *Opt. Lett.*, vol. 32, no. 19, pp. 2783–2785, 2007.

[30] M. V. Berry, M. R. Jeffrey, and J. G. Lunney, “Conical diffraction: observations and theory,” *Proc. R. Soc. A Math. Phys. Eng. Sci.*, vol. 462, no. 2070, pp. 1629–1642, Jun. 2006.

[31] S. Grant and A. Abdolvand, “Evolution of conically diffracted Gaussian beams in free space,” *Opt. Express*, vol. 22, no. 4, pp. 13201–13207, Feb. 2014.

[32] S. D. Grant and A. Abdolvand, “Left- and right-circularly polarized light in cascade conical diffraction,” *Opt. Lett.*, vol. 37, no. 24, pp. 5226–5228, 2012.

[33] S. D. Grant, S. A. Zolotovskaya, W. A. Gillespie, T. K. Kalkandjiev, and A. Abdolvand, “Azimuthally and radially polarized light in conical diffraction.,” *Opt. Lett.*, vol. 39, no. 7, pp. 1988–91, 2014.

[34] S. D. Grant, S. A. Zolotovskaya, T. K. Kalkandjiev, W. A. Gillespie, and A. Abdolvand, “On the frequency-doubled conically-refracted Gaussian beam,” *Opt. Express*, vol. 22, no. 18, p. 21347, Aug. 2014.

[35] S. D. Grant, S. Reynolds, and A. Abdolvand, “Optical sensing of polarization using conical diffraction phenomenon,” *J. Opt.*, vol. 18, no. 2, p. 025609, 2016.

[36] A. M. Belsky and M. A. Stepanov, “Internal conical refraction of coherent light beams,” *Opt. Commun.*, vol. 167, no. 1, pp. 1–5, 1999.

[37] M. Born and E. Wolf, *Princples of Optics*. 1980.

[38] V. V. Filippov, N. V. Kuleshov, and I. T. Bodnar, “Negative thermo-optical coefficients and athermal directions in monoclinic KGd(WO4)2 and KY(WO4)2 laser host crystals in the visible region,” *Appl. Phys. B Lasers Opt.*, vol. 87, no. 4, pp. 611–614, May 2007.

[39] M. V. Berry and M. R. Jeffrey, “Chapter 2 Conical diffraction: Hamilton’s diabolical point at the heart of crystal optics,” *Progress in Optics*, vol. 50. pp. 13–50, 2007.

[40] Croptics.eu, “‘CR Optics :: Home,’” *N.p.*, 2015. [Online]. Available: http://www.croptics.eu/.

[41] Ophiropt.com, "'CCD Beam Profiler | USB Silicon Camera – Ophir,'" *N.p.*, 2015. [Online]. Available: http://www.ophiropt.com/laser-measurement-instruments/beam-profilers/products/industrial-applications/the-cameras/SP620U.

[42] R. T. Darcy, D. McCloskey, K. E. Ballantine, B. D. Jennings, J. G. Lunney, P. R. Eastham, and J. F. Donegan, "White light conical diffraction.," *Opt. Express*, vol. 21, no. 17, pp. 20394–403, Aug. 2013.

[43] R. T. Darcy, D. Mccloskey, K. E. Ballantine, J. G. Lunney, P. R. Eastham, and J. F. Donegan, "Conical diffraction intensity profiles generated using a top-hat input beam," vol. 22, no. 9, pp. 150–155, 2014.

[44] A. Abdolvand, "Conical diffraction from a multi-crystal cascade: experimental observations," *Appl. Phys. B*, vol. 103, no. 2, pp. 281–283, Apr. 2011.

[45] A. Abdolvand, T. Kalkandjiev, and E. U. Rafailov, "Optical system e.g. laser for, e.g. bio-photonic application, has optical element which creates and reconstructs cone refracted beam from input beam," WO2010084317-A1 CA2750297-A1 EP2389608-A1 CN102388334-A US2012082179-A1 JP2012515935-W US8542712-B2 JP5603880-B2 CN102388334-B.

[46] S. D. Grant and A. Abdolvand, "Left- and right-circularly polarized light in cascade conical diffraction," vol. 37, no. 24, pp. 5226–5228, 2012.

[47] D. P. O'Dwyer, C. F. Phelan, Y. P. Rakovich, P. R. Eastham, J. G. Lunney, and J. F. Donegan, "The creation and annihilation of optical vortices using cascade conical diffraction.," *Opt. Express*, vol. 19, no. 3, pp. 2580–2588, 2011.

[48] A. Turpin, Y. V. Loiko, T. K. Kalkandjiev, and J. Mompart, "Multiple rings formation in cascaded conical refraction," *Opt. Lett.*, vol. 38, no. 9, pp. 1455–1457, 2013.

[49] V. Peet, "Variable two-crystal cascade for conical refraction," *Opt. Lett.*, vol. 40, pp. 2405–2408, 2015.

[50] Y. V Loiko, M. a Bursukova, T. K. Kalkanjiev, E. U. Rafailov, and J. Mompart, "Fermionic transformation rules for spatially filtered light beams in conical refraction," *Complex Light Opt. Forces V*, vol. 7950, p. SPIE, 2011.

[51] A. Turpin, "Cascaded Conical Refraction," Universitat Autonoma de Barcelona, 2011.

[52] M. Beresna, M. Gecevičius, P. G. Kazansky, and T. Gertus, "Radially polarized optical vortex converter created by femtosecond laser nanostructuring of glass," *Appl. Phys. Lett.*, vol. 98, no. 20, 2011.

[53] C. F. Phelan, J. F. Donegan, and J. G. Lunney, "Generation of a radially polarized light beam using internal conical diffraction," *Opt. Express*, vol. 19, no. 22, p. 21793, 2011.

[54] Altechna.com, "'S-Waveplate (Radial Polarization Converter),'" *N.P.*, 2015. [Online]. Available: http://www.altechna.com/product_details.php?id=1048&product_name=S-waveplate+%28Radial+Polarization+Converter%29.

[55] P. A. Franken, A. E. Hill, C. W. Peters, and G. Weinreich, "Generation of optical harmonics," *Phys. Rev. Lett.*, vol. 7, no. 4, pp. 118–119, 1961.

[56] S. A. Zolotovskaya, A. Abdolvand, T. K. Kalkandjiev, and E. U. Rafailov, "Second-harmonic conical refraction: observation of free and forced harmonic waves," *Appl. Phys. B*, vol. 103, no. 1, pp. 9–12, Apr. 2011.

[57] V. Peet and S. Shchemelyov, "Frequency doubling with laser beams transformed by conical refraction in a biaxial crystal," *J. Opt.*, vol. 13, no. 5, p. 055205, May 2011.

[58] A. Turpin, Y. V Loiko, T. K. Kalkandjiev, J. Trull, C. Cojocaru, and J. Mompart, "Type I and type II second harmonic generation of conically refracted beams.," *Opt. Lett.*, vol. 38, no. 14, pp. 2484–6, 2013.

[59] E. Chen, S. Y. Chou, and S. Member, "A Novel Device for Detecting the Polarization Direction of Linear Polarized Light Using Integrated Subwavelength Gratings and Photodetectors," *Ieee Photonics Technol. Lett.*, vol. 9, no. 9, pp. 1259–1261, 1997.

[60] Thorlabs.de, "'Polarimeter Systems, High Dynamic Range, Free-Space And Fiber-Coupled,'" *N.P.*, 2015. [Online]. Available: http://www.thorlabs.de/newgrouppage9.cfm?objectgroup_id=1564.

[61] A. Peinado, A. Lizana, A. Turpín, C. Iemmi, K. Todor, J. Mompart, and J. Campos, "Optimization , tolerance analysis and implementation of a Stokes polarimeter based on the conical refraction phenomenon," *Opt. Express*, vol. 23, no. 5, pp. 5453–5469, 2015.

[62] A. Lizana, I. Estévez, A. Turpin, C. Ramirez, A. Peinado, and J. Campos, "Implementation and performance of an in-line incomplete Stokes polarimeter based on a single biaxial crystal," *Appl. Opt.*, vol. 54, no. 29, pp. 8758–8765, 2015.

[63] Sigmaaldrich.com, "'(R)-(−)-Carvone 98% | Sigma-Aldrich,'" *N.P.*, 2015. [Online]. Available: http://www.sigmaaldrich.com/catalog/product/aldrich/124931?lang=en&region=GB.

[64] Sigmaaldrich.com, "'(R)-(+)-Limonene 97% | Sigma-Aldrich,'" *N.P.*, 2015. [Online]. Available: http://www.sigmaaldrich.com/catalog/product/sigma/183164?lang=en&region=GB.

[65] V. Peet, "Improving directivity of laser beams by employing the effect of conical refraction in biaxial crystals.," *Opt. Express*, vol. 18, no. 19, pp. 19566–19573, 2010.

[66] T. A. King, W. Hogervorst, N. S. Kazak, N. A. Khilo, and A. A. Ryzhevich, “Formation of higher-order Bessel light beams in biaxial crystals,” *Opt. Commun.*, vol. 187, no. 4–6, pp. 407–414, 2001.

[67] M. A. Stepanov, “Transformation of Bessel beams under internal conical refraction,” *Opt. Commun.*, vol. 212, no. 1–3, pp. 11–16, 2002.

[68] O. G. Vlokh and R. O. Vlokh, “The Electrogyration Effect,” *Opt. Photon. News*, no. 20, pp. 34–39, 2009.

[69] I. V. Kityk, “Optically Induced Electrogyrators Based on Nanomaterials,” in *2007 9th International Conference on Transparent Optical Networks*, 2007, pp. 202–203.

[70] Hicore.eu.com, “HiCORE - High Brightness Conical Refraction Lasers,” *N.P.*, 2015. [Online]. Available: http://hicore.eu.com/. [Accessed: 25-Sep-2015].

Appendix 1 – Single Crystal Theory

This theoretical treatment is based on the work of Michael Berry as outlined in summarized form in [39]. Starting at the first Hamilton equation (A1.1), which describes the group velocity (v_g) of a wave with wave vector **k**:

$$\mathrm{v_g} = \nabla_{\mathbf{k}}\omega(\mathbf{k}) \tag{A1.1}$$

where $\nabla_{\mathbf{k}}$ is the change in angular frequency ω, with respect to wave vector $\mathbf{k}$, and $\omega(\mathbf{k})$ is the Hamiltonian which generates rays inside the crystal with momentum $\mathbf{k}$ wave vector. This shows that the direction of ray propagation is perpendicular to the wave surface at the diabolical point, as shown in figure 1.2.

Displacement (d**k**) along a wave surface with constant ω is given by

$$\mathbf{S}\cdot\mathrm{d}\mathbf{k} = \frac{1}{2}\omega\mathrm{Re}[\mathbf{E}^*\cdot\mathrm{d}\mathbf{D} - \mathrm{d}\mathbf{E}^*\cdot\mathbf{D} + \mathbf{H}\cdot\mathrm{d}\mathbf{B}^* - \mathrm{d}\mathbf{H}\cdot\mathbf{B}^*] = 0 \tag{A1.2}$$

where from Maxwell's equations, $\mathbf{E}^*$ is the conjugate transpose of the electric field, **D** is the displacement field, **H** is the magnetizing field, **B** is the magnetic field, and **S** is the Poynting vector showing the energy flux, in this case the direction of propagation of rays. Following on from equation (A1.2) the ray direction described in (A1.1) can be written as:

$$\mathbf{S} = \mathrm{Re}\mathbf{E}^*\times\mathbf{H} \tag{A1.3}$$

From this and Maxwell's equations, (A1.3) can be rewritten as

$$\mathbf{S} = \frac{\mathrm{c}}{\mathrm{n_k}}\mathrm{Re}[\mathbf{E}^*\cdot\mathbf{D}\mathbf{e_k} - \mathbf{E}^*\cdot\mathbf{e_k}\mathbf{D}] \tag{A1.4}$$

Using the coordinate system $\mathrm{k_x}$, $\mathrm{k_y}$, and $\mathrm{k_z}$ with k lying along the $\mathbf{e}_z$ direction (the optic axis), the vectors $\mathbf{D}$ and $\mathbf{E}$ can be written as:

$$\mathbf{D} = \begin{pmatrix} D_x \\ D_y \\ 0 \end{pmatrix}, \mathbf{E} = \begin{pmatrix} E_x \\ E_y \\ E_z \end{pmatrix} = \frac{1}{\varepsilon_0}(\boldsymbol{\varepsilon}')^{-1}\mathbf{D} \tag{A1.5}$$

where $\boldsymbol{\varepsilon}'$ is the rotated dielectric matrix which relies upon the following conditions:

- Rotation about the y axis does not affect anything related to the 2 axis as $\mathbf{e}_y = \mathbf{e}_2$
- $\mathbf{k}$ lying along the optic axis means that the xx and yy elements are equivalent
- And $\boldsymbol{\varepsilon}$ and $\boldsymbol{\varepsilon}'$ have the same determinant and trace.

From this it follows that:

$$\varepsilon_0(\boldsymbol{\varepsilon}')^{-1} = \frac{1}{n_2^2}\begin{pmatrix} 1 & 0 & 0 \\ 0 & 1 & 0 \\ 0 & 0 & 1 \end{pmatrix} + \begin{pmatrix} 0 & 0 & \sqrt{\alpha\beta} \\ 0 & 0 & 0 \\ \sqrt{\alpha\beta} & 0 & \alpha - \beta \end{pmatrix} \tag{A1.6}$$

And

$$\mathbf{E}^* \cdot \mathbf{D} = \frac{1}{\varepsilon_0 n_2^2}\left(|D_x|^2 + |D_y|^2\right)$$
$$E_z = \mathbf{E}^* \cdot \mathbf{e}_\mathbf{k} = \frac{1}{\varepsilon_0}\sqrt{\alpha\beta}D_x \tag{A1.7}$$

Equations (A1.6) and (A1.7), together with rewriting $\mathbf{D}$ in polar coordinates with angle φ gives the ray surface, non-circular cone created by the rotation of $\mathbf{S}$, shown in figure 1.2.

$$\mathbf{S} = \frac{cD^2}{\varepsilon_0 n_2^3}\left(\mathbf{e}_z - \frac{1}{2}\tan 2A(\mathbf{e}_x + \mathbf{e}_x \cos 2\phi + \mathbf{e}_y \sin 2\phi)\right) \tag{A1.8}$$

with semi-angle A given by

$$\tan 2A = n_2^2\sqrt{\alpha\beta} \tag{A1.9}$$

where αand β relate the refractive indices of the material:

$$\alpha = \frac{1}{n_1^2} - \frac{1}{n_2^2} \qquad \beta = \frac{1}{n_2^2} - \frac{1}{n_3^2} \tag{A1.10}$$

This is the Maxwell equation description of the wave surface of the cone. Using geometrical optics leads to a more practical formulation with simpler expressions which can be used more readily in experimental work.

In order to use the geometrical theory one needs to consider the properties of the crystals involved and the incident beam. The crystals used in all experiments in this work have refractive indices such that:

$$n_1 < n_2 < n_3 \tag{A1.11}$$

and give rise to a semi-angle A in the resulting cone found, after rearranging (A1.9), with

$$A = \frac{1}{n_2}\sqrt{(n_2 - n_1)(n_3 - n_2)} \tag{A1.12}$$

The incident beam is assumed symmetrical and Gaussian, with wavenumber k_0, and with the electric field profile in the beam radius given by:

$$E_0(r) = \exp\left(-\frac{r^2}{2\omega^2}\right) \tag{A1.13}$$

Starting from the path length from the entrance face of the crystal of length l to a point beyond the crystal at a distance z for waves with wavevector components k_x and k_y.

$$\text{path length} = k_x(x - x_i) + k_y(y - y_i) + l\sqrt{k_0^2 n_{k_\pm}^2 - k_x^2 - k_y^2} + (z - l)\sqrt{k_0^2 - k_x^2 - k_y^2} \tag{A1.14}$$

The geometrical theory utilises a number of dimensionless variables (A1.15) based on the geometry of the beam passing through the crystal as shown in figure A1.1.

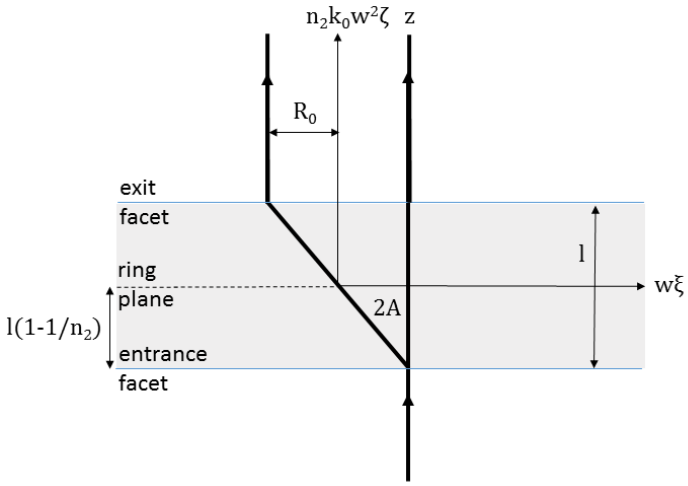

Figure A1.1 Schematic of geometry of beam passing through crystal (shaded area) giving rise to dimensionless variables in equation A1.14, adapted from figure 7 in [39]

$$\boldsymbol{\rho} = \{\xi, \eta\} = \rho\{\cos\phi, \sin\phi\} \equiv \frac{1}{w}\{x + R_0, y\}$$

$$\boldsymbol{\kappa} = \{\kappa_x, \kappa_y\} = \kappa\{\cos\phi_{\boldsymbol{\kappa}}, \sin\phi_{\boldsymbol{\kappa}}\} \equiv w\{k_x, k_y\} \tag{A1.15}$$

$$\rho_0 \equiv \frac{R_0}{w}$$

The transverse position and transverse wavelength, $\boldsymbol{\rho}$ and $\boldsymbol{\kappa}$ respectively are given in terms of the beam radius w. Additionally $\boldsymbol{\rho}$ is measured from the centre of the cylinder, and ρ_0 is the radius of the cylinder in terms of w. Near the intersection of the wave surfaces $\boldsymbol{\kappa}$ is small so the local geometry of the wave surfaces can be described as:

$$n_{k_\pm} = n_2\left(1 + \frac{A(-\kappa_x \pm \kappa)}{k_0 n_2 w}\right) \tag{A1.16}$$

At this point, as all angles are small, a paraxial approximation is used to simplify the situation, allowing (A1.14) to be rewritten as

$$\text{path length} = k_0(n_2 l + z - l) + \Phi_\pm(\boldsymbol{\kappa}, \boldsymbol{\rho}, \boldsymbol{\rho_i}) \tag{A1.17}$$

where

$$\begin{gathered}\Phi_\pm(\boldsymbol{\kappa}, \boldsymbol{\rho}, \boldsymbol{\rho_i}) \equiv \boldsymbol{\kappa}\cdot(\boldsymbol{\rho} - \boldsymbol{\rho_i}) \pm \kappa\rho_0 - \frac{1}{2}\kappa^2\zeta \\ \zeta \equiv \frac{l + n_2(z-l)}{n_2 k_0 w^2}\end{gathered} \tag{A1.18}$$

ζ is a dimensionless variable describing propagation distance from the ring plane at ζ = 0.

The emergent field depends on the following integrals:

$$\begin{aligned}C_0(u, u_0) &= \int_0^\infty dqq\exp\left\{-\frac{1}{2}q^2\right\}\cos(u_0 q)\, J_0(uq) \\ C_1(u, u_0) &= \int_0^\infty dqq\exp\left\{-\frac{1}{2}q^2\right\}\sin(u_0 q)\, J_1(uq)\end{aligned} \tag{A1.19}$$

These are the Belsky-Khapalyuk equations, the fundamental equations in the Belsky-Khapalyuk theory, involving Bessel functions J_0 and J_1. The solution to these equations gives rise to the exact paraxial theory of the phenomenon.

$$\begin{aligned}I(\rho, \zeta; \rho_0) = \frac{1}{1+\zeta^2}\Bigg[&\left|C_0\left(\frac{\rho}{\sqrt{1+i\zeta}}, \frac{\rho_0}{\sqrt{1+i\zeta}}\right)\right|^2 \\ &+ \left|C_1\left(\frac{\rho}{\sqrt{1+i\zeta}}, \frac{\rho_0}{\sqrt{1+i\zeta}}\right)\right|^2\Bigg]\end{aligned} \tag{A1.20}$$

Equation (A1.20) is the exact theory in its simplest form as quoted by Berry in [30]. In order to get simplify towards a more 'user-friendly' form, a few assumptions and simplifications are needed, as discussed below.

Only the case of $\rho_0 >> 1$ is of interest, as this is a requirement for clear observation of the effect. In this case equations (A1.19) can be approximated by one function:

$$C_0(u, u_0) \approx C_1(u, u_0) \approx \frac{1}{\sqrt{u_0}} f(u - u_0) \tag{A1.21}$$

where

$$\begin{aligned} f(s) &= \frac{1}{\sqrt{2\pi}} \int_0^\infty dq \sqrt{q} \exp\left(-\frac{1}{2}q^2\right) \cos\left(qs - \frac{1}{4}\pi\right) \\ &= \frac{1}{4\sqrt{2\pi}} |s|^{3/2} \exp\left(-\frac{1}{4}s^2\right) \left[K_{3/4}\left(\frac{1}{4}s^2\right) \right. \\ &+ \operatorname{sgn}(s) K_{1/4}\left(\frac{1}{4}s^2\right) \\ &\left. + \pi\sqrt{2}\Theta(-s)\left(I_{3/4}\left(\frac{1}{4}s^2\right) - I_{1/4}\left(\frac{1}{4}s^2\right)\right)\right] \end{aligned} \tag{A1.22}$$

where I and K are modified Bessel functions of the first and second kind respectively. In this case the intensity of the rings can be described much more simply as:

$$I_{\text{rings}} = \frac{2}{\rho_0 (1 + \zeta^2)^{3/4}} \left| f\left(\frac{\rho - \rho_0}{\sqrt{1 + i\zeta}}\right) \right|^2 \tag{A1.23}$$

This equation, (A1.23), together with (A1.21) and (A1.22) forms the basis of the theoretical modelling carried out in this work which is outlined in chapter 2, along with chapters 3 and 4 for various situations and experimental requirements. More rigorous theoretical analysis is available in references [16], [30], [39].

Appendix 2 – Cascade Theory

The present theoretical treatment is based on that of Michael Berry as outlined in [17]. The starting point of the theory is to consider a unitary matrix $U_{totN}(\kappa)$ which describes the transformation of a wave having wavenumber κ, as it passes through the crystal cascade. The incident Gaussian beam is acted upon by this matrix and Fourier transformation is used to find the electric field:

$$E_N(\rho,\zeta) = \frac{1}{2\pi}\iint d\kappa \exp\left\{i\left(\kappa\cdot\rho - \frac{1}{2}i\kappa^2\zeta\right)\right\} U_{totN}(\kappa)\overline{E}_0(\kappa) \tag{A2.1}$$

The matrix $U_{totN}(\kappa)$ can be written as the product of the unitary matrices for the individual crystals in the cascade giving:

$$U_{totN}(\kappa) = U_N(\kappa)U_{N-1}(\kappa)\dots U_2(\kappa)U_1(\kappa) \tag{A2.2}$$

Using three Pauli matrices s_1, s_2, and s_3 and the identity matrix, I, the unitary matrix of a single crystal in the cascade can be written as:

$$U_n(\kappa) = \exp\{-i\rho_{0n}\kappa(\sin(\phi-\gamma_n)\,s_1 + \cos(\phi-\gamma_n)s_3)\} \tag{A2.3}$$

And using Dirac notation re-written as:

$$U_n(\kappa) = \exp(-i\rho_{0n}\kappa)\,|n,+\rangle\langle n,+| + \exp(i\rho_{0n}\kappa)|n,-\rangle\langle n,-| \tag{A2.4}$$

Where the eigenvectors are:

$$|n,+\rangle = \begin{pmatrix}\cos(\frac{1}{2}(\phi-\gamma_n))\\ \sin(\frac{1}{2}(\phi-\gamma_n))\end{pmatrix} \qquad |n,-\rangle = \begin{pmatrix}\sin(\frac{1}{2}(\phi-\gamma_n))\\ -\cos(\frac{1}{2}(\phi-\gamma_n))\end{pmatrix} \tag{A2.5}$$

In order to make use of these the overlaps of the eigenvectors from the crystals m and n are required. These can be written as:

$$\langle \mathrm{m},+|\mathrm{n},+\rangle = \langle \mathrm{m},-|\mathrm{n},-\rangle = \langle \mathrm{n},+|\mathrm{m},+\rangle = \langle \mathrm{n},-|\mathrm{m},-\rangle = \cos(\Gamma_{\mathrm{mn}})$$

$$\langle \mathrm{m},+|\mathrm{n},-\rangle = \langle \mathrm{n},-|\mathrm{m},+\rangle = -\langle \mathrm{n},+|\mathrm{m},-\rangle = -\langle \mathrm{m},-|\mathrm{n},+\rangle = \sin(\Gamma_{\mathrm{mn}}) \quad \text{(A2.6)}$$

and reduce to simple trigonometric expressions involving Γ_{mn} which is half the difference between the angles of orientation of crystal m and crystal n.

As (A2.2) can be described as a sum of overlaps, the eigenvalue indices of $+$ and $-$ can be described as paths. This leads to the unitary matrix for the whole cascade being rewritten as:

$$\mathrm{U_{totN}}(\kappa) = \mathrm{A_{++}}|\mathrm{N},+\rangle\langle 1,+| + \mathrm{A_{+-}}|\mathrm{N},+\rangle\langle 1,-| + \mathrm{A_{-+}}|\mathrm{N},-\rangle\langle 1,+| + \mathrm{A_{--}}|\mathrm{N},-\rangle\langle 1,-| \quad \text{(A2.7)}$$

where:

$$\mathrm{A_{\varepsilon N\varepsilon 1}} = \sum_{\varepsilon} \exp\{-\mathrm{i}\kappa\rho_{\mathrm{tot}}(\varepsilon)\}\mathrm{F_{\varepsilon N\varepsilon 1}}(\varepsilon) \quad \text{(A2.8)}$$

$$\mathrm{F_{\varepsilon N\varepsilon 1}}(\varepsilon) \equiv \langle \mathrm{N}, \varepsilon_{\mathrm{N}}|\mathrm{N}-1, \varepsilon_{\mathrm{N}-1}\rangle \ldots \langle 2, \varepsilon_2|1, \varepsilon_1\rangle \quad \text{(A2.9)}$$

Now the natural ordering of matrices leads to $\mathrm{U_{totN}}(\kappa)$ being once again rewritten as:

$$\mathrm{U_{totN}}(\kappa) = \mathrm{U_{0totN}}(\kappa)\mathrm{I} + \mathrm{U_{2totN}}(\kappa)\mathrm{i}s_2 + \mathrm{U_{3totN}}(\kappa)s_3 + \mathrm{U_{1totN}}(\kappa)s_1 \quad \text{(A2.10)}$$

Where the individual numbered terms are given by:

$$U_{0totN}(\kappa) = \frac{1}{2}[(A_{++} + A_{--})\cos\Gamma_{N1} + (A_{+-} + A_{-+})\sin\Gamma_{N1}]$$

$$U_{1totN}(\kappa) = \frac{1}{2}[(A_{++} - A_{--})\sin(\phi - \gamma_{N1}) - (A_{+-} + A_{-+})\cos((\phi - \gamma_{N1})]$$

$$U_{2totN}(\kappa) = \frac{1}{2}[(A_{++} + A_{--})\sin\Gamma_{N1} + (A_{+-} + A_{-+})\cos\Gamma_{N1}]$$

$$U_{3totN}(\kappa) = \frac{1}{2}[(A_{++} - A_{--})\cos(\phi - \gamma_{N1}) - (A_{+-} + A_{-+})\sin((\phi - \gamma_{N1})] \quad \text{(A2.11)}$$

At this point the original electric field from equation (A2.1) can be written as a function of matrix M and incident uniform polarisation e_0:

$$E_N(\rho, \zeta) = M_N(\rho, \zeta)e_0 \quad \text{(A2.12)}$$

The matrix $M_N(\rho,\zeta)$ takes the same form as $U_{totN}(\kappa)$ and is where the Belsky-Khapalyuk equations described in chapter 2 reappear. $M_N(\rho,\zeta)$ can be written as:

$$M_N(\rho, \zeta) = M_{0N}(\rho, \zeta)I + M_{2N}(\rho, \zeta)is_2 + M_{3N}(\rho, \zeta)s_3 + M_{1N}(\rho, \zeta)s_1 \quad \text{(A2.13)}$$

Where $M_{0N,1N,2N,3N}$ are given by:

$$M_{0N}(\rho,\zeta) = \cos\Gamma_{N1}\sum_{\varepsilon} B_0\big(\rho,\zeta;\rho_{tot}(\varepsilon)\big)F_{++}(\varepsilon) + \sin\Gamma_{N1}\sum_{\varepsilon} B_0\big(\rho,\zeta;\rho_{tot}(\varepsilon)\big)F_{+-}(\varepsilon)$$

$$M_{2N}(\rho,\zeta) = \sin\Gamma_{N1}\sum_{\varepsilon} B_0\big(\rho,\zeta;\rho_{tot}(\varepsilon)\big)F_{++}(\varepsilon) - \cos\Gamma_{N1}\sum_{\varepsilon} B_0\big(\rho,\zeta;\rho_{tot}(\varepsilon)\big)F_{+-}(\varepsilon)$$

$$M_{3N}(\rho,\zeta) = \cos(\phi-\gamma_{N1})\sum_{\varepsilon} B_1\big(\rho,\zeta;\rho_{tot}(\varepsilon)\big)F_{++}(\varepsilon) + \sin(\phi-\gamma_{N1})\sum_{\varepsilon} B_1\big(\rho,\zeta;\rho_{tot}(\varepsilon)\big)F_{+-}(\varepsilon)$$

$$M_{1N}(\rho,\zeta) = \sin(\phi-\gamma_{N1})\sum_{\varepsilon} B_1\big(\rho,\zeta;\rho_{tot}(\varepsilon)\big)F_{++}(\varepsilon) - \cos(\phi-\gamma_{N1})\sum_{\varepsilon} B_1\big(\rho,\zeta;\rho_{tot}(\varepsilon)\big)F_{+-}(\varepsilon) \quad \text{(A2.14)}$$

From these equations, together with equation (A2.1), it can be seen that the cascade pattern is the superposition of the ring patterns for different paths through the crystal. It follows that for a cascade of N crystals there will be 2^{N-1} rings. For the ring plane region where $|\rho_{tot}(\varepsilon)| >> 1$, and ζ is small the Belsky-Khapalyuk equations follow the condition that:

$$B_1(\rho,\zeta;|\rho_0|) \approx B_0(\rho,\zeta;|\rho_0|) \quad \text{(A2.15)}$$

In this situation the electric field for each ring is given by:

$$\mathrm{E}(\varepsilon) = 2\begin{pmatrix}\cos(\frac{1}{2}(\theta-\gamma_n))\\ \sin(\frac{1}{2}(\theta-\gamma_n))\end{pmatrix}\mathrm{B}_0\big(\rho,\zeta;\rho_{tot}(\varepsilon)\big)$$
$$\times\Big[\mathrm{F}_{++}(\varepsilon)\{\cos(\frac{1}{2}(\theta-\gamma_1)\}\mathrm{e}_{01}+\sin(\frac{1}{2}(\theta-\gamma_1)\}\mathrm{e}_{02}$$
$$+\,\mathrm{F}_{+-}(\varepsilon)\{\sin(\frac{1}{2}(\theta-\gamma_1)\}\mathrm{e}_{01}-\cos(\frac{1}{2}(\theta-\gamma_1)\}\mathrm{e}_{02}\Big] \qquad \text{(A2.16)}$$

From this the intensity of the ring pattern produced beyond the ring plane is given, in general, by:

$$\mathrm{I}_N(\rho,\zeta)=\mathrm{E}_N^*(\rho,\zeta)\cdot\mathrm{E}_n(\rho,\zeta)=\mathrm{e}_0^*\mathrm{M}_N^\dagger(\rho,\zeta)\mathrm{M}_N(\rho,\zeta)\mathrm{e}_0 \qquad \text{(A2.17)}$$

For circular incident polarisation the intensity can be written as :

$$\mathrm{I}_N(\rho,\zeta)=\Big|\sum_\varepsilon \mathrm{B}_0\big(\rho,\zeta;\rho_{tot}(\varepsilon)\big)\mathrm{F}_{++}(\varepsilon)$$
$$\mp\,\mathrm{i}\sum_\varepsilon \mathrm{B}_0\big(\rho,\zeta;\rho_{tot}(\varepsilon)\big)\mathrm{F}_{+-}(\varepsilon)\Big|^2$$
$$+\Big|\sum_\varepsilon \mathrm{B}_1\big(\rho,\zeta;\rho_{tot}(\varepsilon)\big)\mathrm{F}_{++}(\varepsilon)$$
$$\mp\,\mathrm{i}\sum_\varepsilon \mathrm{B}_1\big(\rho,\zeta;\rho_{tot}(\varepsilon)\big)\mathrm{F}_{+-}(\varepsilon)\Big|^2 \qquad \text{(A2.18)}$$

For two crystals in cascade equation (A2.9) becomes:

$$\mathrm{F}_{++}(++) = \cos\frac{1}{2}\gamma_2, \quad \mathrm{F}_{+-}(+-) = \sin\frac{1}{2}\gamma_2 \tag{A2.19}$$

And the intensity equation can be explicitly written as:

$$\begin{aligned}\mathrm{I}_2(\rho,\zeta) = {} & (|\mathrm{B}_0(\rho,\zeta;\rho_{01}+\rho_{02})|^2 + |\mathrm{B}_1(\rho,\zeta;\rho_{01}+\rho_{02})|^2)\cos^2\frac{1}{2}\gamma_2 \\ & + (|\mathrm{B}_0(\rho,\zeta;\rho_{01}-\rho_{02})|^2 \\ & - |\mathrm{B}_1(\rho,\zeta;\rho_{01}-\rho_{02})|^2)\sin\frac{1}{2}\gamma_2 \\ & \pm 2\mathrm{Im}[\mathrm{B}_0(\rho,\zeta;\rho_{01}+\rho_{02}) * \mathrm{B}_0(\rho,\zeta;\rho_{01}-\rho_{02}) \\ & + \mathrm{B}_1(\rho,\zeta;\rho_{01}+\rho_{02}) * \mathrm{B}_1(\rho,\zeta;\rho_{01}-\rho_{02})] \\ & \times \cos^2\frac{1}{2}\gamma_2\sin^2\frac{1}{2}\gamma_2\end{aligned} \tag{A2.20}$$

A full description of all facets of this theory, including notation and further exapansion beyond what is relevant here, is available in [17].

Analysis based on this theory reproduces a number of previously observed features of the phenomenon, such as the number of observed rings and the degenerate case which reproduces the incident beam first described in initial CD laser papers. Berry's theory also included the prediction relating to differences in patterns between left and right circularly polarised light for a three crystal cascade which is experimentally investigated In chapter 3. However, despite its accuracy and predictions this theory proves unwieldy in a practical

sense and as such, the theoretical work in chapter 3 is based on the single crystal intensity calculations from chapter 2 and the formulation of cascade theory from [48].

Appendix 3 – Second Harmonic Theory

This theoretical treatment is from Schell and Bloembergen's 1978 paper [14]. Firstly, considering an unpolarised incident light beam, the second harmonic beam produced will have polarisation such that it has three wave vectors with three components. The harmonic polarisations are confined to regions of the crystal containing beam intensity such that:

Polarisation	Confining area
$P^{11}(2\omega)$	Ray 1
$P^{22}(2\omega)$	Ray 2
$P^{12}(2\omega)$	Overlap of ray 1 and 2

The direction and magnitude of the second harmonic polarisation in each of the three wave vectors is given by:

$$P_i^{mn}(2\omega) = \chi_{ijk}^{(2)}(-2\omega, \omega, \omega)E_j^m(\omega)E_k^n(\omega) \quad \text{(A3.1)}$$

where m and n both = 1 or 2 and ijk are Cartesian coordinates.

Selecting just one of these polarisations leads to:

$$\vec{P}^{N\,LS}(2\omega) = P_0\hat{p}\exp[i(2\omega/c)n_f(\hat{s}\cdot\vec{r})] \quad \text{(A3.2)}$$

The wave equation of the resulting second harmonic field can be written as:

$$\vec{\nabla}\times\left(\vec{\nabla}\times\vec{E}\right) - \vec{\in}(2\omega)(2\omega/c)^2\vec{E} = 4\pi(2\omega/c)^2\vec{P}^{NLS} \quad \text{(A3.3)}$$

The forced second harmonic wave solution of this inhomogeneous equation is given by:

$$E^{inh} = (A_1\hat{e}_1 + A_2\hat{e}_2 + A_3\hat{e}_3)\exp[i(2\omega/c)n_f(\hat{s}\cdot\vec{r})] \quad (A3.4)$$

where $\hat{e}_1$ and $\hat{e}_2$ are the directions of the electric field related to the unit displacement vector $\hat{d}$. $\hat{d}$ is normal to $\hat{s}$ and both $\hat{e}$ and $\hat{d}$ are described by $\hat{s}$ for the two modes at 2ω. A in equation (A3.4) is given by:

$$A_v = \frac{4\pi P_0 \exp[i(2\omega/c)n_f(\hat{s}\cdot\vec{r})]}{(n_F^2 - n_{v,s}^2)(\hat{d}_v\cdot\hat{e}_v)} \times \left(\hat{d}_v\cdot\hat{p} - \frac{(\hat{d}_v\cdot\vec{\epsilon}\cdot\hat{s})(\hat{p}\cdot\hat{s})}{\bar{\epsilon}}\right) \quad (A3.5)$$

where $n_{v,s}$ (v=1, 2) are the refractive indices at 2ω. The third component, perpendicular to both $\hat{e}_1$ and $\hat{e}_2$ and normal to the boundary is:

$$A_3 = -4\pi P_0(\hat{p}\cdot\hat{e}_3)/\bar{\epsilon} \quad (A3.6)$$

Combining these with (A3.4) gives the complete second harmonic field as:

$$\begin{aligned}\vec{E}(2\omega) = {} & A_1\hat{e}_1\{\exp[i(2\omega/c)n_f(\hat{s}\cdot\vec{r})] - \exp[i(2\omega/c)n_{1\hat{s}}(\hat{s}\cdot\vec{r})]\} \\ & + A_2\hat{e}_2\{\exp[i(2\omega/c)n_f(\hat{s}\cdot\vec{r})] \\ & - \exp[i(2\omega/c)n_{2\hat{s}}(\hat{s}\cdot\vec{r})]\} + A_3\hat{e}_3\exp[i(2\omega/c)n_f(\hat{s}\cdot\vec{r})]\end{aligned} \quad (A3.7)$$

Simplifications due to the polarisation used in the original experiments lead to:

$$\hat{p}\cdot\hat{d}_1 = 1, \qquad \hat{p}\cdot\hat{s} = \hat{p}\cdot\hat{e}_3 = 0, \qquad \hat{p}\cdot\hat{d}_2 = 0 \quad (A3.8)$$

And equation (A3.7) reduces to

$$\vec{E}(2\omega) = \hat{y}\frac{4\pi\omega}{nc\Delta k}P_0\{\exp[i(2\omega/c)n_f(\hat{s}\cdot\vec{r})] - \exp[i(2\omega/c)n_y(2\omega)(\hat{s}\cdot\vec{r})]\} \quad (A3.9)$$

Which describes the complete second harmonic field with the ‘free’ and ‘forced’ rings which overlap.

Appendix 4 – MATLAB Scripts

C1 :- Cross Section

```
% Cross Section Code

% Start Program Timer
tic


% Open the individual files to make the cross section, variable
AllImages contains
% the images.

D = dir('*.png');
for ii = 1:length(D),
    AllImages{ii}=imread(D(ii).name);
end

% Variable Len holds the length of each column vector to be
extracted from
% AllImages. Here it is preallocated for speed purposes

Len= zeros(1,length(D));
for q=1:length(D)
    Len(1,q)=max(size(AllImages{q},2));
end

% Max is the maximum value contained in Len

Max=max(Len);

% This provides a buffer of 10 places to the Max value. By
determining if
% the Max is odd or even. MAXX is the value of Max + buffer.

if rem(Max/2,1)~=0
    MAXX=Max+11;
else
       MAXX=Max+10;
end

% CS is the variable that holds the cross section itself

CS = zeros(MAXX,length(D)); % preallocate for speed

% This deletes cells
for j=1:length(D)
if rem(Len(j)/2,1)~=0
    AllImages{j}(:,Len(j))=[];
end
```

```
48  end
49
50  % Depending on the images being used, either preprepared horizontal
51  slices
52  % or whole images with the central slice extracted slightly
53  different code
54  % is needed.
55  % The images are padded to ensure everything is the same length so
56  it can
57  % be properly aligned to form the cross section.
58
59  % Use for SINGLE COLUMN, HORIZONTAL images
60  for i=1:length(D)
61     CS(:,i)=padarray((AllImages{i})',(round((MAXX-
62  (size(AllImages{1},2)))/2)),'both');
63  end
64
65  % Use for WHOLE IMAGE, HORIZONTAL slice
66  for i=1:length(D)
67     CS(:,i)=padarray((AllImages{i}(round(Len(i)/2),:))',(round((MAXX-
68  (Len(i)))/2)),'both');
69  end
70
71
72  % This section aligns all the column vectors so they line up
73  correctly
74  % Find Maxima and their locations
75  for d=1:length(AllImages)
76  [C(d),I(d)] = eval(['max(CS(:,' int2str(d) '))']);
77  end
78
79  % Find the amount to shift
80  for d=1:length(AllImages)
81  shift(d)=(I(1)-I(d));
82  end
83
84  % Align the arrays
85  for d=1:length(AllImages)
86  pad=eval(['padarray(CS(:,' int2str(d) '),[100 0],0,''both'')']);
87  v=circshift(pad ,shift(d));
88  V(:,d)=v;
89  end
90
91  for i=1:MAXX
92      for j=1:length(D)
93          if CS(i,j)<40
94              CS(i,j)=0;
95          else
96              CS(i,j)=CS(i,j);
97          end
98      end
99  end
100
101 % An averaging filter is applied to CS to smooth the image
102 h=fspecial('average',[3 3]);
103 CSf=imfilter(CS,h);
104 colormap jet
105
106 % Displays the image
```

```
107  imagesc(CSf)
108  set(gca,'position',[0 0 1 1],'units','normalized')
109  axis off
110
111
112  % Stops the program timer
113  toc
```

C2 :- Averaging Program (written by Dr. Guang Tang)

```
%%%% draw rings with averaged data by ImageJ
%%%% draw pixel with fited data
%%%% Required IMAGEJ Plugin available from:
%%%% http://rsb.info.nih.gov/ij/plugins/radial-profile.html

clear all;
Data=[


];   %%%%%Data coped from ImageJ manually. when you change data,
replace the data in [,,]



Radii   = Data(:,1);        %%% the radii of each ring  %%% or
Radii(:)=Data(:,1)
Density = Data(:,2);        %%% the density of each ring
n = length(Radii);          %%% find how many data should be
processed
MaxR = max(Radii);          %%% find the max radii of rings
L=2*MaxR+11;                %%% set buffer size, the buffer should
place the rings
centreX=MaxR+6;  centreY=MaxR+6;  %%% set ring centre in buffer
buffer=zeros(L,L);          %%% set image buffer

RR = 0;                     %%% the distance between each pixel and
centre
for i=1:L
    for j=1:L               %%% for each pixel in buffer, write
        RR=sqrt((i-centreX)^2+(j-centreY)^2);     %%% caculate the
distance from pixel(i,j) to centre
        if RR<=Radii(1)
           buffer(i,j)=Density(1);    %%% when RR< radii of first
ring, write data with data of first ring
        elseif RR>Radii(n)
           %%%  buffer(i,j)=0;        %%% when RR< radii of last
ring, pixel is zero!
        else

            for k=1:n-1
               if (RR>=Radii(k)) && (RR<=Radii(k+1))
                    buffer(i,j)=Density(k)+(Density(k+1)-
Density(k))*(RR-Radii(k))/(Radii(k+1)-Radii(k));
                    break;
               end
            end

        end


    end

end

imshow(buffer,[0,max(Density)]);   %%% display all rings in image
buffer
```

```
57  I= mat2gray(buffer);                %%% convert matrix(double format)
58  to a gray image
59  set(gca,'position',[0 0 1 1],'units','normalized')
60  axis off
61  imwrite(I,'Directory','jpg'); %%%% save the image to specified
62  directory
63  %%%%%%%%%%%%%%%%%%%%%%%%%%%%%%%%
```

C3 :- Single Crystal Conical Diffraction

```
% Berry 2006 paper equation 3.9 for Single Crystal CD
% Start program timer and clear workspace
tic
clc
clear

% Define parameters
lambda=543*10^-9; % Wavelength
A=0.01758;      % Semi Angle of crystal
L1=19.4*10^-3;  % Crystal Length
w=20*10^-6;     %Beam waist radius at the focus
r=1:1:((A*L1)*10^6)+400;    %Variable to define the distance in um
n1=2.01348;     n2=2.04580;     n3=2.08608; % Refractive Indices
k0=n2*(2*pi/lambda);    % Wavenumber
Zeta=0; % Distance from the ring plane
phi=((pi/2));   % Orientation of the crystal G Vector

% Basic Calculations
% p0 is the Ring Radius, p is a running variable of the distance
along the radius from 0 to p0 = 400
p0=(A*L1)/w;
p=(r)/(w*10^6);

% PreAllocation for Speed
Irings=zeros(1,numel(p));
wx=zeros(2881,401); wy=zeros(2881,401);



 % Equation 3.9 'Irings'
% Calculations using Equation 3.9 from Berry 2006 Paper (Equation
1.23 in Chapter 1)
% Irings contains the intensity values at each 1um step along the
length p

for o=1:1:numel(p)
    s(o)=(p(o)-p0)/(sqrt(1+i*Zeta));
    K3=besselj(3/4,(0.25*(s(o))^2));
    K1=besselj(1/4,(0.25*(s(o))^2));
    I3=besselj(3/4,(0.25*(s(o))^2));
    I1=besselj(1/4,(0.25*(s(o))^2));
    fun(o)=(1/(4*sqrt(2*pi)))*(abs(s(o)))^(3/2)*exp(-
0.25*(s(o))^2)*(K3+(sign(s(o))*K1)+(pi*sqrt(2)*heaviside(s(o))*(I3-
I1)));
    Irings(o)=(2/(p0*(1+Zeta^2)^(3/4)))*(abs(fun(o)))^2;
end

% Create a circle onto which the intensity information will be
mapped. The image size, center position and number of points per
degree are defined here
ind=find(Irings>0.00000001);
posit=(A*L1)*10^6;
size=(posit*2)+100;
image=zeros(size+1,size+1);
```

```
centerx=(size/2)+1;
centery=(size/2)+1;
chi=0:(3*pi)/2880:(3*pi);

% Define area into which the intensity information will be fitted, a
large range of 400 data points is used to ensure no information is
lost
for j=1:200
    r=posit-j:1:posit+j;
end

% Calculate the coordinates of every point about the circle with
center as previously defined.
for j=1:401

    wx(:,j)=centerx + r(j)*cos(chi);
    wy(:,j)=centery + r(j)*sin(chi);

end

for j=1:401
for i=1:2881

    ICP(i,j)=Irings(min(ind)+j);

end
end

% Insert the Intensity information into the image
for j=1:201
for i=1:2881

    image(round(wx(i,j)),round(wy(i,j)))=ICP(i,j);

end
end

% Apply some filtering and display parameters
h=fspecial('average',[5 5]);
Imagef=imfilter(image,h);
FigHandle = figure('Position', [100, 100, 100, 100],'OuterPosition',
[100, 100, 500, 500]);
set(gca,'position',[0 0 1 1],'units','normalized')
imagesc(Imagef)
colormap Gray
axis off

% Display the image
figure
plot(Imagef(round((length(Imagef))/2),:))

%Stop the program clock
toc
```

C4 :- Cascade Conical Diffraction 1

```
% 2 Crystal Cascade code based on (46)
tic
clc
clear

% Crystal Lengths
L1=19.4*10^-3;
L2=24.5*10^-3;

% Crystal Orientations
phi1=0;
phi2=(pi/2);
phi21=phi2-phi1;

% Initial Parameters, A is the semi angle of the crystal, r0 defines
the
% center of the each ring pattern. There is no offset between them.
w0 is
% the incident beam waist radius. Power is the power of the laser,
used to
% calculate the incident intensity I0. xgauss and ygauss are
parameters to
% change the output froma  single sharp line to a gaussian shape for
% visibility purposes.

A=0.01758;
r0=[0,0];
w0=60*10^-6;
power=1*10^-3;
I0=power/(pi*w0^2);
xgauss=0:1:10;
ygauss = gaussmf(xgauss,[2 (numel(xgauss)-1)/2]);

% Initial calculations and preliminary things
R1=A*L1;
R2=A*L2;
G1=[(R1*cos(phi1)),(R1*sin(phi1))];
G2=[(R2*cos(phi2)),(R2*sin(phi2))];
r1=r0+G1;
r2=r1+G2;

% Ring Radii and ring intensities defines as per (46)
CR21=abs(abs(G2(2))-abs(G1(1)));
CR22=abs(abs(G1(1))+abs(G2(2)));
I21=(I0/(4*pi*w0*CR21))*(cos((phi21)/2))^2;
I22=(I0/(4*pi*w0*CR22))*(sin((phi21)/2))^2;
I21gauss=ygauss.*I21;
I22gauss=ygauss.*I22;

% Parameters and set up for Image
posit1=round(CR21*10^6);
posit2=round(CR22*10^6);
radius=0:1:posit2+100;
Intensity=zeros(1,posit2+101);
Intensity(1,posit1-((numel(xgauss)-1)/2):posit1+((numel(xgauss)-
1)/2))=I21gauss*10^-11;
```

```
Intensity(1,posit2-((numel(xgauss)-1)/2):posit2+((numel(xgauss)-
1)/2))=I22gauss*10^-11;
Image=horzcat(radius',Intensity');

Data=[Image];               % Data now contains both position and
intensity data as a two column vector
Radii    = Data(:,1);
Intensity = Data(:,2);
n = length(Radii);
MaxR = max(Radii);
L=2*MaxR+11;                          % Setting the buffer size
centreX=MaxR+6;  centreY=MaxR+6;      % define the center of the
matrix in the buffer
buffer=zeros(L,L);                    % pre-allocate the image buffer


% Traces a circle using the two column radius and intensity values
% contained in Data
RR = 0;                               % RR is the position that the
pixel value will be written too
for i=1:L
    for j=1:L
        RR=sqrt((i-centreX)^2+(j-centreY)^2);
        if RR<=Radii(1)
           buffer(i,j)=Intensity(1);
        elseif RR>Radii(n)
            buffer(i,j)=0;
        else
           for k=1:n-1
               if (RR>=Radii(k)) && (RR<=Radii(k+1))
                    buffer(i,j)=Intensity(k)+(Intensity(k+1)-
Intensity(k))*(RR-Radii(k))/(Radii(k+1)-Radii(k));
                    break;
               end
            end

        end


    end

end

% Displaying the image
figure;
imshow(buffer,[0,max(Intensity)]);
I= mat2gray(buffer);
colormap jet


toc
```

C5 :- Cascade Conical Diffraction 2

```
% Berry 2006 paper equation 3.9 (1.23 in this work) for Single
Crystal CD, combined with cascade program C3 based on (46)

% Start program timer and clear workspace
tic
clc
clear

% Define parameters
lambda=543*10^-9; % Wavelength
A=0.01758;      % Semi Angle of crystal
L1=7.94*10^-3;  % Crystal Length
L2=19.4*10^-3;
w=20*10^-6;     %Beam waist radius at the focus
r1=1:1:((A*L2)*10^6)+400;   %Variable to define the distance in um
n1=2.01348;     n2=2.04580;     n3=2.08608; % Refractive Indices
k0=n2*(2*pi/lambda);    % Wavenumber
Zeta=0; % Distance from the ring plane
phi=((pi/2));   % Orientation of the crystal G Vector
phi2=((pi/2));

% Basic Calculations
% p0 is the Ring Radius, p is a running variable of the distance
along the radius from 0 to p0 = 400
p0=(A*L2)/w;
p=(r1)/(w*10^6);

% PreAllocation for Speed
Irings=zeros(1,numel(p));
wx=zeros(2881,401); wy=zeros(2881,401);
wx1=zeros(2881,401); wy1=zeros(2881,401);
wx2=zeros(2881,401); wy2=zeros(2881,401);
ICP=zeros(2881,401); ICP2=zeros(2881,401);

 % Equation 3.9 'Irings'
% Calculations using Equation 3.9 from Berry 2006 Paper (Equation
1.23 in Chapter 1)
% Irings contains the intensity values at each 1um step along the
length p

for o=1:1:numel(p)
    s(o)=(p(o)-p0)/(sqrt(1+i*Zeta));
    K3=besselj(3/4,(0.25*(s(o))^2));
    K1=besselj(1/4,(0.25*(s(o))^2));
    I3=besselj(3/4,(0.25*(s(o))^2));
    I1=besselj(1/4,(0.25*(s(o))^2));
    fun(o)=(1/(4*sqrt(2*pi)))*(abs(s(o)))^(3/2)*exp(-
0.25*(s(o))^2)*(K3+(sign(s(o))*K1)+(pi*sqrt(2)*heaviside(s(o))*(I3-
I1)));
    Irings(o)=(2/(p0*(1+Zeta^2)^(3/4)))*(abs(fun(o)))^2;
end

```

```
% Create a circle onto which the intensity information will be
mapped. The image size, center position and number of points per
degree are defined here
ind=find(Irings>0.00000001);
posit=(A*L1)*10^6;
posit2=posit+(((A*L2)-(A*L1))*10^6);
size=(posit2*2)+100;
image=zeros(size+1,size+1);
centerx=(size/2)+1;
centery=(size/2)+1;
chi=0:(3*pi)/2880:(3*pi);

% Define area into which the intensity information will be fitted, a
large range of 400 data points is used to ensure no information is
lost
for j=1:200
    r=posit-j:1:posit+j;
    r2=posit2-j:1:posit2+j;
end

% Calculate the coordinates of every point about the circle with
center as previously defined.
for j=1:401

    wx1(:,j)=centerx + r1(j)*cos(chi);
    wy1(:,j)=centery + r1(j)*sin(chi);
    wx2(:,j)=centerx + r2(j)*cos(chi);
    wy2(:,j)=centery + r2(j)*sin(chi);
end

for j=1:401
for i=1:2881

    ICP(i,j)=Irings(min(ind)+j);
    ICP2(i,j)=Irings(min(ind)+j);

end
end

% Insert the Intensity information into the image
for j=1:201
for i=1:2881

    image(round(wx1(i,j)),round(wy1(i,j)))=ICP(i,j);
    image(round(wx2(i,j)),round(wy2(i,j)))=ICP2(i,j);

end
end

% Apply some filtering and display parameters
h=fspecial('average',[5 5]);
Imagef=imfilter(image,h);
FigHandle = figure('Position', [100, 100, 100, 100],'OuterPosition',
[100, 100, 500, 500]);
set(gca,'position',[0 0 1 1],'units','normalized')
imagesc(Imagef)
colormap Gray
axis off

```

```
% Display the image
figure
plot(Imagef)

%Stop the program clock
toc
```

C6 :- Linearly Polarised Single Crystal Conical Diffraction

```
% Berry 2006 paper equation 3.9 for Single Crystal CD w/ Linearly
polarised incident beam. Line 76 adapted from C3
% Start program timer and clear workspace
tic
clc
clear

% Define parameters
lambda=543*10^-9; % Wavelength
A=0.01758;      % Semi Angle of crystal
L1=19.4*10^-3;  % Crystal Length
w=20*10^-6;     %Beam waist radius at the focus
r=1:1:((A*L1)*10^6)+400;    %Variable to define the distance in um
n1=2.01348;     n2=2.04580;     n3=2.08608; % Refractive Indices
k0=n2*(2*pi/lambda);    % Wavenumber
Zeta=0; % Distance from the ring plane
phi=((pi/2));   % Orientation of the crystal G Vector

% Basic Calculations
% p0 is the Ring Radius, p is a running variable of the distance
along the radius from 0 to p0 = 400
p0=(A*L1)/w;
p=(r)/(w*10^6);

% PreAllocation for Speed
Irings=zeros(1,numel(p));
wx=zeros(2881,401); wy=zeros(2881,401);




 % Equation 3.9 'Irings'
% Calculations using Equation 3.9 from Berry 2006 Paper (Equation
1.23 in Chapter 1)
% Irings contains the intensity values at each 1um step along the
length p

for o=1:1:numel(p)
    s(o)=(p(o)-p0)/(sqrt(1+i*Zeta));
    K3=besselj(3/4,(0.25*(s(o))^2));
    K1=besselj(1/4,(0.25*(s(o))^2));
    I3=besselj(3/4,(0.25*(s(o))^2));
    I1=besselj(1/4,(0.25*(s(o))^2));
    fun(o)=(1/(4*sqrt(2*pi)))*(abs(s(o)))^(3/2)*exp(-
0.25*(s(o))^2)*(K3+(sign(s(o))*K1)+(pi*sqrt(2)*heaviside(s(o))*(I3-
I1)));
    Irings(o)=(2/(p0*(1+Zeta^2)^(3/4)))*(abs(fun(o)))^2;
end

% Create a circle onto which the intensity information will be
mapped. The image size, center position and number of points per
degree are defined here
ind=find(Irings>0.00000001);
posit=(A*L1)*10^6;
```

```
size=(posit*2)+100;
image=zeros(size+1,size+1);
centerx=(size/2)+1;
centery=(size/2)+1;
chi=0:(3*pi)/2880:(3*pi);

% Define area into which the intensity information will be fitted, a
large range of 400 data points is used to ensure no information is
lost
for j=1:200
    r=posit-j:1:posit+j;
end

% Calculate the coordinates of every point about the circle with
center as previously defined.
for j=1:401

    wx(:,j)=centerx + r(j)*cos(chi);
    wy(:,j)=centery + r(j)*sin(chi);

end

for j=1:401
for i=1:2881

    ILP(i,j)=Irings(min(ind)+j)*(2/pi)*(cos((chi(i)+phi)-
(((chi(i)+phi)/2))))^2;

end
end

% Insert the Intensity information into the image
for j=1:201
for i=1:2881

    image(round(wx(i,j)),round(wy(i,j)))=ILP(i,j);

end
end

% Apply some filtering and display parameters
h=fspecial('average',[5 5]);
Imagef=imfilter(image,h);
FigHandle = figure('Position', [100, 100, 100, 100],'OuterPosition',
[100, 100, 500, 500]);
set(gca,'position',[0 0 1 1],'units','normalized')
imagesc(Imagef)
colormap Gray
axis off

% Display the image
figure
plot(Imagef(round((length(Imagef))/2),:))

%Stop the program clock
toc
```

C7 :- Azimuthally and Radially Polarised Conical Diffraction

```
%%Radial & Azimuthal Theory
%Start Program Timer and clear workspace
tic
clear
clc

%Parameters
r0=25;                  %Annular Beam radius
L=24.5*10^-3;           %Crystal Length
A=0.01758;              %SemiAngle of Cone of Conical Diffraction
R0=(A*L)*10^6;          %Conical Diffraction ring radius

%Two ring splitting
Rplus=((r0/2)+R0);                  %Outer Ring
Rminus=(abs((r0/2)-R0));            %Inner Ring
phi=0:(2*pi)/2880:(2*pi);           %Angles about circle
phig=input('Enter crystal orientation in degrees: ');   %See Prompt
phig=phig*(pi/180);                                     %Convert to
Radians

%Circles
% This section produces the final image and is NOT theoretical, just
MATLAB housekeeping
posit=Rplus;                        %Position along radius of outer
ring
posit2=Rminus;                      %Position along radius of inner
ring
size=(posit*2)+100;                 %Size of image matrix
centerx=(size/2)+1;                 %X-Center point of circle
centery=(size/2)+1;                 %Y-Center point of circle
imagerad=zeros(size+1,size+1);      %Preallocate matrix for speed
imageaz=zeros(size+1,size+1);       %Preallocate matrix for speed

%Add thickness to rings so they are visible
for j=1:10

    r1=posit-j:1:posit+j;
    r2=posit2-j:1:posit2+j;

end

%Circle point coordinates
for j=1:10

    wx1(:,j)=centerx + r1(j)*cos(phi);
    wy1(:,j)=centery + r1(j)*sin(phi);
    wx2(:,j)=centerx + r2(j)*cos(phi);
    wy2(:,j)=centery + r2(j)*sin(phi);

end

```

```
%The business end of things, the vector (i) is the points around the
circle in a single column vector which will be mapped to the
previously defined circle coordinates
for i=1:2881

    Erad(i)=phi(i);                     %Radial Epsilon value from
                                         theory
    EAz(i)=phi(i)-pi;                   %Azimuthal Epsilon value
                                         from theory
    chirad(i)=(2*Erad(i))-phi(i);       %Radial Chi value from
                                         theory
    chiAz(i)=(2*EAz(i))-phi(i);         %Azimuthal Chi value from
                                         theory
    Irad(i)=(cos((phi(i)-phig)/2))^2;   %Radial Intensity
    Iaz(i)=(sin((phi(i)-phig)/2))^2;    %Azimuthal Intensity

    %Same as above but for the Inner Ring
    Erad2(i)=phi(i);
    EAz2(i)=phi(i)-pi;
    chirad2(i)=(2*Erad2(i))-phi(i);
    chiAz2(i)=(2*EAz2(i))-phi(i);
    Irad2(i)=(cos((phi(i)-phig)/2))^2;
    Iaz2(i)=(sin((phi(i)-phig)/2))^2;

end


for j=1:10
for i=1:2881
%Insert Intensity values into image matrix, Radial intensity, outer
ring
    imagerad(round(wx1(i,j)),round(wy1(i,j)))=Irad(i);
%Insert Intensity values into image matrix, Radial intensity, inner
ring
    imagerad(round(wx2(i,j)),round(wy2(i,j)))=Irad2(i);
%Azimuthal intensity, outer ring
    imageaz(round(wx1(i,j)),round(wy1(i,j)))=Iaz(i);
%Azimuthal intensity, inner ring
    imageaz(round(wx2(i,j)),round(wy2(i,j)))=Iaz2(i);

end
end

%Open figures, add smoothing filter, control size, position,
colormap
h=fspecial('average',[7 7]);
Imageradf=imfilter(imagerad,h); Imageazf=imfilter(imageaz,h);
FigHandle = figure('Position', [100, 100, 100, 100],'OuterPosition',
[600, 400, 500, 500],'name','Radial
Polarisation','numbertitle','off');
set(gca,'position',[0 0 1 1],'units','normalized')
imagesc(Imageradf)
colormap gray
FigHandle = figure('Position', [100, 100, 100, 100],'OuterPosition',
[100, 400, 500, 500],'name','Azimuthal
Polarisation','numbertitle','off');
set(gca,'position',[0 0 1 1],'units','normalized')
imagesc(Imageazf)
colormap gray
axis off
```

```
112
113 %Plot radial intensity, horizontally across images
114 figure
115 plot(Imageradf(370,:))
116 figure
117 plot(Imageazf(370,:))
118
119 toc
```

C8 :- Optical Sensor based on Conical Diffraction

```
%Start Program Timer and clear workspace

clc;
clear;
close all
tic

%Read in image from file
vid = videoinput('winvideo');
vidRes = vid.VideoResolution;
nBands = vid.NumberOfBands;
hImage = image(zeros(vidRes(2),vidRes(1),nBands));
preview(vid,hImage);
pause
Image=getsnapshot(vid);

% Threshold the image to binarize it and measure number of areas and
sizes
ImageBinary = Imagegrey > 100;
ImageBinary = imfill(ImageBinary, 'holes');


% Use function imellipse to draw a circle over the largest area of
the beam
figure
imagesc(ImageBinary)
h = imellipse();
pause()

% Make a mask using the selected area
mask = createMask(h);

% Find Boundaries
boundaries = bwboundaries(mask);
thisBoundary = boundaries{1};
x = thisBoundary(:,2);
y = thisBoundary(:,1);

% Measure values along circumference of the drawn circle
for k = 1 : length(x)
    profile(k) = ImageBinary(y(k), x(k));
end

% Plot intensity profile
figure
plot(profile);
title('Profile');
xlabel('Distance');

% Find the broken part of the drawn circle
count=0;
for i = 1:length(profile)
    if profile(i) ~= 1
```

```
53                  count = count + 1;
54          elseif count >= 10
55                  lastIndex = i;
56                  break;
57          else
58                  count = 0;
59          end
60
61          if count == 10
62                 index = i - 9;
63          end
64      end
65
66      %Convert to position of the missing section to angle about circle
67      missingcenter=lastIndex-(lastIndex-index)/2;
68      Start=index*(360/k);
69      End=(lastIndex*(360/k));
70      degree=((missingcenter*(360/k)))
71      incidentbeam=abs(degree/4)
72      toc
73
74      %Display Polarisation angle
75      message = sprintf('The polarisation angle of the incident beam = %f
76      degrees\n', incidentbeam)
77      uiwait(helpdlg(message));
78      close all
79
80
81      toc
```